Shape and Structural Optimization of Flapping Wings

Eric Colby Stewart

Dissertation submitted to the Faculty of the
Virginia Polytechnic Institute and State University
in partial fulfillment of the requirements for the degree of

Doctor of Philosophy
in
Aerospace Engineering

Mayuresh J. Patil, Chair

Robert A. Canfield, Co-Chair

Richard D. Snyder

Rakesh K. Kapania

December 11, 2013
Blacksburg, Virginia

Keywords: Flapping Wing, Micro Air Vehicle (MAV), Multi-objective Optimization, Unsteady Vortex Lattice Method (UVLM), Finite Element Analysis (FEA), Aeroelastic Optimization

Shape and Structural Optimization of Flapping Wings

Eric Colby Stewart

(ABSTRACT)

This dissertation presents shape and structural optimization studies on flapping wings for micro air vehicles. The design space of the optimization includes the wing planform and the structural properties that are relevant to the wing model being analyzed. The planform design is parameterized using a novel technique called modified Zimmerman, which extends the concept of Zimmerman planforms to include four ellipses rather than two. Three wing types are considered: rigid, plate-like deformable, and membrane. The rigid wing requires no structural design variables. The structural design variables for the plate-like wing are the thickness distribution polynomial coefficients. The structural variables for the membrane wing control the in-plane distributed forces which modulate the structural deformation of the wing.

The rigid wing optimization is performed using the modified Zimmerman method to describe the wing. A quasi-steady aerodynamics model is used to calculate the thrust and input power required during the flapping cycle. An assumed inflow model is derived based on lifting-line theory and is used to better approximate the effects of the induced drag on the wing. A multi-objective optimization approach is used since more than one aspect is considered in flapping wing design. The the ϵ-constraint approach is used to calculate the Pareto optimal solutions that maximize the cycle-average thrust while minimizing the peak input power and the wing mass.

An aeroelastic model is derived to calculate the aerodynamic performance and the structural response of the deformable wings. A linearized unsteady vortex lattice method is tightly coupled to a linear finite element model. The model is cost effective and the steady-state solution is solved by inverting a matrix. The aeroelastic model is used to maximize the thrust produced over one flapping cycle while minimizing the input power.

Acknowledgments

Thank you to my Lord and Savior Jesus Christ.

Thank you Melissa, the love of my life, for putting up with me. It is only with your help, support, and encouragement that I actually finished my Ph.D. I am oh-so-glad that I can go through the rest of my life with you. Thanks to my daughter Violet for giving me added motivation to finish quickly.

Thanks to my advisors Dr. Patil and Dr. Canfield for their constant guidance, added knowledge, and encouragement. Many times, I was unfocused, discouraged, and stuck; ya'll helped me focus, get unstuck, and pick my head up. Also, thanks to my other committee members Dr. Kapania and Dr. Snyder for their added wisdom.

Thanks to all of my labmates and peers through grad school: Will Walker, Jeff Ouellette, Ben Leonard, Anthony Ricciardi, Mandar Kulkarni, Chris Emory, Eddie Hale, Karen Scott Walker, Max Richter, and Jonas Radlmayr. You all have been great friends and you taught me much about aerospace engineering. Hopefully you learned at least a small fraction from me compared to what I learned from you.

This material is based on research sponsored by Air Force Research Laboratory under agreement number FA8650-09-2-3938. The U.S. Government is authorized to reproduce and distribute reprints for Governmental purposes notwithstanding any copyright notation thereon. The views and conclusions contained herein are those of the authors and should not be interpreted as necessarily representing the official policies or endorsements, either expressed or implied, of the Air Force Research Laboratory or the U.S. Government.

Dedication

To Melissa. My life is never boring with you.

Contents

List of Figures

List of Tables

Nomenclature

α	instantaneous angle of attack
α_0	angle of attack of the rigid body with respect to the freestream velocity
$\bar{c}$	nondimensional chord
$\bar{s}$	nondimensional span
ΔP	pressure difference on the wing
Δt	time step size
η	nondimensionalized position in the chordwise direction
Γ	circulation on the planform
Γ_b	bound circulation
Γ_w	wake circulation
κ	wing stroke angle
λ_0	assumed inflow for Peters theory
$\mathfrak{x}$, $\mathfrak{y}$	area coordinates of the DKT element
μ	wing deviation angle
ϕ	chordwise Glauert coodinate

ρ	air density
ρ_w	density of the wing material
ρ_w	density of the wing material
σ_1, σ_2	principal stresses
σ_x, σ_y, σ_{xy}	in-plane membrane prestress
τ	wing rotation angle
τ_i	generalized airloads for Peters' aerodynamics
θ	one period of flapping
ξ	nondimensionalized position in the spanwise direction
A	wing area
A^e	area of the e^{th} finite element
A_b	matrix of influence coefficients from the bound vorticity
A_w	matrix of influence coefficients from the wake vorticity
B	DKT strain-displacement relationship matrix
b	semi-chord
B_1, B_2	matricies to shed the wake downstream
C_s	proportional structural damping
$C_{P,peak}$	peak coefficient of power over the flapping cycle
D_0	drag per unit length
D_b	DKT stress-strain relationship matrix

E	modulus of elasticity
F_{aero}	vector of aerodynamic forces acting on the wing
F_e	forces acting on membrane element
$F_{inertia}$	vector of inertial forces acting on the wing
G	$2n$-by-n vector containing the local velocities of the blade elements
h	rigid body motion at the finite element nodes
h	wing thickness
h_{CP}	rigid-body motion at the control points
k	reduced frequency
K_E	kinetic energy
K_s	structural stiffness matrix for the DKT elements
L_0	lift per unit length
M_0	aerodynamic moment per unit length on the wing
M_s	structural mass matrix for the DKT elements
N	finite element shape functions
n	number of blade elements
p	structural membrane mode shapes
p	weighting function used in the weak form of the membrane equation
P_E	potential energy
P_{in}	input power

Q	n-by-n matrix relating the inflow of each blade element to the circulation of all the blade elements
q	finite element nodal degrees of freedom
T	thrust
$T_{\alpha,q}$	matrix that converts nodal deformation to control point rotations
$T_{\Gamma 1}, T_{\Gamma 2}$	matricies that algebraically manipulate the vector of bound vorticity
$T_{a,cp}$	matrix that converts pressure at the control points to nodal forces
T_{avg}	average thrust over one period
$T_{V,q}$	matrix that converts the nodal velocities to velocities at the control points
V_s	velocity of the air acting on the wing due to the rate of the deformation
V_∞	freestream velocity
V_{kin}	velocity of the air acting on the wing due to the prescribed kinematic motion
w_i	Peters' generalized velocities
x	spanwise coordinate of the wing
t	wing thickness

Subscripts

LE	leading edge
TE	trailing edge

Conventions

$\dot{q}$	time derivative of q
T_{AB}	rotate from reference frame A into reference frame B

Superscripts

e	specific finite element
l	left side of the given blade element
r	right side of the given blade element

Chapter 1

Introduction

1.1 Motivation

The concept of flapping-wing flight has existed since the dawn of time. And since then, mankind has attempted to replicate the feat using creations of our own device. Even Wile E. Coyote used a Da Vincian contraption in an attempt to catch the roadrunner via areal assault. But it was not until the late 20th century that engineers successfully built a vehicle that mimics biology and can achieve flight[2, 3].

Since those first man-made ornithopters, the concept of flapping wing vehicles has gained in popularity. In parallel to the ornithopter development, DARPA basically dared the engineering community to shrink the scale of aircraft to a point where the maximum dimension does not exceed six inches[4]. After approximately one decade of using propellers to achieve flight for these Micro Air Vehicles (MAVs), technology had caught up and the development of flapping wing MAVs began in earnest. To create these new MAVs, engineers have relied on biology to guide the design. Since biology evolved this mechanism for flight millennia ago and has continued its use – whether it be birds, bats, insects, or fish (stingrays)– then humans assume that using flapping wings for propulsion must be a suitable choice for flight. By similar logic, MAV engineers assume that the wings that evolution has given the animals must also be Pareto optimal for the particular styles of flight and lifestyle in which the an-

imals participate. Therefore, some of the current flapping wing MAVs have the biomimetic wings of bats[5], birds[6], and insects[7, 8]. However, evolution cares not for aerodynamic performance, but rather focuses on fitness and survival, so these biological designs do not necessarily represent the aerodynamic optimum for MAV missions.

In the last few years, researchers have started to perform optimization studies on flapping wing MAVs to find the best overall design. Since the wings are the only component generating aerodynamic forces, studies have primarily focused on the mechanisms by which thrust and lift are generated and then optimizing the wing shape to take advantage of those mechanisms. Many of the studies treat the wings as rigid and consider aerodynamics only. However, the aeroelastic effects must be considered if the wing structure is optimized. But the combination of shape and structural optimization on a flapping wing has rarely been done.

1.2 Objectives

The focus of the current work is to perform shape and structural optimization on a flapping wing for the micro air vehicle application. During the optimization procedure, average aerodynamic force production is maximized for a flapping cycle while both the power requirement and the wing weight are minimized. The optimization is performed with a gradient-based solver and the Pareto surface is calculated using the ϵ-constraint method, which treats two of the objectives as nonlinear constraints. The design space includes the parameters from a novel wing parameterization that extends traditional Zimmerman planforms by connecting four quarter-ellipses with straight lines. The method gives the ability to explore a large swath of the design space of planforms with only a few variables.

For the simplest structural model - a rigid wing assumption - a low-order aerodynamic model is used in an attempt to get the optimal designs with little computational cost. The aerodynamic model is based off of Peters' two-dimensional quasi-steady aerodynamic model[9] and is combined with blade element theory. An assumed inflow model, based on a discretized version of lifting-line theory[10], is added to approximate finite span effects.

The plate-like wing with deformation is modeled with a Discrete Kirchhoff Triangular (DKT) finite element model. This plate model allows for deformation in both the spanwise and chordwise directions with a high order of fidelity. The membrane-like wing is modeled with constant strain triangular elements to model the out-of-plane deformation as well as the in-plane membrane prestress. The structural design variables for a membrane wing are the coefficients that prescribe the non-uniform prestress in the spanwise and chordwise directions.

For each of the wing models that allow for wing deformation, an aeroelastic model is developed which tightly couples the structural model with an unsteady vortex lattice model (UVLM). The UVLM aerodynamic model is simplified so that the aerodynamic and structural models can be combined into a state-space system of equations with constant coefficients.

Previous studies have optimized parts of the flapping wing system for a wide variety of objective functions. The optimization in this study is focused on flapping wings in the forward flight kinematic configuration. As such, the objective function of primary interest is the cycle-averaged thrust while the peak power required to flap is the secondary objective function. Maximization of the thrust is important, since the MAV needs to generate some aerodynamic forces to move, while minimization of the power objective function is also important, since a micro air vehicle is equipped with a finite amount of battery power on board.

Chapter 2

Literature Review

2.1 Flapping Micro Air Vehicles

Recent efforts in the field of micro air vehicle (MAV) study have focused on creating vehicles that mimic biology. This leads to MAVs that fly using flapping wings, which has been theorized to be more energetically efficient than traditional designs that used propellers and fixed wings when at low Reynolds numbers[11]. Flapping wing vehicles are also beneficial because they can be camouflaged as birds or insects during a mission. Several well-known flapping wing MAVs, such as the Harvard Robofly[7, 8], the clap-and-fling ornithopter built at Wright State[12], and the hummingbird MAV built by Aerovironment[13] have all achieved flapping flight. However, these designs do not have the same wing planforms, revealing the possibility that either none are optimal or each are optimal only for its own mission. Shape optimization of MAV wings must be performed in order to find the best configuration.

2.2 Aerodynamics

Many aerodynamic models have been used in previous micro air vehicle studies. These models range from the inexpensive but less accurate quasi-steady analyses to the accurate and computationally expensive computational fluid dynamics (CFD) models. Selecting the

aerodynamic model for design optimization is problematic since it needs to be both high fidelity and low order for design.

Low-order aerodynamic models include quasi-steady aerodynamic models that have been developed and utilized specifically for MAV research[14, 15, 16, 17, 18, 19]. These models often modify the aerodynamic predictions to fit experimental data by fixing the aerodynamic coefficients. For example, Dickinson, et al.[20] effectively curve-fit some experimental data to calculate the coefficients of lift and drag for an insect wing as a function of the angle of attack during the flapping cycle. Sane and Dickinson[17] similarly fit aerodynamic force production curves to data from experiments, but their data included kinematic parameters. Berman and Wang[16] took data for the coefficients of lift and drag for fruit fly wings from previous work to make their aerodynamic model more accurate. Other low-order models used in MAV analysis are developed to analyze wings as a two-dimensional strip[21, 22, 23]. The aerodynamics on the two-dimensional strip is then integrated over the span of the wing to predict the total aerodynamic loads. Studies that take advantage of these low-order theories are often focused on aspects of the micro air vehicle other than the accuracy of the aerodynamic models, whether that be flight dynamics studies [24, 25, 26], or wing optimization studies [27, 28, 29]. Their preferred status in these studies, despite their low-fidelity, is due to their low computational cost. These low-order models, like their quasi-steady aerodynamic cousins, are used as a first guess in micro air vehicle analysis.

The unsteady vortex lattice method (UVLM)[30] is an aerodynamic model with medium fidelity that has been used in many flapping wing analyses[31, 32, 33, 34, 35, 36]. UVLM is more accurate than the aforementioned low-order models because it captures the three-dimensional effects on the wing as well as the wake effects. When used in an aeroelastic system, UVLM is better than many of the low-order models because it calculates the pressure distribution over the entire wing rather than the effective aerodynamic loads as is done in most-blade element models. The UVLM analysis can get expensive when the wake position is updated and then the Biot-Savart law is called upon to update the aerodynamic influence coefficients, at every time step.

One less common, but still relevant aerodynamic model is the unsteady lifting-line model [37, 38, 39, 40]. The unsteady lifting-line theory was developed as a low-order improvement to the aerodynamic forces for an oscillating wing as compared to the models presented by Theodorsen[41] and Garrick[42]. Unsteady lifting-line models consider the three-dimensional effects on the wing and they can allow for some wing deformation. However, lifting-line is limited in that it is best used for high aspect ratio wings and low reduced frequencies.

Several high-fidelity aerodynamic models are worth some discussion since they have been used in MAV research. One relatively uncommon model is the lattice Boltzmann model which was used in one study[43] to calculate the benefits of flapping a deformable wing at a resonant frequency to get aerodynamic improvement. Other flapping wing research has utilized a Navier-Stokes solver[44] direct numerical simulation[45], however, these high-fidelity models are seldom used to do design research due to their very high computational cost. They are more commonly used when investigating the aerodynamic mechanisms that either help or hinder flapping wing flight.

2.3 Structural Modeling

There are several structural models that have been used in the study of flapping wing micro air vehicles. The simplest wing model is to assume that the wing is completely rigid. This assumption is common when the focus of the study is not on the fluid-structure interactions, but rather on a different area of focus such as aerodynamics [46, 47, 48], flight dynamics [26, 24], or planform studies[29, 47]. The rigid wing is a simplified structural model that greatly reduces computational cost within a study because there is no need to have neither aeroelastic nor aeroservoelastic coupling.

The other way of modeling the structure of the wing is to create a system that allows flexibility. This is more computationally intensive than the rigid assumption, but it is more accurate with respect to an actual flapping wing. Three models are prevalent among micro air vehicle research: beam, plate, and membrane. The beam model is used a when the goal

is some form of wing optimization[27, 49] wherein the structural components of the wing are thin rods. The flapping wing can also be represented as a deformable plate in aeroelastic models[35, 50]. The benefit of a plate model over a beam model is the plate model allows for both spanwise and chordwise deformations which are significant in low-aspect ratio wings; the beam model only allows for deformation in the spanwise direction. Lastly, the membrane model has been used extensively in the analysis of flapping wings[51, 52, 28, 25, 36]. The membrane model is commonly used in conjunction with beams, or battens, that run from the leading edge to the trailing edge to stiffen the membrane. The prevalence of the membrane model is due to its similarities with a bat's wing which has a membrane-like skin attached to the stiffening skeleton. It has also been used as a representation of an insect wing that has the internal structural venation pattern[28].

2.4 Wing Planform and Parameterization

Various studies have been carried out to investigate the effect of wing geometry on the aerodynamic characteristics of micro air vehicles. Moschetta and Thipyopas[53] studied the effect of wing planforms on the performance of fixed-wing biplane MAVs in a wind tunnel. They considered twelve specific planforms and experimentally determined the lift and drag characteristics of each wing shape. During parametric studies, they focused on typical biplane configuration variables such as gap, stagger, decalage angle, etc., but only considered specifically chosen wing shapes. Ansari, et al. [47] studied the effect of planform design on aerodynamic performance for wings in hovering motion, but also only investigated specific wing shapes. The authors used a previously-developed aerodynamic code[18, 19] to explore the effects of aspect ratio, wing length, area, wing offset, and pitch-axis location and noted how lift, drag, and torque all change when only one parameter at a time was varied.

Day[6] created a bird-like wing and parameterized the length of the "feathers" on the fixed wing. The author then used a genetic algorithm to optimize for the length of the individual feathers to maximize the ratio of the experimentally determined lift to drag. The

set-up allowed for many variations on the bird wing, but did not effectively capture other biomimetic shapes.

Many methods of parameterized geometry can be found in the literature. Proper shape parameterization is important to ensure acceptable designs. Two common parameterization techniques are often used. The first method is parameterization by controlling boundary nodal coordinates. This method was used by Persson and Willis[44] to define the leading and trailing edges of their wings. Also, Jagdale et al. [54] used this method effectively to optimize the wing camber of a fixed wing MAV. Although this simple method can be very effective, it can become costly when performing optimization, as it can to lead to a large number of design variables[55, 56]. The boundary node coordinate parameterization method is also hard to control and can lead to non-smooth shapes. The second common method to parameterize the geometry uses polynomial functions where the coefficients are the design variables.

Zimmerman planforms have been used in numerous studies for MAVs. Stanford and Ifju[57] optimized the membrane and shell topology of a fixed-wing Zimmerman planform. Torres and Mueller[58] experimentally studied the lift and drag on Zimmerman, inverse Zimmerman, rectangular, and elliptical planforms for varying aspect ratios and for low Reynolds numbers.

2.5 Micro Air Vehicle Optimization

Design optimization has been applied to micro air vehicles in many ways throughout the literature. In designing a MAV, the researcher must first decide on the parameters to be optimized: whether that be kinematics, shape or stiffness. Researchers must also decide on the objective for which to optimize the design.

The kinematic parameters have been treated as the design variables in many studies. Berman and Wang[16] represented an insect wing as a flat rigid plate and used a blade-element aerodynamics model[14] to analyze the forces generated by a flapping wing. The

kinematics were described as three Euler angles and parameterized as periodic functions. Kurdi, et al.[59] similarly treated the kinematics as the design variables, but parameterized the Euler angles as sinusoidal functions. Ghommem, et al.[60] optimized the two-dimensional motion of a slice of a flapping wing using an unsteady vortex lattice model. Taha, et al.[22] derived a novel, two-dimensional, unsteady aerodynamic model and used calculus of variations to optimize the motion of the blade element of a wing. Thompson et al.[61] experimentally determined the optimal flapping kinematics to generate the maximum lift with a hawk moth wing. They described the three Euler angles as a four-term Fourier series and treated the coefficients as the design variables.

The planform of the flapping wing is seldom considered as a parameter that needs to be optimized. Ansari, et al. developed a aerodynamic model[48] and used the model to analyzed thirteen planforms while varying different components of each design such as area and aspect ratio[47]. Stanford, et al.[27] described the wing planform as a set of blade elements and used the chords of each element as the variables. This parameterization technique was limited and only allowed designs that were symmetric about the mid-chord.

The third aspect of MAV wing design that is often parameterized is the structural stiffness or topology of the structure. The topology of stiff battens within a membrane wing has been studied for both fixed wings[57] as well as flapping wings[28, 62]. The stiffness of a membrane wing can also be varied by changing the applied prestress. For a plate-like wing, the structural stiffness distribution can be controlled through the thickness of the wing.

Just as the design optimization studies focus on different variables, so to do those studies focus on a variety of objective functions. Some studies focus on the need to prolong MAV battery life and thus choose to minimize required power[33, 59, 16, 63]. Other studies treat aerodynamic force production as the objective[50] since micro air vehicles can not fly with out generating a certain amount of lift and thrust. Other studies combine power and thrust requirements into aerodynamic efficiency and use that as the objective[49, 60, 33, 44]. Another idea is to treat aerodynamic force production, power requirements, and overall weight as equally important objectives and then perform multiobjective optimization[29, 54].

2.6 Membrane Wings

Very little work has been done to show the effects that membrane prestress can have on an aeroelastic system. Stearman[64] experimentally showed that an increase in membrane prestress can delay the onset of flutter for a low-aspect-ratio membrane wing which is clamped at the leading and trailing edges and free on the sides. Similar membrane stability analyses have been done using linear[65, 66] and non-linear analyses[67, 68].

Richter and Patil[69] showed that different magnitudes of uniform prestress in a membrane wing change both the aerodynamic force generation as well as the stability of a hovering configuration. Walker et al.[52] coupled a novel two-dimensional aerodynamic model[21] with a two-dimensional Galerkin approximation to the membrane equation. They parameterized the chordwise stiffness in the membrane and calculated the Pareto-optimal set of stress distributions for thrust and thrust efficiency. However, their analysis did not account for spanwise variation in the prestress for two reasons: the blade element approximation to the aerodynamics and the membrane structure was modeled as a two dimensional string.

Chapter 3

Modeling Tools

To perform shape and structural optimization on a wing, the tools to describe and analyze a particular design are required. This chapter describes how the design space is described and then describes each of the analysis tools that are used to optimize the flapping wing planform.

3.1 Shape Parametric Representation

When designing micro air vehicle wings, the method of parameterization of the system must be carefully selected. If a parameterization method is inadequate, then the design space will not be fully explored. The parametric definition must be such that it captures many shapes ranging from the simple circle or triangle to more complex shapes that mimic biology.

It was desired to have a planform parameterization that would allow for effective design space exploration as opposed to the method of performing analysis on only a few select shapes, as has been done in previous studies[47, 53]. To explore the design space, a modified Zimmerman parameterization method was developed. Traditional Zimmerman planforms are created by joining two ellipses at the quarter-chord, while inverse Zimmerman planforms are created by joining the two ellipses at the three-quarter chord[70, 71, 72] as seen in Figure 3.1.

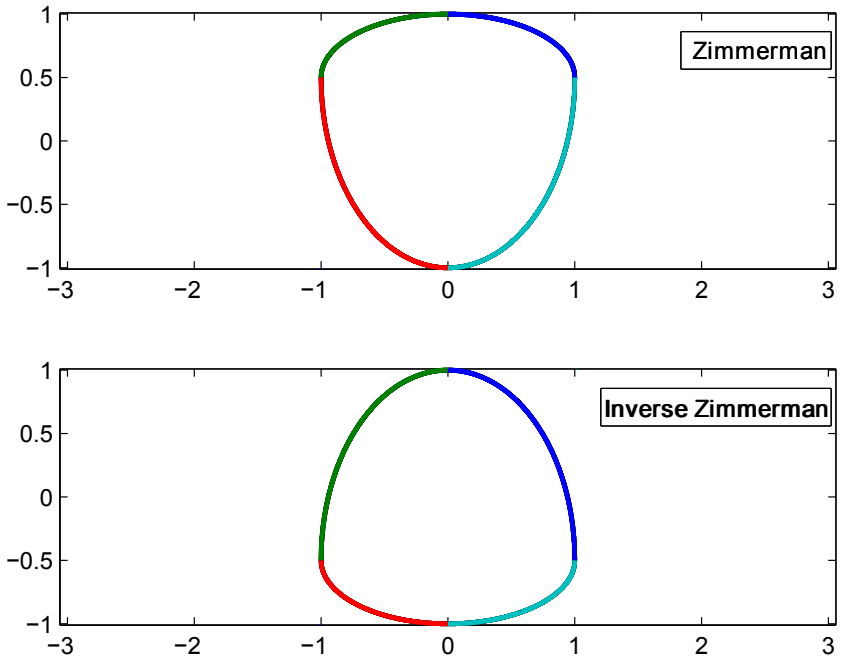

Figure 3.1: Examples of Zimmerman and Inverse Zimmerman planforms

The proposed method extends the Zimmerman planform by using four quarter ellipses and joining them together with straight lines. The quarter ellipse size and location are controlled by the position of its endpoints. There are four quarter ellipses with two endpoints apiece giving only 16 design variables. Each quarter ellipse is controlled independently of the others, but it must maintain the same relative position to the others. Adjacent quarter ellipses are then connected by straight lines to complete the planform. Figure 3.2 gives an example of a general shape that can be generated with the modified Zimmerman method with the endpoints labeled.

The shape generated by the modified Zimmerman method is constrained in size by the nondimensionalized span and chord. The nondimensionalized span goes from $-\bar{s}$ to $\bar{s}$ in the horizontal axis whereas the nondimensionalized chord goes from $-\bar{c}$ to $\bar{c}$ in the vertical axis. A scaling factor is used to re-dimension the design. The coordinates of the endpoints, represented by ξ in the spanwise direction and η in the chordwise direction, as shown in

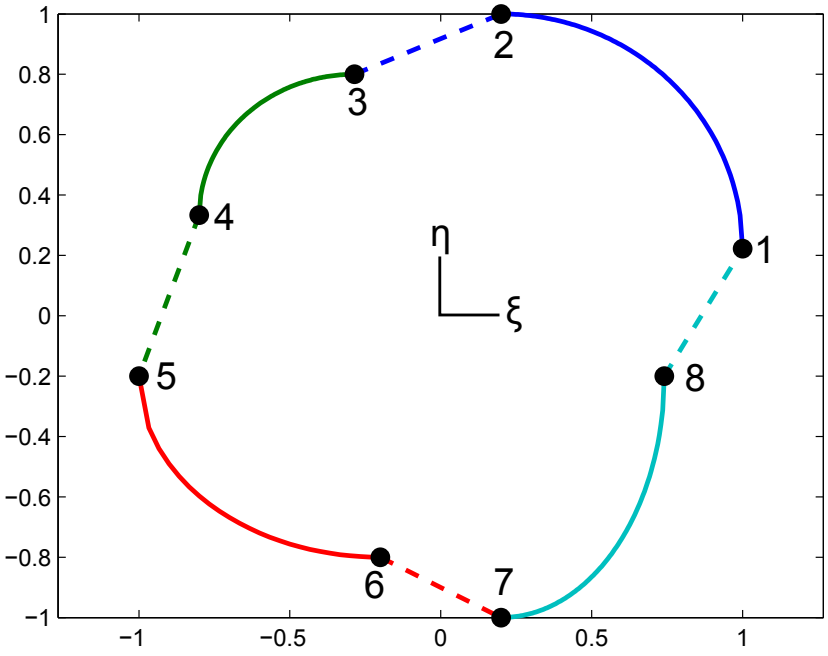

Figure 3.2: General shape generated with modified Zimmerman parameterization. Solid lines represent the quarter ellipses, dashed lines are the straight lines.

Figure 3.2, are constrained as

$$-\bar{s} \leq \xi_4 \leq \xi_3 \leq \xi_2 \leq \xi_1 \leq \bar{s} \tag{3.1}$$

$$-\bar{s} \leq \xi_5 \leq \xi_6 \leq \xi_7 \leq \xi_8 \leq \bar{s} \tag{3.2}$$

$$-\bar{c} \leq \eta_6 \leq \eta_5 \leq \eta_4 \leq \eta_3 \leq \bar{c} \tag{3.3}$$

$$-\bar{c} \leq \eta_7 \leq \eta_8 \leq \eta_1 \leq \eta_2 \leq \bar{c} \tag{3.4}$$

$$\xi_6 \leq \xi_2 \tag{3.5}$$

$$\xi_3 \leq \xi_7 \tag{3.6}$$

$$\eta_5 \leq \eta_1 \tag{3.7}$$

$$\eta_8 \leq \eta_4 \tag{3.8}$$

Each quarter ellipse and straight line is designated to either be part of the leading edge or trailing edge of the wing shape. For instance, Figure 3.2 shows the leading edge of the wing shape consisting of the line segments 5-4, 4-3, 3-2, and 2-1. The trailing edge of the planform is defined by the segments 5-6, 6-7, 7-8, and 8-1. The leading and trailing edges are piecewise continuous and described by the functions

$$\eta_{LE} = \begin{cases} \left(\frac{\eta_4-\eta_5}{\xi_4-\xi_5}\right)(\xi_{LE}-\xi_4)+\eta_4 & \xi_5 \le \xi_{LE} \le \xi_4 \\ \eta_4 + \sqrt{(\eta_3-\eta_4)^2 - (\eta_3-\eta_4)^2\left(\frac{\xi_{LE}-\xi_3}{\xi_3-\xi_4}\right)^2} & \xi_4 \le \xi_{LE} \le \xi_3 \\ \left(\frac{\eta_2-\eta_3}{\xi_2-\xi_3}\right)(\xi_{LE}-\xi_2)+\eta_2 & \xi_3 \le \xi_{LE} \le \xi_2 \\ \eta_1 + \sqrt{(\eta_2-\eta_1)^2 - (\eta_2-\eta_1)^2\left(\frac{\xi_{LE}-\xi_2}{\xi_1-\xi_2}\right)^2} & \xi_2 \le \xi_{LE} \le \xi_1 \end{cases} \tag{3.9}$$

$$\eta_{TE} = \begin{cases} \eta_5 - \sqrt{(\eta_5-\eta_6)^2 - (\eta_5-\eta_6)^2\left(\frac{\xi_{TE}-\xi_6}{\xi_6-\xi_5}\right)^2} & \xi_5 \le \xi_{LE} \le \xi_6 \\ \left(\frac{\eta_7-\eta_6}{\xi_7-\xi_6}\right)(\xi_{TE}-\xi_6)+\eta_6 & \xi_6 \le \xi_{LE} \le \xi_7 \\ \eta_8 - \sqrt{(\eta_8-\eta_7)^2 - (\eta_8-\eta_7)^2\left(\frac{\xi_{TE}-\xi_7}{\xi_8-\xi_7}\right)^2} & \xi_7 \le \xi_{LE} \le \xi_8 \\ \left(\frac{\eta_1-\eta_8}{\xi_1-\xi_8}\right)(\xi_{TE}-\xi_1)+\eta_1 & \xi_8 \le \xi_{LE} \le \xi_1 \end{cases} \tag{3.10}$$

There are several combinations as to which segments of the wing shape are part of the leading edge and which ones are part of the trailing edge. Line segments 5-4 and 8-1 can be located on either the leading edge, trailing edge, or neither if $\xi_4 = \xi_5$ or $\xi_8 = \xi_1$. The spanwise distribution of the chord can be represented as

$$c(\xi) = \eta_{LE} - \eta_{TE} \tag{3.11}$$

The modified Zimmerman method is versatile. All of the simple shapes used in Ansari, et al.[47] can be reproduced, as well as many biologically-inspired shapes. Figure 3.3 shows simple shapes that can be generated with modified Zimmerman. The square is created by collapsing the endpoints of the quarter ellipses to single points. The triangle is likewise created by collapsing two ellipses into a single vertex. The modified Zimmerman method can

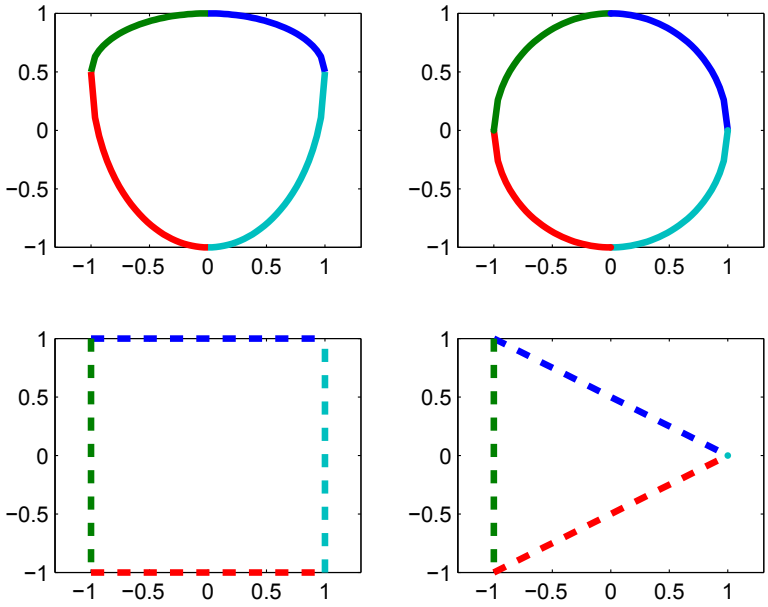

Figure 3.3: Simple shapes drawn with the modified Zimmerman approach

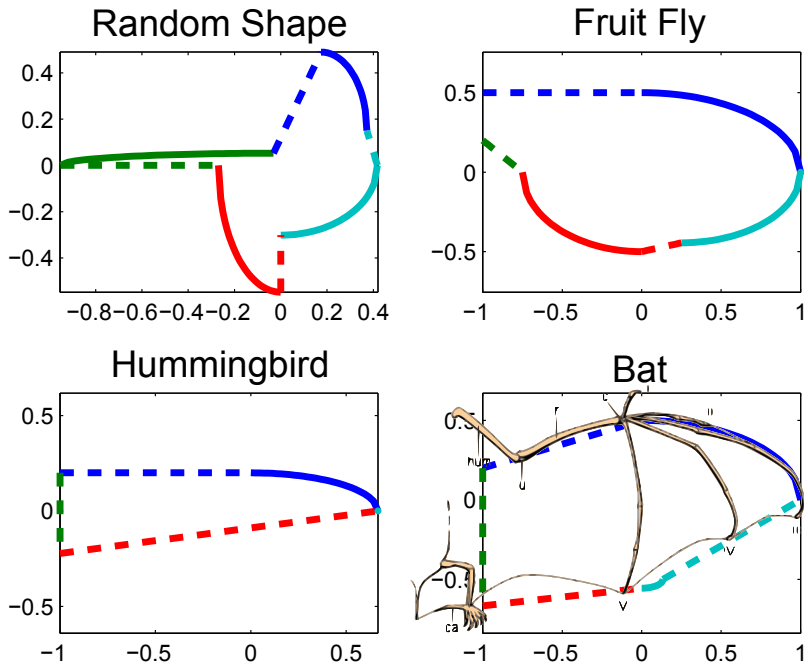

Figure 3.4: One random and three biomimetic plan forms drawn with the modified Zimmerman approach

also create biomimetic planforms as seen in Figure 3.4. The biomimetic planforms do not obviously represent biology until a wing picture is overlaid onto the modified Zimmerman planform, as was done with the bat wing[73]. For all of the planforms, the wing hinge is located on the left side of the figure and the freestream is considered to be moving from top to bottom relative to the wing.

3.2 Structural Parameterization

3.2.1 Thickness of Plate Wing

The structural design for the plate-like wing is controlled by the thickness distribution in the wing. The thickness on the wing is parameterized by describing the thickness distribution as a six-term quadratic polynomial

$$t(\xi,\eta) = t_0 + t_1\xi + t_2\eta + t_3\xi^2 + t_4\eta^2 + t_5\xi\eta \tag{3.12}$$

where $t_0 - t_5$ are the thickness distribution coefficients that become design variables.

3.2.2 Prestress of Membrane Wing

The structural design of a membrane is controlled by the amount of prestress that is applied to the wing. The wing prestress parameterization is difficult to control since the prestress inside the wing must satisfy the equilibrium conditions; also, the wing must be in a state of tensile stress since compression is not appropriately modeled using linear finite elements.

Satisfying the equilibrium equation for all iterations is difficult since the planform changes with each iteration. So the membrane prestress is calculated inside the wing using the following steps:

1. A wing planform is defined using the modified Zimmerman method as in Figure 3.5

2. The forces on the rectangular membrane are applied with the boundary conditions

shown in Figure 3.6. This leads to a prestress distribution within the membrane. An example of the Von Mises stress distribution is shown in Figure 3.7.

3. The current planform is "glued" to the membrane and takes on the stress state within its boundary as in Figure 3.8.

4. Physically, the excess membrane is then cut away from the planform, leaving only the planform and a membrane with a non-uniform prestress state shown in Figure 3.9

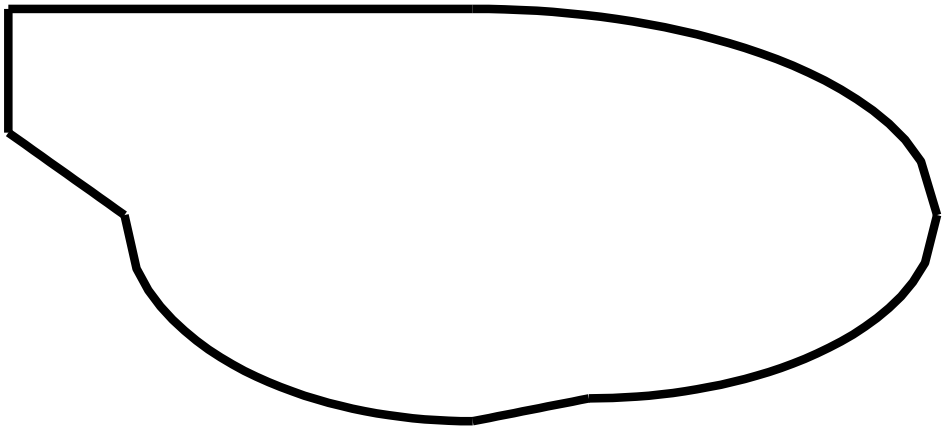

Figure 3.5: First stage in prestress definition

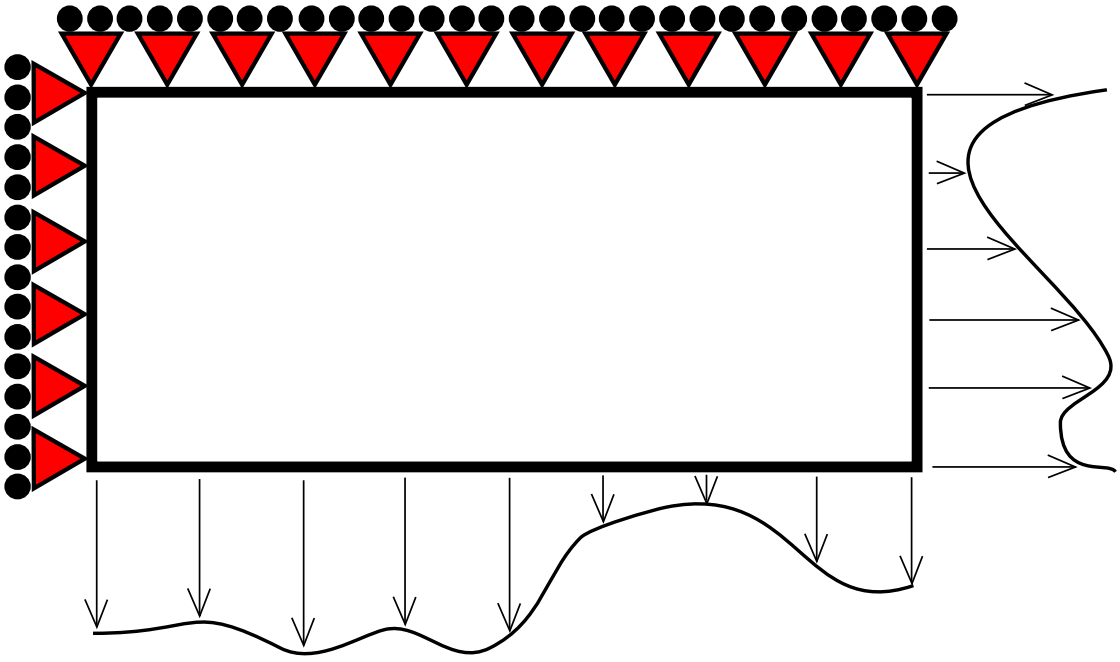

Figure 3.6: Second stage in prestress definition

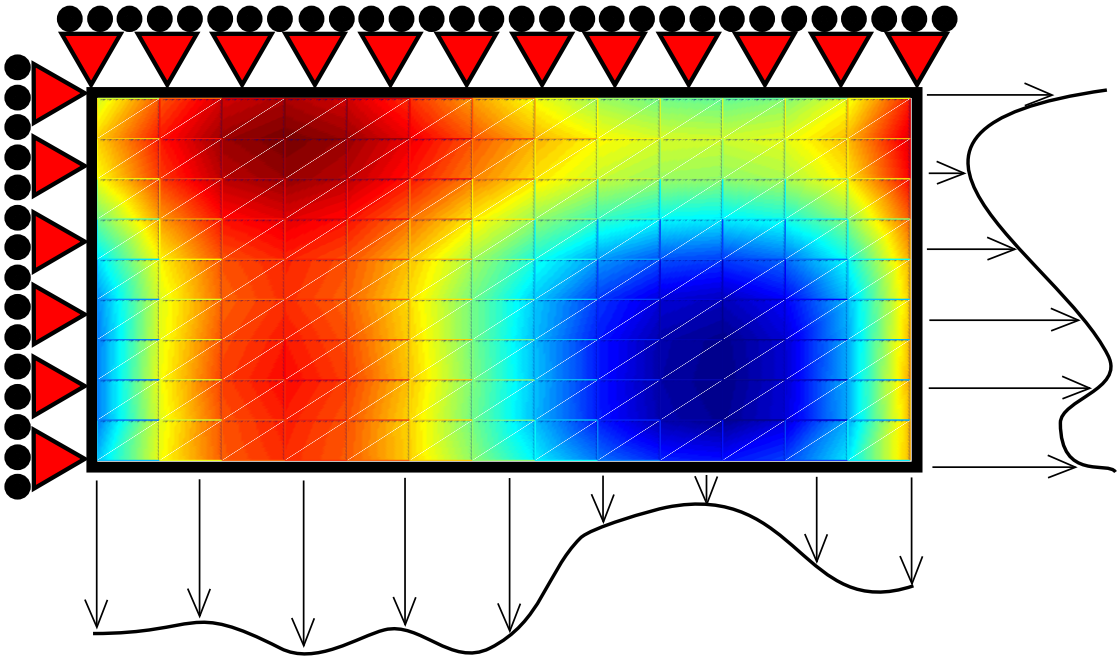

Figure 3.7: Third stage in prestress definition

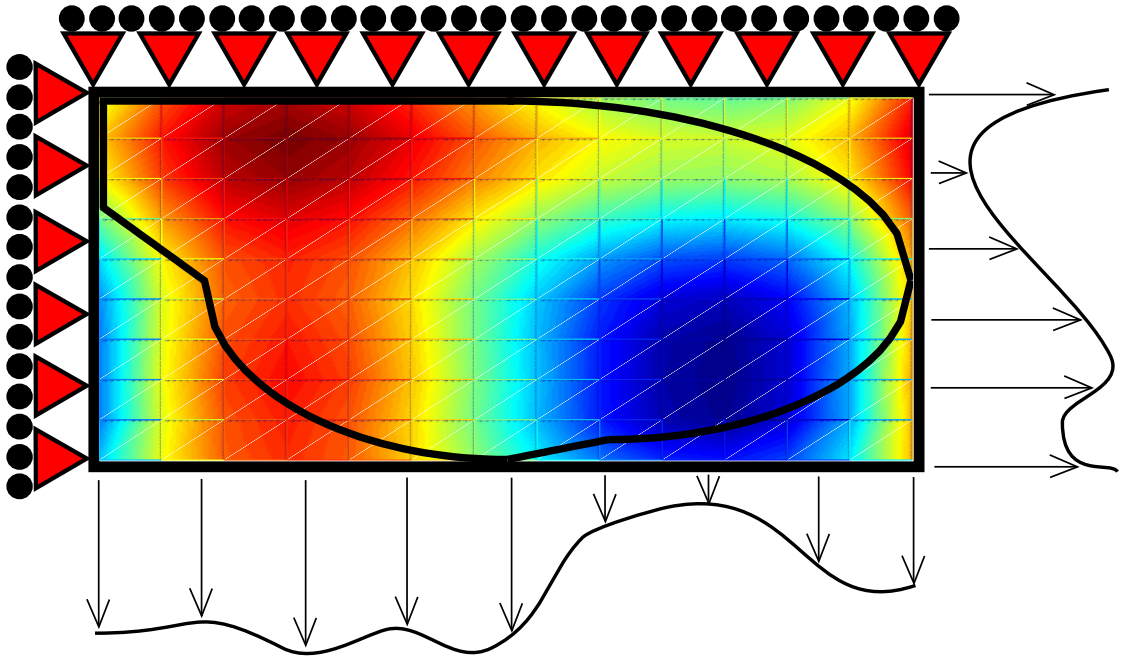

Figure 3.8: Fourth stage in prestress definition

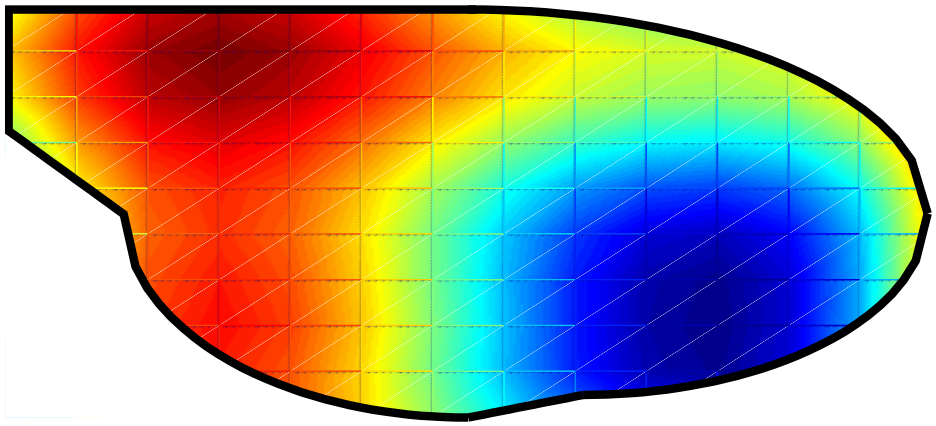

Figure 3.9: Fifth stage in prestress definition

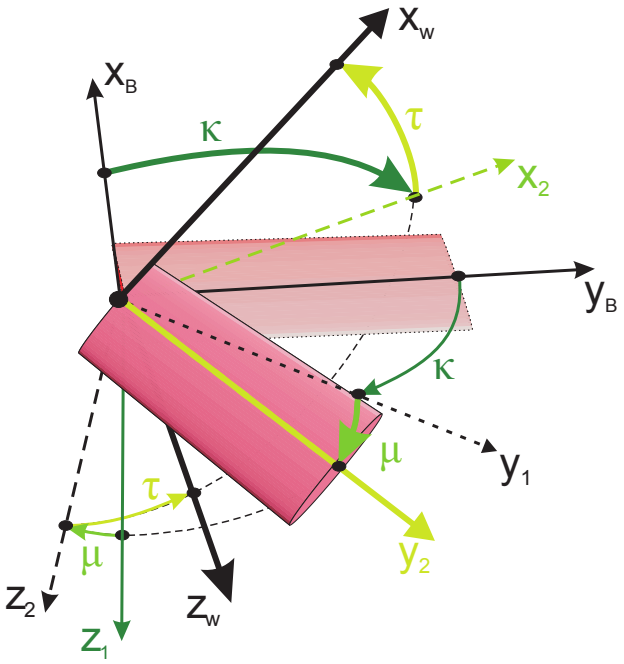

Figure 3.10: Kinematics description

3.3 Kinematics Definition

The kinematics description that was used is shown in Figure 3.10. A set of Euler angles κ, γ, and μ represent the stroke, deviation, and rotation of the wing with respect to the stroke frame[24, 25]. The stroke frame and the body frame are the same since the stroke angle was assumed to be zero. The transformation matrix to get from the body frame to the wing frame is given by the following rotation sequence

1. Rotate the wing through κ about z_B to get (x_1, y_1, z_1)
2. Rotate the wing through γ about x_1 to get (x_2, y_2, z_2)
3. Rotate the wing through μ about y_2 to get (x_w, y_w, z_w)

The transformation matrix is thus defined as $[T_{wb}] = [T_{w2}(\mu)]\,[T_{21}(\gamma)]\,[T_{1b}(\kappa)]$.

Both forward flapping flight (called flapping for the rest of this paper) and hovering configurations were studied to find the best wing planform for each case. In the flapping configuration, only deviation γ was prescribed and a constant velocity parallel to the wing

was assumed. For hovering, the prescribed wing motion was sinusoidal stroke with an out of phase rotation at the end of the stroke and no deviation.

3.4 Low-Order Aerodynamics

3.4.1 Peters' Airloads Model

The aerodynamic forces for a rigid wing are captured using Peters' two-dimensional, inviscid aerodynamic model[9] coupled with an inflow model that captures the induced drag effects. Peters' model is well suited for the application to MAVs because it is written in the wing reference frame and allows for large reference frame motions. The pressure difference ΔP over a 2-D section of the wing planform is written as

$$\Delta P = 2\rho \left[\tau_0 \frac{1 - \cos(\phi)}{\sin(\phi)} + \sum_{i=1}^{\infty} \tau_i \sin(i\phi) \right] \tag{3.13}$$

where ρ is the air density and ϕ is the chordwise coordinate from a Glauert transformation as

$$x = b \cos(\phi) \tag{3.14}$$

with $\phi = 0$ at the trailing edge, $\phi = \pi$ at the leading edge, and b is the semi-chord. The τ_i are the generalized loads and are formulated in terms of the generalized velocities (w_i), which are expansion terms of the total induced flow from the circulation, and the weighted average of the assumed inflow (λ_0) over the 2-D wing section

$$\tau_0 = u_0(v_0 - \lambda_0) \tag{3.15}$$

$$\tau_1 = b\,\dot{v}_0 + u_0 v_1 \tag{3.16}$$

An inflow model was created to account for the induced drag on the planform.

The lift and drag in the wing frame is easily computed from the pressure differential on the airfoil. The lift per unit length L_0, drag per unit length D_0, and moment per unit length

M_0 on a blade element can be found by integrating the pressure over the chord. The drag also includes a leading-edge suction term, which is the only chordwise force in the wing frame when no deformation is present and the spanwise effects are ignored.

$$L_0 = -\int_0^{\pi} b\Delta P \sin(\phi)\, d\phi = -2\pi\rho b \left(f\tau_0 + \frac{1}{2}\tau_1 \right) \tag{3.17}$$

$$D_0 = -2\pi\rho b f \left(v_0 - \lambda_0 \right)^2 \tag{3.18}$$

$$M_0 = -\int_0^{\pi} b\Delta P \cos(\phi) \sin(\phi)\, d\phi = \pi\rho b \left(\tau_0 - \frac{1}{2}\tau_2 \right) \tag{3.19}$$

3.4.2 Blade Element Theory

The forces over the entire wing were calculated by integrating the two-dimensional airloads over the span as per blade element theory[17]. Blade element theory has been used effectively in previous attempts to calculate the forces on an MAV wing[74, 27, 18, 19]. The fruit fly wing shown in Figure 3.11 shows how a wing generated with the modified Zimmerman method can be discretized into n total blade elements.

Once the eight endpoints from modified Zimmerman are positioned using the 16 design variables and straight lines connect the quarter ellipses, the planform is divided into strips to be used in blade element theory. The ξ positions of the center of each of the n blade elements used are found as

$$\xi_c^i = \min(\xi) + \left(i - \frac{1}{2} \right) \frac{\max(\xi) - \min(\xi)}{n}$$

where $\min(\xi)$ is the minimum ξ value of the planform, which is always either ξ_4 or ξ_5, and $\max(\xi)$ is the maximum ξ value, which is always either ξ_1 or ξ_8.

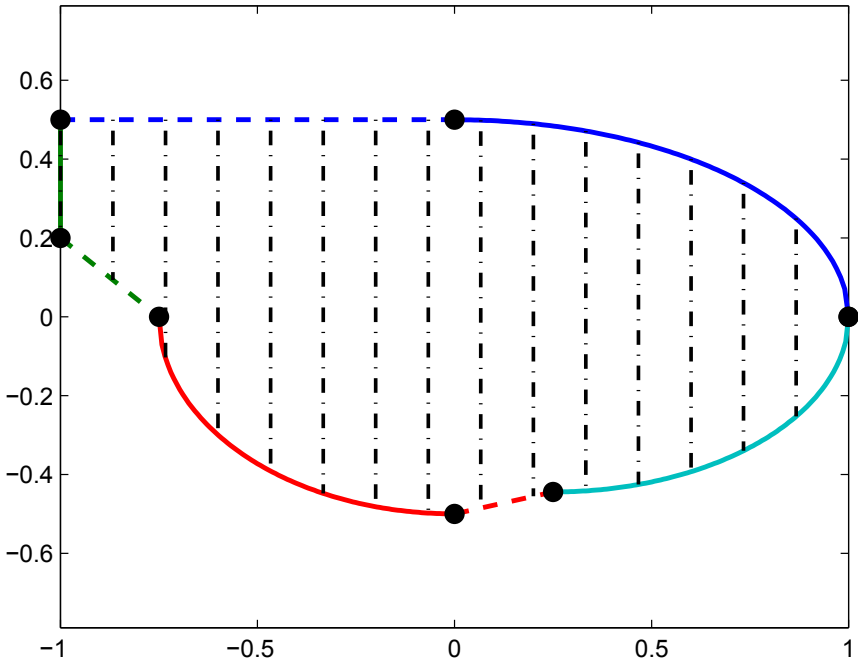

Figure 3.11: Sample shape generated with modified Zimmerman method with blade elements

3.4.3 Assumed Inflow Model

Calculating the weighted average of the inflow from the motion of the wing is done by first relating the bound circulation, Γ and the inflow on a 2D section of the planform as

$$\Gamma = 2\pi b \left[w_0 - \lambda_0 + \frac{1}{2} w_1 \right] \tag{3.20}$$

Using lifting-line theory[10],the total bound circulation on a single blade is related to the induced flow at each point along the lifting line as

$$\lambda_0 (x_0) = \frac{1}{4\pi} \int_0^{\bar{s}} \frac{d\Gamma/dx}{x_0 - x} dx \tag{3.21}$$

where x is the spanwise coordinate and $\bar{s}$ is the semi-span of the wing. The continuous form of lifting line theory can be discretized to be used with the blade elements generated with the modified Zimmerman method. The induced flow on the i^{th} blade element due to the bound

circulation on the j^{th} element is found as

$$\lambda_0^i = \sum_{j=1}^{n} \frac{\Gamma_j}{4\pi \left(x_i - x_j^l\right)} - \frac{\Gamma_j}{4\pi \left(x_i - x_j^r\right)} \tag{3.22}$$

where x_j^l is the position of the left side of the j^{th} blade element and x_j^r is the position of the right side. Equation 3.22 can be put in matrix form as

$$\{\lambda\} = [Q]\{\Gamma\} \tag{3.23}$$

where Q is an n-by-n matrix and $\{\Gamma\}$ is an n-by-1 vector containing the values of circulation on each of the blade elements. The total bound circulation for the i^{th} blade element in Eq. 3.20 can be represented in matrix form as

$$\Gamma_i = \begin{bmatrix} 2\pi b_i & \pi b_i \end{bmatrix} \begin{Bmatrix} v_0 \\ v_1 \end{Bmatrix}_i - 2\pi b_i \lambda_0^i \tag{3.24}$$

The matrix equations for each blade element are combined to give

$$\{\Gamma\} = [A]\{G\} + [P]\{\lambda\} \tag{3.25}$$

where A is an n-by-$2n$ matrix which is multiplied by the $2n$-by-1 vector G containing the velocities of all of the blade elements. P is an n-by-n diagonal matrix which multiplies the $\{\lambda\}$ that is an n-by-1 vector containing the inflows for each of the n blade elements. Combining equation 3.23 and equation 3.25, the bound circulation can be eliminated and the weighted average of the inflow can be calculated directly from the wing motion.

$$\{\lambda\} = [Q]\left[[I] - [P][Q]\right]^{-1}[A]\{G\} \tag{3.26}$$

3.5 Unsteady Vortex Lattice Method

The unsteady vortex lattice method (UVLM) calculates the aerodynamic forces on a wing by discretizing the continuous sheet of vorticity on a wing into a set of ring vortices. The no-penetration boundary condition is imposed at a set of control points. The vorticity along the trailing edge is shed into the wake at each time step. The finite segments of bound vorticity and wake vorticity induce a downwash on the wing according to the Biot-Savart law[30] which is used to calculate the total downwash at each control point from all of the bound ring vortices, Γ_b and wake vortices, Γ_w.

The no-penetration boundary condition is a set of summations of the velocities acting on the control points which is set to zero so that no fluid passes through the wing at the control points. In an aeroelastic system, the no-penetration boundary condition takes the form

$$[A_w]\{\Gamma_w\} + [A_b]\{\Gamma_b\} = \vec{V}_{kin} \cdot \vec{n} + \vec{V}_s \cdot \vec{n} \tag{3.27}$$

where A_w and A_b are the set of influence coefficients from the wake vortices and bound vortices, respectively. The velocity on the wing from the structural deformation V_s and the kinematics V_{kin} are dotted with the normal vector on the control point, which is located at the center of each lattice panel.

Several assumptions about the UVLM system are made in the current analysis. The plate finite element model assumes small out-of-plane deformations, so the effect of flexibility is negligible when calculating the influence matrix for the bound vorticity. Also, the wake is assumed to shed directly behind the wing at each time step and stays in the plane of the wing throughout the analysis. This decreases the complexity of the analysis and makes the wake influence coefficient matrix constant over the duration of the analysis.

The aerodynamic model is validated for various aspect ratio wings at an angle of attack. The flat wing is in a constant freestream and is started instantaneously from rest. The coefficient of lift for the different aspect ratios is shown in Figure 3.12 and the coefficient of drag is shown in Figure 3.13. The current analysis with the flat wake assumption accurately predicts

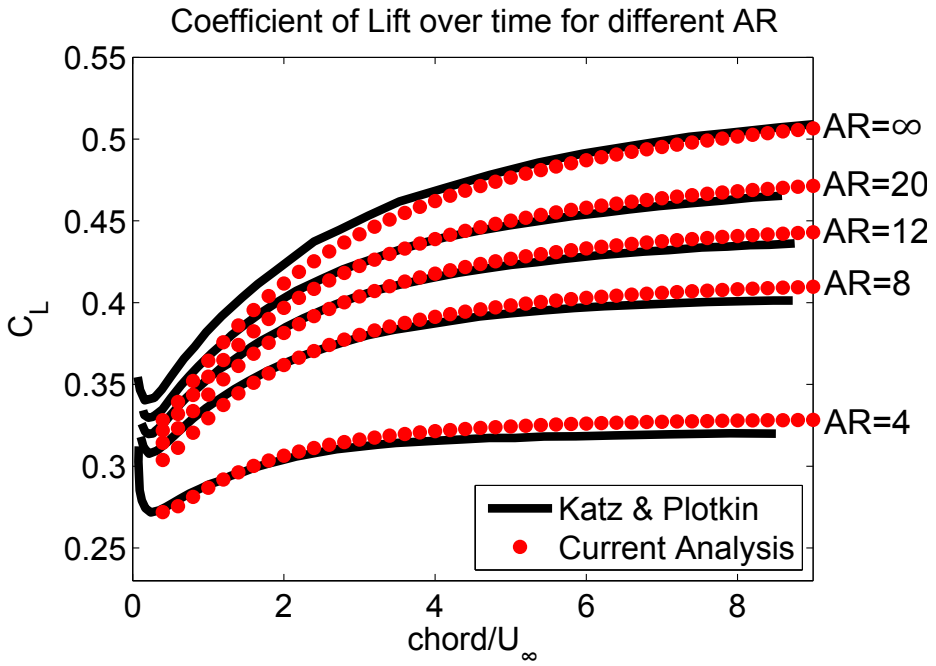

Figure 3.12: Coefficient of lift for wing with impulse start from rest

the transient lift and the drag on the wing in comparison to Katz and Plotkin'sresults[30].

The UVLM model is then compared with data from Heathcote et al.[75] for the case of a rigid wing in plunging motion. The rigid wing is plunged at various reduced frequencies and the cycle-averaged thrust coefficient is given in Figure 3.14 and is also compared with the UVLM model used by Ghommem[34]. The current analysis is a simplified version of the Ghommem model since the wake is assumed to be flat throughout the flapping cycle, yet the two unsteady vortex lattice models agrees well over the range of reduced frequencies. Both UVLM models over-predict the coefficient of thrust because of the viscous effects that are unaccounted for in UVLM.

3.6 Structural Models

In the shape and structural optimization of flapping MAV wings, three wing types were chosen to optimize: rigid, plate-like, and membrane-like. The aerodynamic models described above have the rigid wing assumption built in to them, so a separate structural model is

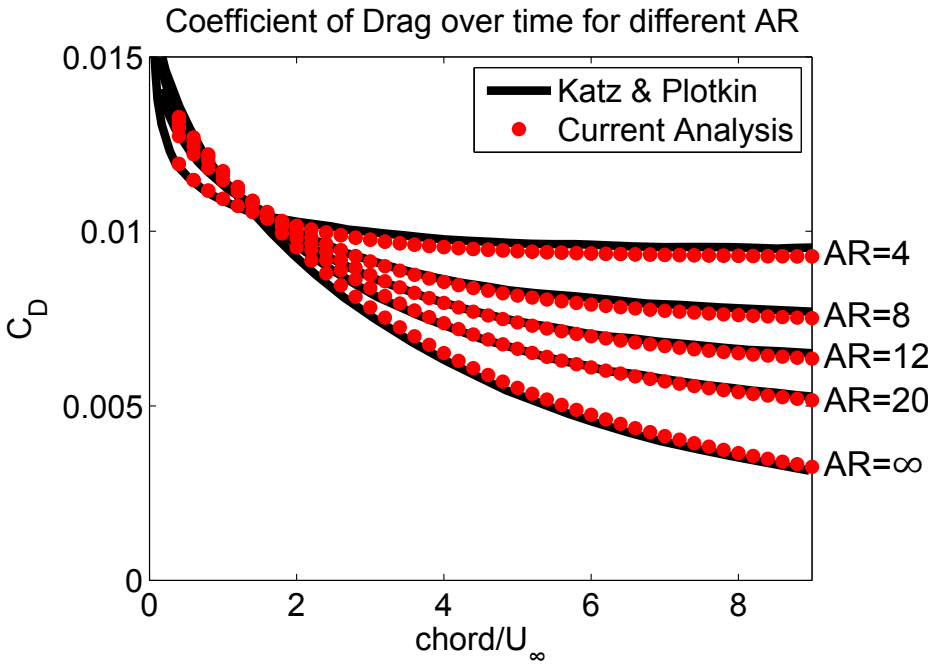

Figure 3.13: Coefficient of drag for wing with impulse start from rest

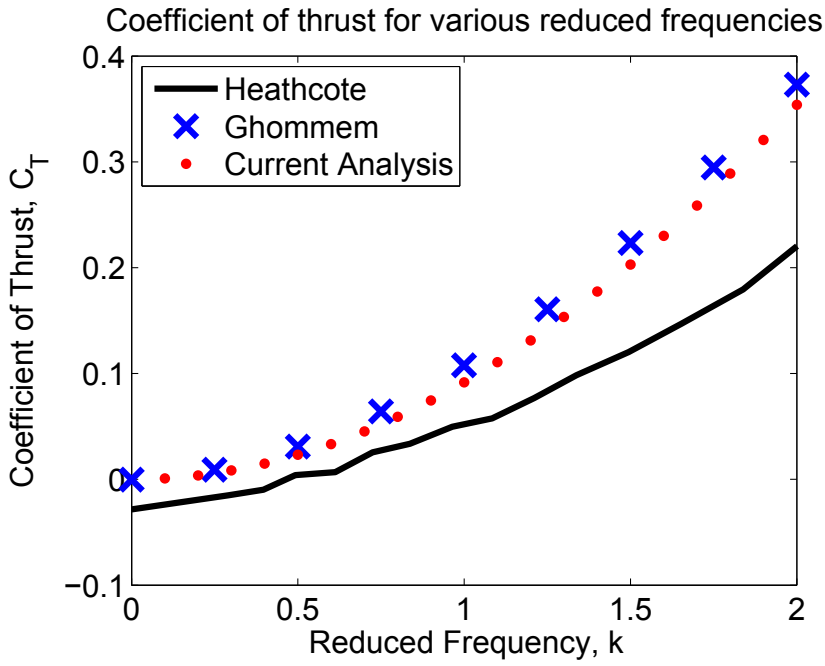

Figure 3.14: Average thrust coefficient for various reduced frequencies

needed. For the plate and membrane wing types, the deformation due to flapping is unique to the wing type and the stiffness distribution of each is controlled by a different set of design parameters.

3.6.1 Plate Model

Plate finite elements (FE) are chosen to to model plate-like deformation in the flapping wings. Finite elements are an efficient way to model the deformation because the structural model can easily be coupled to an aerodynamic model. The wing is modeled as a plate to account for the moments that are carried by the wing during passive deformation. Linear finite element analysis (FEA) is used because non-linear finite elements will have a small effect for small deformations and would be too computationally expensive when performing shape and structural optimization of the flapping wings.

3.6.1.1 Theory

Discrete Kirchhoff Triangular (DKT) elements are chosen as the plate structural model. More information about DKT elements can be found in various sources[76, 77, 78] and a simple, yet full derivation can be found in [79]. However, a short discussion of the DKT element will be carried out here. Discrete Kirchhoff elements start with the thin plate assumptions:

1. The mid-surface of the plate remains unstretched
2. Planes that are straight and normal to the mid-plane remain straight and normal
3. Transverse shear strain is considered negligible

DKT elements have 21 variables with 12 constraints which relate the independent values for displacement and rotation, thus giving a nine degree-of-freedom element. There are three degrees of freedom at each of the three corner nodes - two rotations and transverse displacement. C^1continuity is ensured between the elements by using six nodes on the element, three at the corners and three at the midpoints on the edges. The stiffness, K_s, and mass, M_s, matrices of a DKT element are found as

$$K_s^e = 2A^e \int_0^1 \int_0^{1-\eta} B^T D_b B \, d\mathfrak{x} d\mathfrak{y} \tag{3.28}$$

$$M_s^e = A^e \int_0^1 \int_0^{1-\eta} \rho_w t_h N^T N \, d\mathfrak{x} d\mathfrak{y} \tag{3.29}$$

where A^e is the area of the element e, B is the strain-displacement matrix, D_b is the stress-strain relationship for the bending of the element, ρ_w is the density of the wing material, t is the thickness of the element, N is the vector of DKT shape functions, and $\mathfrak{x}$ and $\mathfrak{y}$ are the area coordinates of the element. The structural stiffness matrix is evaluated exactly using three-point Gauss quadrature while the structural mass matrix is evaluated using seven-point Gauss quadrature. The elements in the mesh are created using a structured grid such that the nodes in the finite element model and the lattice line intersections in the UVLM model are coincident. An example of the structured grid is shown for a fruit fly wing in Figure 3.15. Any node along the wing hinge, located at the left side of the wing, is given clamped boundary conditions to prevent any displacement or rotation. These specific boundary conditions apply to the plate-like deformable wing only.

3.6.1.2 Verification

The plate finite element code is checked against the modes shapes of a simply supported plate. In calculating free vibration of a system using finite elements, the simplest way to find the natural frequencies and mode shapes is to solve the eigenvalue problem as

$$\left[-\omega^2 M_s + K_s\right] \{q\} = 0 \tag{3.30}$$

The vector q is the set of degrees of freedom not constrained by the boundary conditions. To not get the trivial solution $\{q\} = 0$ for the eigenvalue problem, the new problem becomes

$$\det\left[-\omega^2 M_{DKT} + K_{DKT}\right] = 0 \tag{3.31}$$

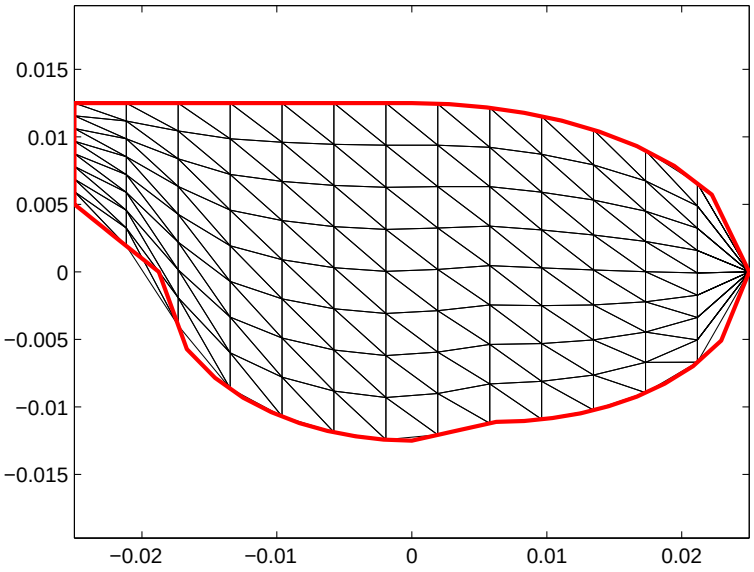

Figure 3.15: Example of a fruit fly wing with structured mesh

Table 3.1: Comparison of natural frequencies for a simply supported plate.

Mode	Analytical	DKT	Percent Difference
ω_{11}	4.935	4.913	0.448
$\omega_{12} = \omega_{21}$	12.337	12.242	0.769
ω_{22}	19.739	19.410	1.667
ω_{31}	24.674	24.429	0.994

Solving this equation gives the natural frequencies ω_i of the system. Substituting the natural frequencies back into the original eigenvalue problem gives the corresponding mode shapes of the system. An analytical solution to this system is known for a simply supported plate[80]. The natural frequencies for the first four modes are found and compared in table 3.1 using the analytical solution and the DKT elements.

The first four mode shapes of the simply supported plate take the form as seen in figure 3.16.

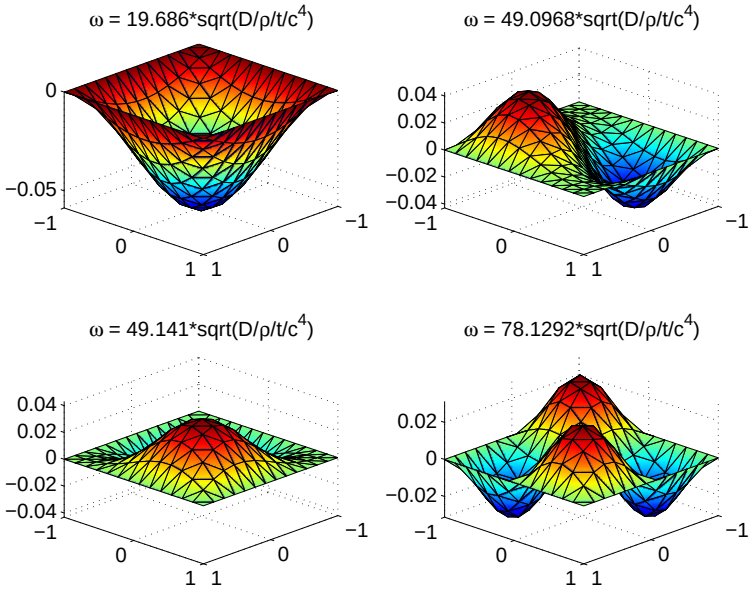

Figure 3.16: First mode shapes of a simply supported plate.

3.6.2 Membrane Finite Elements

A membrane finite element model is used for the membrane wing configuration. The derivation of the in-plane membrane finite element model is derived many times throughout the literature[81, 79] and is not repeated here. The derivation of the membrane CST model is given elsewhere[69] and is repeated here. Three-node Constant Strain Triangular (CST) membrane elements are used to model the out-of-plane deformation as well as the in-plane membrane prestress. The weak form of the membrane out-of-plane deformation equation is calculated as

$$
\begin{aligned}
0 = t \int_{\Omega} \left[\frac{\partial p}{\partial x} \left(\sigma_x \frac{\partial q}{\partial x} + \sigma_{xy} \frac{\partial q}{\partial y} \right) + \frac{\partial p}{\partial y} \left(\sigma_{xy} \frac{\partial q}{\partial x} + \sigma_y \frac{\partial q}{\partial y} \right) \right] dA \\
+ t \int_{\Omega} \left[-p \, \Delta P + \rho_w \frac{\partial^2 q}{\partial t^2} \right] dA \\
- t \oint_{\Gamma} \left[n_x p \left(\sigma_x \frac{\partial q}{\partial x} + \sigma_{xy} \frac{\partial q}{\partial y} \right) + n_y p \left(\sigma_{xy} \frac{\partial q}{\partial x} + \sigma_y \frac{\partial q}{\partial y} \right) \right] dA
\end{aligned}
\tag{3.32}
$$

where σ_x, σ_y, and σ_{xy} are the in-plane prestresses on the membrane, ΔP is the pressure distribution acting on the membrane, p is the weighting function, q is the out-of-plane deformation, ρ_w is the membrane density, and t is the membrane thickness which is assumed constant throughout the membrane. The weak form of the equation is manipulated to produce the stiffness K_s and mass M_s matrices as well as the force vector F_e as

$$K_s = t \int_\Omega \left(\frac{\partial N^T}{\partial x} \left(\sigma_x \frac{\partial N}{\partial x} + \sigma_{xy} \frac{\partial N}{\partial y} \right) + \frac{\partial N^T}{\partial y} \left(\sigma_{xy} \frac{\partial N}{\partial x} + \sigma_y \frac{\partial N}{\partial y} \right) \right) dx\, dy \tag{3.33}$$

$$M_s = t\, \rho_w \int_\Omega N^T N \, dxdy \tag{3.34}$$

$$F_e = t \int_\Omega N \, f_z dx \, dy \tag{3.35}$$

where N are the shape functions of the membrane element which are calculated as

$$N_i \left(x, y \right) = \frac{1}{2A^e} \left(\beta_i + \gamma_i x + \delta_i y \right) \tag{3.36}$$

with A^e as the element area, and β_i, γ_i, and δ_i calculated from the nodal positions of the element. The stiffness and mass matrices are evaluated using Gauss quadrature over the element domain.

3.6.2.1 Verification

The modes shapes, p, generated by the finite element code are compared against the first four modes of a clamped rectangular membrane of size $a \times b$. The analytical equations to the membrane modes are

$$p \left(\xi, \eta \right) = \sin \left(\frac{i \pi \xi}{a} \right) \sin \left(\frac{j \pi \eta}{b} \right) \tag{3.37}$$

where i and j are integers. The finite element model is validated by calculating the first four mode shapes of a rectangular membrane and compared to the analytical modes as shown in Figure 3.17.

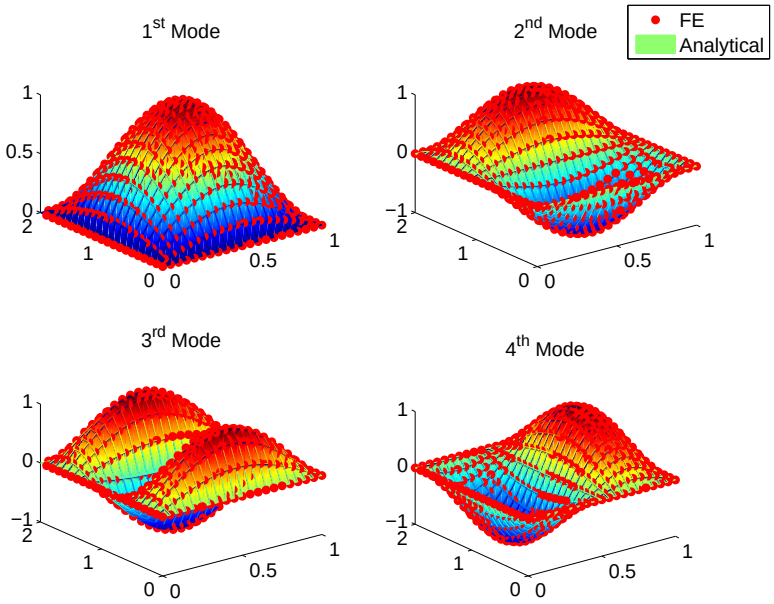

Figure 3.17: Membrane mode shapes

A linear prestress σ_x is applied to a rectangular wing as shown in Figure 3.18.

The first four modes of a membrane with constant σ_y and linearly varying σ_x pretension are shown in Figure 3.19 where the ratio of pretension along the two axes is $\frac{\sigma_{x0}}{\sigma_{y0}} = 10$. It is seen that the mode shape peaks tend to move toward the region where the pretention is smallest.

The pretension modes are compared against the Galerkin approximation to the membrane equation presented in Walker, et al.[52]. The centerline of the first mode shape is shown for different maximum values of σ_{x0} while σ_y is held constant as seen in Figure 3.20. The finite element approximation of the mode shapes matches up well with Galerkin approximation. As is seen in the figure, the peak of the mode shape tends to move toward the region of less prestress.

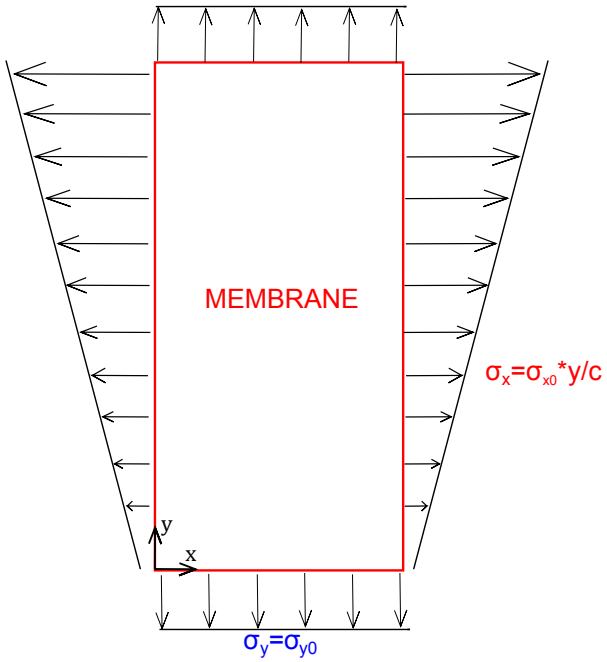

Figure 3.18: Application of linearly-varying prestress

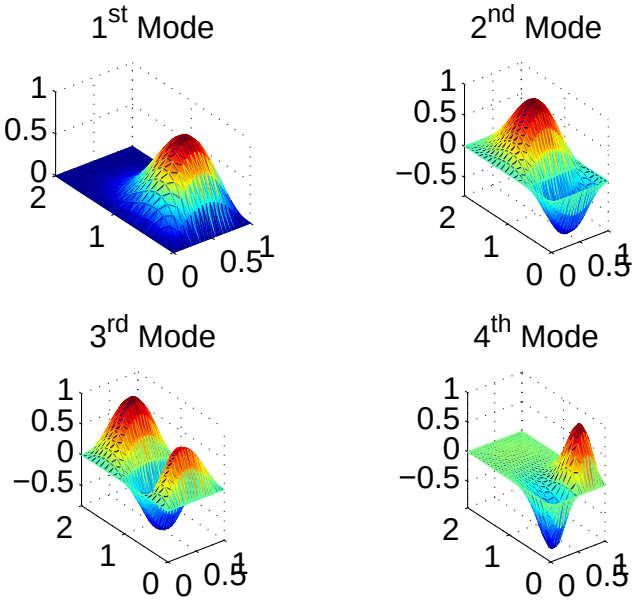

Figure 3.19: First four membrane modes for linearly varying pretension

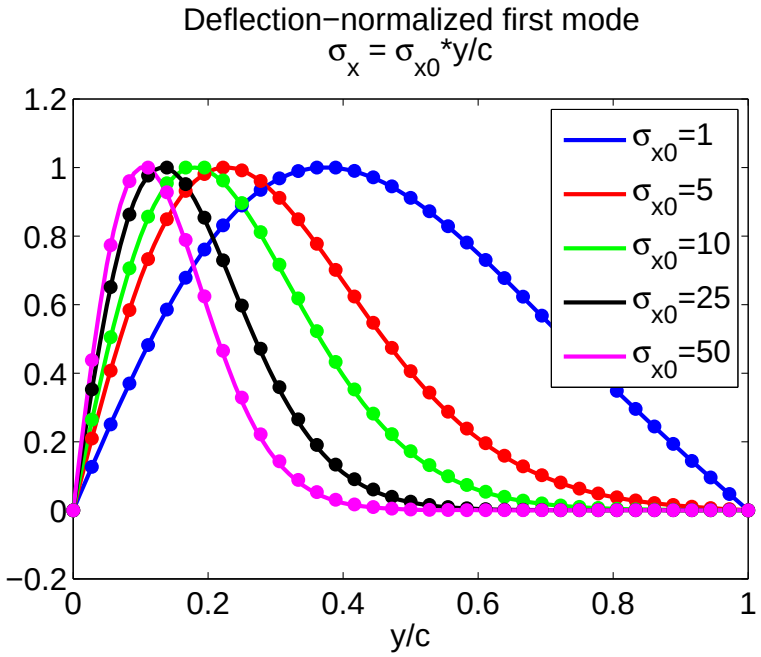

Figure 3.20: Mode shapes for different prestress magnitudes. Solid lines determined using Galerkin, dots calculated with finite elements

Chapter 4

Aeroelastic Coupling

The aeroelastic model couples the structural finite element model with the UVLM aerodynamic model. The coupling is valid for either the plate finite element model or the membrane finite element model with only a few modifications needed to convert between structural models. In the aeroelastic optimization, the unsteady vortex lattice method was the only aerodynamic model considered in the coupling, so the method by which Peters' aerodynamics can be coupled to the structural model is not discussed here.

4.1 Theory

The plate structural model is tightly coupled with the UVLM model. The equation of motion is

$$[M_s]\{\ddot{q}\} + [C_s]\{\dot{q}\} + [K_s]\{q\} = \{F_{inertia}\} + \{F_{aero}\} \tag{4.1}$$

where K_s is the structural stiffness matrix, M_s is the structural mass matrix, and C_s is the proportional structural damping, q is the vector of nodal degrees of freedom, $F_{inertia}$ are the inertial forces on the wing, and F_{aero} are the aerodynamic forces from the pressure acting on the wing. The second equation in the aeroelastic system is the no-penetration boundary condition on the wing. The velocities acting on a single panel of the wing are shown in Figure

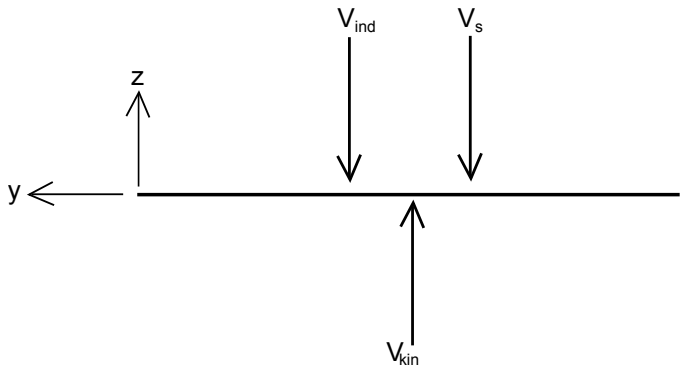

Figure 4.1: Velocities acting on the wing

4.1 and are given in equation form as

$$V_{ind} + V_s = V_{kin} \tag{4.2}$$

The no-penetration boundary condition, when applied over the entire wing grid, leads to the matrix equation

$$[A_b]\{\Gamma_b\} + [A_w]\{\Gamma_w\} + \{V_s\} = \{V_{kin}\} \tag{4.3}$$

where A_b and A_w are the influence coefficient matrices for the bound and wake vorticity, respectively. The right-hand-side of the equation has the velocity of the wing from the kinematics, including the freestream, rigid-body motion, and time-instantaneous wing deformation. The structural velocity component of the no-penetration equation is dependent on the time-derivative of the structural deformations as

$$V_s = [T_{V,q}]\{\dot{q}\} \tag{4.4}$$

where $T_{V,q}$ converts the nodal velocities into velocities at the control points of the UVLM model; it must be modified to work appropriately with the chosen structural model.

The velocity from the kinematics is based on the time-periodic kinematic parameters as well as the instantaneous angle-of-attack of the wing. The angle of attack, α, is a function

of the structural deformation on the wing as well as the time derivative of the rigid body motion at the control points h_{CP}. The total kinematic velocity acting on the i element is a function of the freestream velocity V_∞ and the rigid-body motion

$$V_{kin}^{k} = \left\{ \begin{array}{c} 0 \\ -V_\infty \cos(\alpha) \\ -V_\infty \sin(\alpha) \end{array} \right\} \cdot \vec{n}_i + \left\{ \begin{array}{c} 0 \\ -\dot{h}_{CP} \sin(\alpha) \\ -\dot{h}_{CP} \cos(\alpha) \end{array} \right\} \cdot \vec{n}_i \tag{4.5}$$

Only the component normal to the wing is used in the no-penetration boundary condition, which means that only the last component of the vector is used due to the UVLM simplifying assumptions. Grouping the kinematic velocity component on each control point into a single vector yields

$$\{V_{kin}\} = \left\{ -V_\infty \sin(\alpha) - \dot{h}_{CP} \cos(\alpha) \right\} \tag{4.6}$$

where α is the instantaneous angle of attack of each of the panels. The instantaneous angle of attack is based on the geometric angle of attack α_0 as well as the structural deformation as

$$\alpha = \alpha_0 + [T_{\alpha,q}] \{q\} \tag{4.7}$$

where $T_{\alpha,q}$ is an interpolation matrix that takes the nodal deformations and rotations and converts them to rotations at the control points of the UVLM grid. Like $T_{V,q}$, $T_{\alpha,q}$ changes with the structural model. Similarly, the rigid body motion at the control points is interpolated from the rigid body motion at the nodes as

$$\{h_{CP}\} = [T_{V,q}] \{h\} \tag{4.8}$$

The flat wake and small deformation assumptions are derived from the small angle assumption. If α_i is small then the kinematic velocity on the wing ultimately becomes

$$\{V_{kin}\} = -V_\infty \{\alpha_0\} - V_\infty [T_{\alpha,q}] \{q\} - [T_{V,q}] \left\{\dot{h}\right\} \tag{4.9}$$

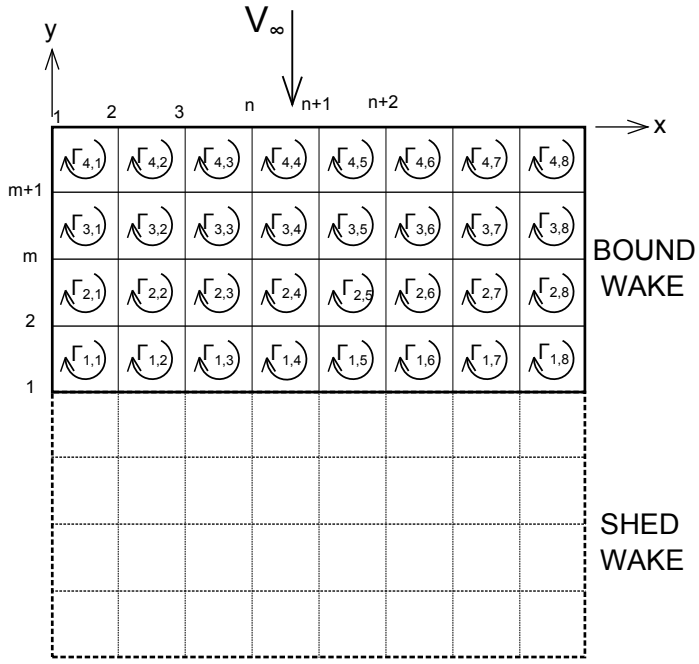

Figure 4.2: UVLM reference frame

The aerodynamic forces acting perpendicular on the wing are a function of the forces acting on the wing at the control points.

$$\{F_{aero}\} = [T_{a,CP}]\,\{\Delta P_{CP}\} \tag{4.10}$$

The matrix $T_{a,CP}$ converts the pressure at the control points to statically-equivalent nodal forces. The pressure on an element is based on the bound circulation as well as the time derivative of the bound circulation.

$$\Delta P^{i}_{m,n} = \rho \left[\|V_{m,n}\| \, \frac{(\Gamma_{m,n} - \Gamma_{m+1,n})}{c_{m,n}} + \frac{\partial}{\partial t} \left(\frac{\Gamma_{m,n} + \Gamma_{m+1,n}}{2} \right) \right] \tag{4.11}$$

The indices m and n are defined in Fig. 4.2. The pressure equation can then be cast into matrix/vectorial form as

$$\{\Delta p\} = \rho \, diag \left(\frac{\|V\|}{c} \right) [T_{\Gamma 1}]\,\{\Gamma_b\} + \rho\,[T_{\Gamma 2}]\,\left\{\dot{\Gamma}_b\right\} \tag{4.12}$$

where $T_{\Gamma 1}$ and $T_{\Gamma 2}$ are matrices that algebraically manipulate the bound vorticity, ρ is the fluid density, and $diag\left(\frac{\|V\|}{C}\right)$ is a diagonal matrix containing the magnitude of the velocity at each of the control points divided by the chord of the corresponding panel. The aerodynamic force vector is then written as

$$\{F_{aero}\} = \rho\,[T_{a,CP}]\ \text{diag}\left(\frac{\|V\|}{c}\right)[T_{\Gamma 1}]\,\{\Gamma_b\} + \rho\,[T_{a,CP}]\,[T_{\Gamma 2}]\,\left\{\dot{\Gamma}_b\right\} \tag{4.13}$$

The inertial force vector in the aeroelastic equation is from the prescribed motion of the wing. The inertial forces are a function of the second time derivative of the rigid body motion at the nodes h as

$$\{F_{inertial}\} = -\,[M_s]\,\left\{\ddot{h}\right\} \tag{4.14}$$

Eq. 4.1, Eq. 4.13, and Eq. 4.14 can be combined into the tightly coupled aeroelastic equation as

$$\begin{aligned}&[M_s]\,\{\ddot{q}\} + [C_s]\,\{\dot{q}\} + [K_s]\,\{q\} = \\ &-\,[M_s]\,\left\{\ddot{h}\right\} + \rho\,[T_{a,CP}]\ \text{diag}\left(\frac{\|V\|}{c}\right)[T_{\Gamma 1}]\,\{\Gamma_b\} + \rho\,[T_{a,CP}]\,[T_{\Gamma 2}]\,\left\{\dot{\Gamma}_b\right\}\end{aligned} \tag{4.15}$$

The final equation in the coupling of the aerodynamics and the structure is the time-dependent shedding of the wake vorticity. The wake vorticity at the new time step is dependent on the bound circulation at the trailing edge of the wing and the wake vorticity for the previous time. The discrete time form of the shedding equation is represented as

$$\{\Gamma_w\}^{t+\Delta t} = [B_1]\,\{\Gamma_b\}^t + [B_2]\,\{\Gamma_w\}^t \tag{4.16}$$

which can be converted to continuous time via central differencing

$$\frac{\Delta t}{2}\left([B_1]\,\left\{\dot{\Gamma}_b\right\} + [[B_2] + [I]]\,\left\{\dot{\Gamma}_w\right\}\right) = [B_1]\,\{\Gamma_b\} + [B_2 - I]\,\{\Gamma_w\} \tag{4.17}$$

where I is the identity matrix, Δt is the time step, and B_1 and B_2 are matrices that shed

the wake downstream. Combining Eqs. 4.3-4.9 and solving for bound circulation gives

$$\{\Gamma_b\} = -[A_b]^{-1}[A_w]\{\Gamma_w\} - V_\infty[A_b]^{-1}\{\alpha_0\} \\ - V_\infty[A_b]^{-1}[T_{\alpha,q}]\{q\} - [A_b]^{-1}[T_{V,q}]\left\{\dot{h}\right\} - [A_b]^{-1}[T_{V,q}]\{\dot{q}\} \quad (4.18)$$

The value of the bound circulation Γ_b from Eq. 4.18 is used in the wake-shedding equation and the equation of motion. The like terms are grouped together and the two equations simplify to

$$\left[\hat{M}\right]\{\ddot{q}\} + [C_3][A_w]\left\{\dot{\Gamma}_w\right\} = -[C_2][A_w]\{\Gamma_w\} + \left[\hat{K}_1\right]\{q\} + \left[\hat{C}_1\right]\{\dot{q}\} + \{F_1(t)\} \quad (4.19)$$

$$[C_{\Gamma_w}]\left\{\dot{\Gamma}_w\right\} + \frac{\Delta t}{2}[C_1][T_{V,q}]\{\ddot{q}\} = [K_{\Gamma_w}]\{\Gamma_w\} + \left[\hat{C}_2\right]\{\dot{q}\} + \left[\hat{K}\right]\{q\} + \{F_2(t)\} \quad (4.20)$$

In state-space form, these equations take the form

$$\begin{bmatrix} 0 & \hat{M} & C_3A_w \\ 0 & -\frac{\Delta t}{2}C_1T_{V,q} & C_{\Gamma_w} \\ I_q & 0 & 0 \end{bmatrix} \begin{Bmatrix} \dot{q} \\ \ddot{q} \\ \dot{\Gamma}_w \end{Bmatrix} = \quad (4.21)$$

$$\begin{bmatrix} \hat{K}_1 & \hat{C}_1 & -C_2A_w \\ \hat{K}_2 & \hat{C}_2 & K_{\Gamma_w} \\ 0 & I_q & 0 \end{bmatrix} \begin{Bmatrix} q \\ \dot{q} \\ \Gamma_w \end{Bmatrix} + \begin{Bmatrix} F_1(t) \\ F_2(t) \\ 0 \end{Bmatrix}$$

where the new variables are defined as

$$C_1 = [B_1][A_b]^{-1} \quad (4.22)$$

$$C_2 = \rho[T_{a,CP}]\ \text{diag}\left(\frac{\|V\|}{c}\right)[T_{\Gamma 1}][A_b]^{-1} \quad (4.23)$$

$$C_3 = \rho[T_{a,CP}][T_{\Gamma 2}][A_b]^{-1} \quad (4.24)$$

$$\hat{M} = [M_s] + [C_3]\,[T_{V,q}] \tag{4.25}$$

$$\hat{K}_1 = -V_\infty\,[C_2]\,[T_{\alpha,q}] - [K_s] - \dot{V}_\infty\,[C_3]\,[T_{\alpha,q}] \tag{4.26}$$

$$\hat{K}_2 = V_\infty\,[C_1]\,[T_{\alpha,q}] - \dot{V}_\infty \frac{\Delta t}{2}\,[C_1]\,[T_{\alpha,q}] \tag{4.27}$$

$$C_{\Gamma_w} = \frac{\Delta t}{2}\,[[B_2] + [I]] - \frac{\Delta t}{2}\,[C_1]\,[A_w] \tag{4.28}$$

$$K_{\Gamma_w} = [B_2 - I] - [C_1]\,[A_w] \tag{4.29}$$

$$\hat{C}_1 = -V_\infty\,[C_3]\,[T_{\alpha,q}] - [C_s] - [C_2]\,[T_{V,q}] \tag{4.30}$$

$$\hat{C}_2 = V_\infty \frac{\Delta t}{2}\,[C_1]\,[T_{\alpha,q}] - [C_1]\,[T_{V,q}] \tag{4.31}$$

$$\begin{aligned} F_1(t) = &-[C_3]\left(\dot{V}_\infty\,\{\alpha_0\} + V_\infty\,\{\dot{\alpha}_0\}\right) - V_\infty\,[C_2]\,\{\alpha_0\} \\ &- [C_2]\,[T_{V,q}]\left\{\dot{h}\right\} + [-[M_s] - [C_3]\,[T_{V,q}]]\left\{\ddot{h}\right\} \end{aligned} \tag{4.32}$$

$$\begin{aligned} F_2(t) = &-\frac{\Delta t}{2}\dot{V}_\infty\,[C_1]\,\{\alpha_0\} - \frac{\Delta t}{2}V_\infty\,[C_1]\,\{\dot{\alpha}_0\} - V_\infty\,[C_1]\,\{\alpha_0\} \\ &- [C_1]\,[T_{V,q}]\left\{\dot{h}\right\} + \frac{\Delta t}{2}\,[C_1]\,[T_{V,q}]\left\{\ddot{h}\right\} \end{aligned} \tag{4.33}$$

4.1.1 Time-Periodic Solution

The state space form of Eq. 4.21 takes the simple form

$$[A]\,\{\dot{x}\} + [B]\,\{x\} = \{F(t)\} \tag{4.34}$$

where A and B are time-invariant matrices. The forcing vector is sinusoidal due to the harmonic flapping motion

$$\{F(t)\} = \{F_c\}\,\cos(\omega t) + \{F_s\}\sin(\omega t) \tag{4.35}$$

Therefore, the time-periodic response will also be sinusoidal with the form

$$x = x_c \cos(\omega t) + x_s \sin(\omega t) \tag{4.36}$$

The equations are turned into a linear system to solve for the response as

$$\begin{bmatrix} [B] & \omega [A] \\ -\omega [A] & [B] \end{bmatrix} \begin{Bmatrix} x_c \\ x_s \end{Bmatrix} = \begin{Bmatrix} F_c \\ F_s \end{Bmatrix} \tag{4.37}$$

The thrust, T, and input power, P_{in} are calculated using the results of the previous calculation. The input power for the plate-like wing is calculated by multiplying the root bending moment, M_{root} with the flapping speed $\dot{\gamma}$.

$$T = \rho b \left(\text{diag}(-V_{ind}) [T_{\Gamma 1}] \{\Gamma_b\} + \text{diag}\left([T_{V,q}] \left\{ \dot{h} + \dot{q} \right\} \right) [T_{\Gamma 1}] \{\Gamma_b\} \right) \tag{4.38}$$

$$P_{in} = M_{root} \dot{\gamma} \tag{4.39}$$

The power calculation can equivalently be expressed as the summation of the negative aerodynamic power with the time-derivative of the kinetic energy and potential energy as

$$\begin{aligned} P_{in} = \frac{dP_E}{dt} + \frac{dK_E}{dt} - P_{aero} &= \{\dot{q}\}^T [K_s] \{q\} \\ &+ \left\{ \ddot{h} \right\}^T [M_s] \left\{ \dot{h} \right\} + \left\{ \dot{h} \right\}^T [M_s] \{\ddot{q}\} + \left\{ \ddot{h} \right\}^T [M_s] \{\dot{q}\} + \{\ddot{q}\}^T [M_s] \{\dot{q}\} - P_{aero} \end{aligned} \tag{4.40}$$

4.2 Aeroelastic Validation - Plate

4.2.1 Static Aeroelastic Analysis

For a deformable cantilevered wing in a constant freestream and at a angle of attack, the static deflection of the wing is calculated. A quasi-steady form of Theodorsen's unsteady aerodynamics and an assumed modes method is used to validate the results for the plate

finite element - UVLM coupled model. Three orthogonal bending modes and three orthogonal twisting modes are used to model the structural deformation. The lift and moment on the airfoil are written as

$$L = qc\left[C_{l_0} + C_{l_\alpha}\left(\alpha_0 + \theta_x\right)\right] \tag{4.41}$$

$$M = qc^2 C_{M_0} \tag{4.42}$$

The static form of the assumed modes method can be written in the following form

$$\begin{bmatrix} K^{(1)} & -K^{(12)} \\ -K^{(12)} & K^2 \end{bmatrix} \begin{Bmatrix} v \\ \theta \end{Bmatrix} = \begin{Bmatrix} f_i \\ \tau_i \end{Bmatrix} \tag{4.43}$$

where

$$K_{ij}^{(1)} = \int_0^l EI(x)\phi_i^v(x)''\phi_j^v(x)''\,dx \tag{4.44}$$

$$K_{ij}^{(12)} = \int_0^l EI(x)\phi_i^v(x)''\left[z_{ea}\left(x\right)\phi_j^\theta(x)''\right]\,dx \tag{4.45}$$

$$K_{ij}^{(2)} = \int_0^l GJ(x)\phi_i^\theta(x)'\phi_j^\theta(x)' + EI\left[z_{ea}\left(x\right)\phi_i^\theta(x)''\right]\left[z_{ea}\left(x\right)\phi_j^\theta(x)''\right]\,dx \tag{4.46}$$

$$f_i = \int_0^l L\,\phi_i^v(x)\,dx \tag{4.47}$$

$$\tau_i = \int_0^l \left(M - z_{ac}L\right)\phi_i^\theta(x)\,dx \tag{4.48}$$

The assumed bending modes ϕ_i^v are polynomials that are orthogonal with respect to the others. Similarly, the assumed torsional modes ϕ_i^θ are orthogonal polynomials. The structural componen t of the equations are decoupled since the elastic axis and the aerodynamic center are coincident ($z_{ea} = 0$), but the full aeroelastic equations are coupled through the aerodynamics. Ultimately, the quasi-steady - assumed modes coupled system is

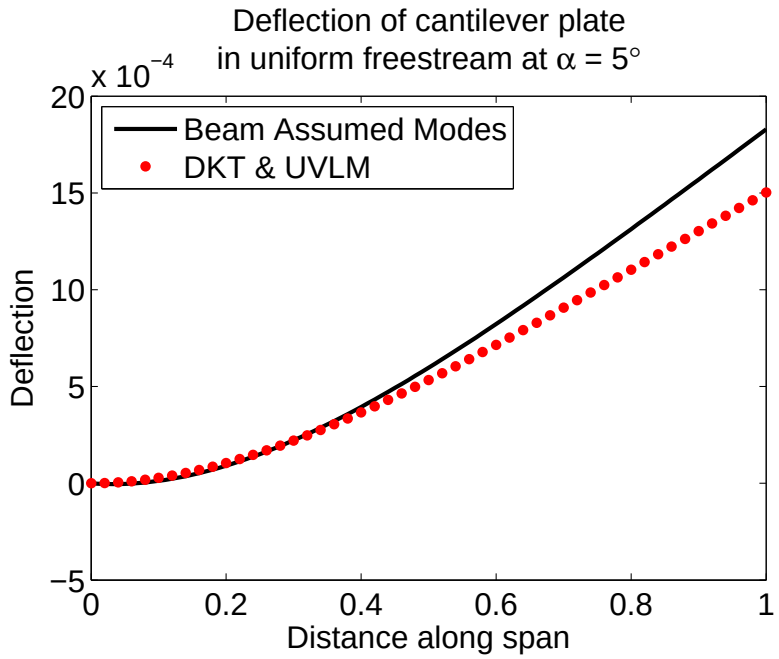

Figure 4.3: Static aeroelastic validation

$$\begin{bmatrix} K^{(1)} & -qcC_{l_\alpha} f_{ij}^0 \\ 0 & K^{(2)} + z_{ac} qcC_{l_\alpha} M_{ij}^0 \end{bmatrix} \begin{Bmatrix} v \\ \theta \end{Bmatrix} = \begin{Bmatrix} qcC_{l_\alpha} \alpha_0 f_i^0 \\ -z_{ac} qcC_{l_\alpha} \alpha_0 M_i^0 \end{Bmatrix} \tag{4.49}$$

The differences in the overall deflection are due to the different aerodynamics used in each case. The blade element theory applies the same load at the tip as it would at the midspan of the wing, whereas the UVLM model is affected by the three-dimensional effects and there is decreased loading at the tip of the wing.

4.2.2 Plunging Wing Deformation

The dynamic aeroelastic analysis is validated using the experimental results of Heathcote, et al.[1] and the computational results of Chimakurthi, et al.[82]. Heathcote took three rubber airfoils and reinforced one with a 1mm thick aluminum (70 GPa) plate, one with a 1mm thick steel (210 GPa) plate, and one with two steel rods to make the wing effectively rigid. The wings were then sinusoidally plunged in water and the tip deflection of each wing was measured for a range of reduced frequencies. They then fit a sinusoidal curve to

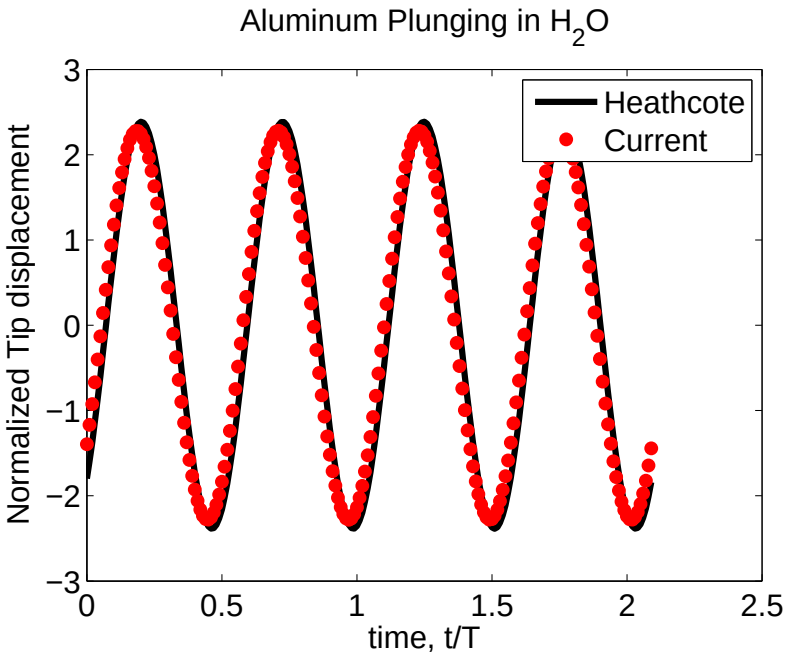

Figure 4.4: Tip deflection of aluminum plate plunging in water

the tip deformation in the form of $a_{tip}\cos(\omega t + \psi_{tip})$ where a_{tip} is the magnitude of the tip displacement which includes the rigid-body motion and deformation and ψ_{tip} is phase offset relative to the plunging.

The current aeroelastic analysis is used to compute the time-harmonic results of the steel and aluminum wings plunging in water, which are compared to the Heathcote results in Figure 4.4 and Figure 4.5. The computational results from Chimakurthi are included in Figure 4.5.

The current aeroelastic analysis is used to calculate the values of a_{tip} and ψ_{tip} of the aluminum and steel wings at different reduced frequencies. The values for tip deformation and phase lag are shown in Figure 4.6 and Figure 4.7, respectively, and compared against the experimental results of Heathcote. The aeroelastic model closely predicts both the magnitude of the tip deformation as well as the phase lag. The error in the phase lag exacerbates the inaccuracies in the magnitude of the tip displacement. When the phase lag increases above 90° the magnitude of the tip displacement decreases. Since the current model predicts that the phase of the aluminum goes above 90° at a higher reduced frequency, then the peak of

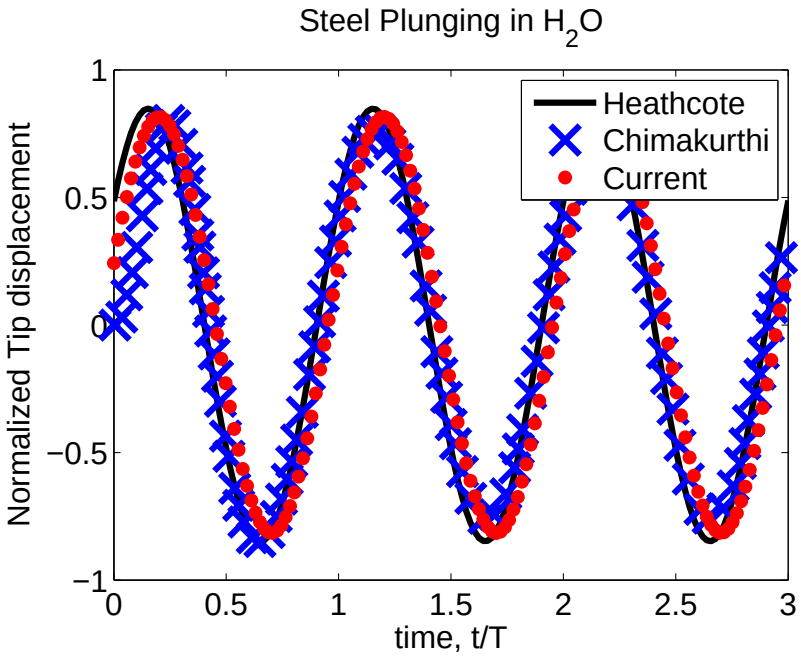

Figure 4.5: Tip deflection of steel plate plunging water

the tip dispacement is shifted to the right for the aeroelastic model.

4.2.3 Flutter

The current plate-UVLM model is set in a constant freestream and the flutter velocity is calculated for a rectangular wing with varying aspect ratios. The results from the current analysis are compared to the flutter calculations done by Tang, et al.[83] in Figure 4.8. Tang, et al. uses an unsteady vortex lattice method and couples it to an assumed modes plate model. The modes of a beam in vibration are used to describe the chordwise and spanwise bending of the plate structural model. The two methods differ in the flutter velocity prediction, especially for the low aspect ratio wings. The difference is attributed to the choice of structural models; the beam modes are less accurate at the lower aspect ratios.

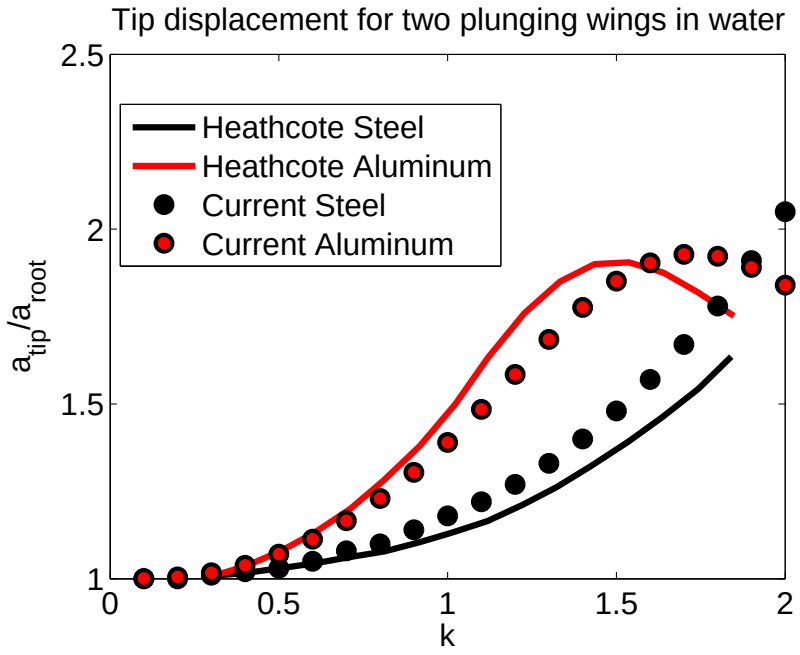

Figure 4.6: Comparison of tip displacement for two different wings.

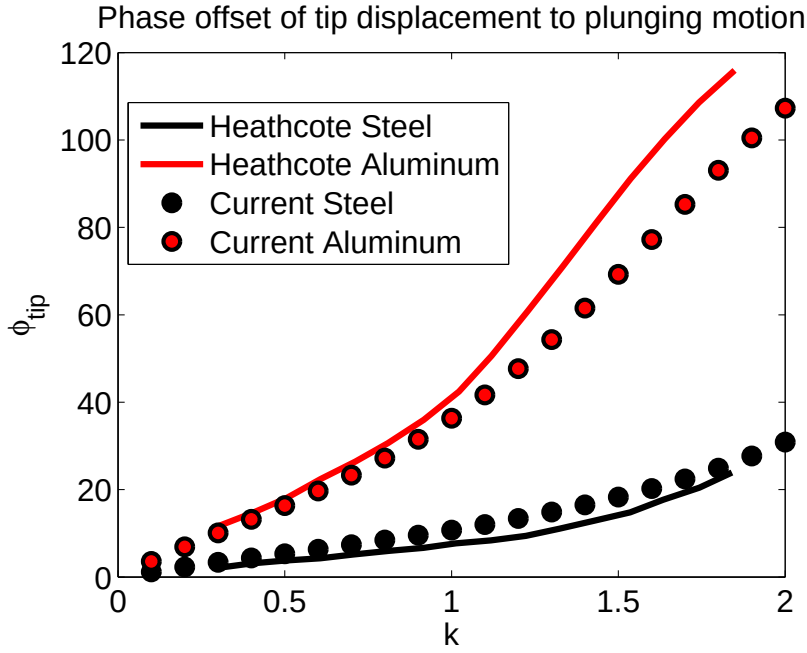

Figure 4.7: Comparison of phase offset for two different wings

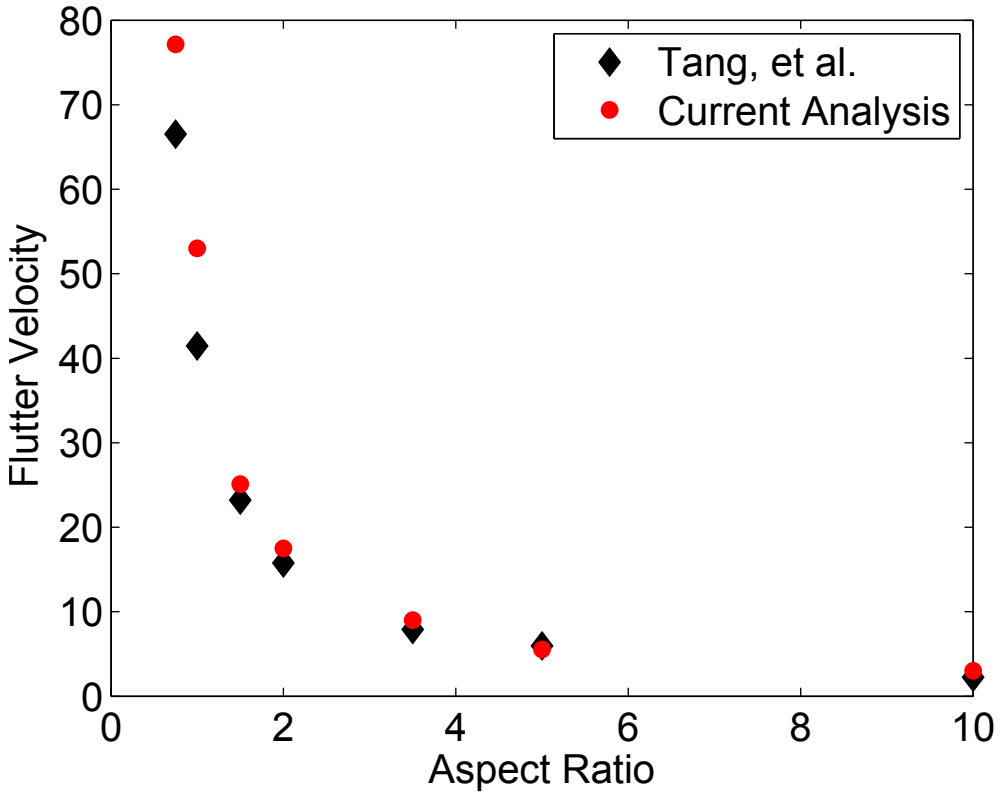

Figure 4.8: Plate flutter calculations comparing Tang, et. al and current model

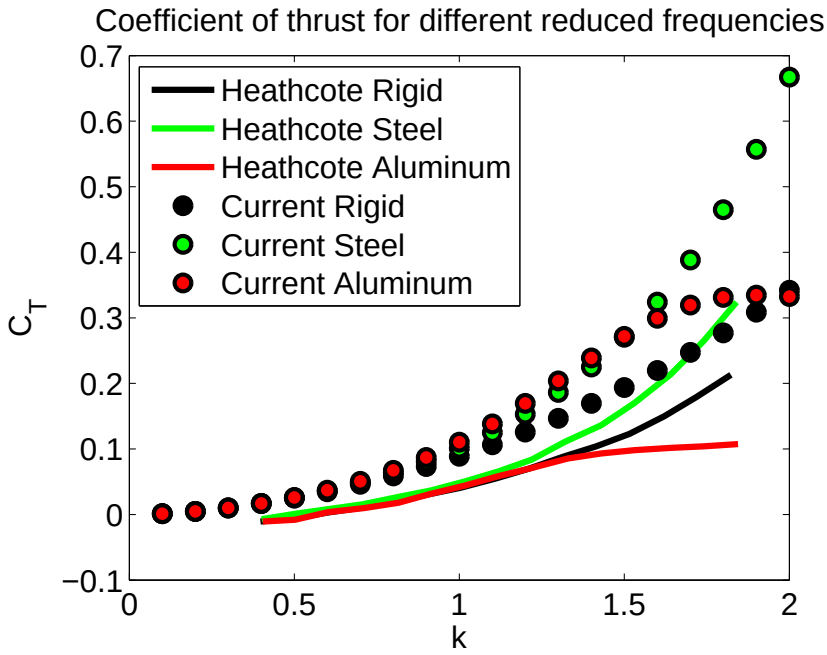

Figure 4.9: Thrust produced for wings with different stiffnesses

4.2.4 Thrust Prediction

The plate aeroelastic model is again compared against the experimental work of Heathcote, et al.[1] Heathcote measured the thrust force produced by the rigid, aluminum, and steel wings during the plunging cycle. The current analysis is compared against the experimental work in Figure 4.9. The current model overpredicts the thrust calculated by the plunging wing since the UVLM model does not include viscous effects.

4.3 Aeroelastic Validation - Membrane

The aeroelastic system is validated against the experimental work of Stearman[64]. A membrane is clamped at the leading edge and trailing edge while free on the sides and subjected to a uniform flow. A pretension parallel to the freestream is applied and varied to test its effects on the flutter speed. Stearman tested several cases with different membrane thickness and span, but here the flutter calculations are shown for only the experimental set up given in Table 4.1. Some material properties are not given explicitly in paper and are approximated

Table 4.1: Experimental set-up for flutter validation

Variable	Stearman (English)	Stearman (Metric)
thickness	0.001 in	0.0000254 m
chord	2.36 ft	0.719238 m
span	6 in	0.1524 m
Young's Modulus	740 ksi	5.18 GPa
Mylar density	86.774 lb/ft^3	1390 kg/m^3
Membrane Pre-stress	1 lb/ft	14.58 N/m
dynamic pressure	1 lb/ft^2	47.88 N/m^2

here.

The computational flutter results are shown in Figure 4.10. The flutter calculations were first performed with zero structural damping on the system, which led to a large difference as compared to the experimental analysis. However, Gibbs, et al.[68] found that a small amount of structural damping is required in a nonlinear plate-membrane system to correctly calculate the flutter of a clamped-clamped-clamped-free membrane. So a small amount of structural damping was added to the current system and the newly calculated flutter speeds are indicated by the blue dots. The damping greatly improves the flutter prediction and is therefore included in the membrane aeroelastic analysis.

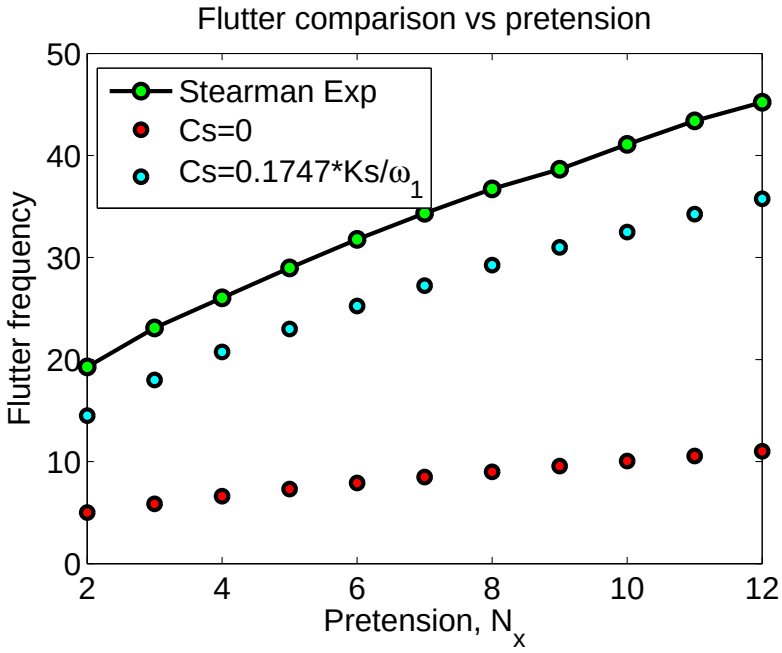

Figure 4.10: Flutter comparison to results from Stearman, t = 0.001 in

Chapter 5

Rigid Shape Optimization

In this chapter, shape optimization is performed on a rigid flapping wing using three aerodynamic models: Peters' quasi-steady aerodynamics[9] with and without an assumed inflow model, and unsteady vortex lattice method. Using quasi-steady aerodynamics, there are two kinematic configurations that are considered, forward flapping flight and hovering. For the the UVLM aerodynamics model, only forward flapping flight kinematics is considered due to the inherent limitations of the aerodynamic model.

5.1 Quasi-Steady Aerodynamics

In performing shape optimization for MAVs, there is a need to use constraints with physical meaning in order to gain deeper understanding of the problem. Peak power was selected as the nonlinear constraint for this problem, as was done in previous studies[27]. Peak power is well suited to this problem because it is representative of the maximum power that can be transmitted by the motor. Using a constraint that depends on transient behavior, such as peak power, can add significant cost to the problem because each discretized time point must satisfy the constraint. [84, 85]. However, the power is sinusoidal in time at twice the flapping frequency about an average power, and only the peak power, which is the sum of the average power and amplitude of oscillation, needs to be constrained.

A planform area objective function was added to the optimization formulation in an effort to represent the size constraints imposed by mission specifications. The wing weight is directly proportional to the wing planform area since a constant wing thickness and material density are assumed. By minimizing the wing weight, more weight can be purposed for payload on the MAV. The optimization problem thus has three objectives: minimize area, minimize peak power, and maximize thrust.

The multiobjective formulation of the problem leads to a Pareto front of best designs. The Pareto front of optimal designs was found using the ϵ-constraint method[86, 87, 88], where the power and area were constrained to be less than some value ϵ and the average coefficient of thrust $C_{T,avg}$ was the objective for which the design was optimized. The constraints on area and power were then slowly relaxed to calculate the Pareto front. Aerodynamic thrust generation was used as the objective function for the forward flight case, while lift was used as the objective for the hover kinematics case. The ϵ-constraint optimization problem is written formally as

$$\begin{gathered}
min: \ -C_{T,avg} \\
st: \ C_{P,peak} \leq \epsilon_1 \\
A \leq \epsilon_2 \\
-\tfrac{\bar{s}}{2} \leq \xi_4 \leq \xi_3 \leq \xi_2 \leq \xi_1 \leq \tfrac{\bar{s}}{2} \\
-\tfrac{\bar{s}}{2} \leq \xi_5 \leq \xi_6 \leq \xi_7 \leq \xi_8 \leq \tfrac{\bar{s}}{2} \\
-\tfrac{\bar{c}}{2} \leq \eta_6 \leq \eta_5 \leq \eta_4 \leq \eta_3 \leq \tfrac{\bar{c}}{2} \\
-\tfrac{\bar{c}}{2} \leq \eta_7 \leq \eta_8 \leq \eta_1 \leq \eta_2 \leq \tfrac{\bar{c}}{2} \\
\xi_6 \leq \xi_2 \\
\xi_3 \leq \xi_7 \\
\eta_5 \leq \eta_1 \\
\eta_8 \leq \eta_4
\end{gathered} \tag{5.1}$$

where the peak power and area were constrained by ϵ_1 and ϵ_2. During the optimization, the average thrust and peak power were used as the objective functions rather than the nondimensional thrust and power coefficients. Subsequently the Pareto surfaces were expressed in

terms of the coefficients and the normalized area. The coefficient of power and the coefficient of thrust are calculated as

$$C_P = \frac{P}{\frac{1}{2}\rho V_\infty^2 s^3 \omega} \tag{5.2}$$

$$C_T = \frac{T}{\frac{1}{2}\rho V_\infty^2 s^3 \omega} \tag{5.3}$$

where s is the upper bound of the wing span. The normalized area is the total planform area divided by area of the largest possible planform that could be created by the modified Zimmerman method. The side constraints and linear relations among the design variables were created by the modified Zimmerman parameterization.

Two kinematic configurations were considered in the planform optimization studies: forward flapping flight and hovering. For each kinematic configuration, planform optimization was performed with and without the assumed inflow. The power and area constraints were selected so that only a small section of the design space was considered.

Previous optimization formulations for MAVs have focused on the optimization of other objectives such as propulsive efficiency[33, 49] and power[27, 16, 59]. The decision of how to formulate the multiobjective problem depends on the performance metric of interest. In selecting thrust and lift as the primary objective function, the optimal designs will produce wing planforms that best accelerate the MAV with some battery power constraints. If power were selected as the primary objective function, then the planforms would allow the MAV to prolong battery life while just meeting the thrust or lift needs.

5.1.1 Flapping Kinematics - No Inflow

Initially, the multiobjective optimization was performed without considering the induced drag effects. In doing so, the analytical sensitivities derived in the Appendix could be used to verify the results. The modified Zimmerman method was constrained to produce MAV wing shapes that were symmetric about the mid-chord. The Pareto front of designs with the markers' colors indicating constraint activity is shown in Fig. 5.1.

The green dots indicate that the power constraint was active while the area constraint was

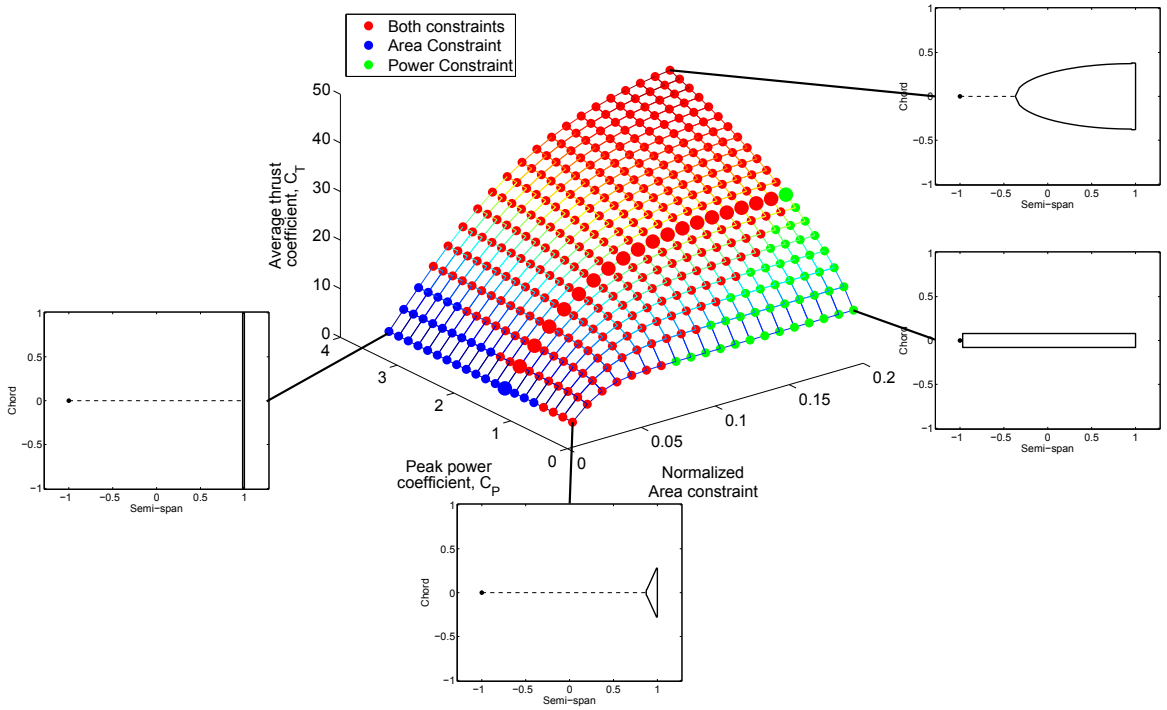

Figure 5.1: Pareto front of designs for flapping, symmetric planforms with no inflow

inactive. The blue dots indicate that the area constraint was active and power was not, while the red dots indicate that both constraints were active. Each constraint becomes inactive when the other drives the optimization. The activity of the constraints was determined by the magnitude of the corresponding Lagrange multipliers. If the Lagrange multiplier is less than a finite threshold magnitude of 0.05, then the constraint was assumed to be inactive. If both of the Lagrange multipliers are non-zero, then the planform design is Pareto optimal[88, 86]. For the cases where one of the constraints is inactive, the planform designs are weakly Pareto optimal. A comparison of the Lagrange multiplier magnitudes for area and power is shown in Fig. 5.2.

The effect of constraint activity on optimal planform design can be seen in Fig. 5.3. A slice of the Pareto surface is taken at $C_P = 1.3623$, indicated by the highlighted dots in Fig. 5.1. The various planforms show how the optimal design changes for a constant power constraint and various area constraints. When only the area constraint is active, then the thrust is optimized by pushing all of the blade elements as far from the hinge as possible

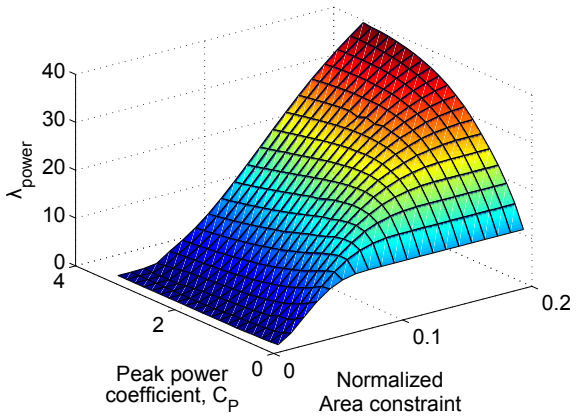

(a) Magnitude of the Lagrange multiplier corresponding to peak power for symmetric shapes

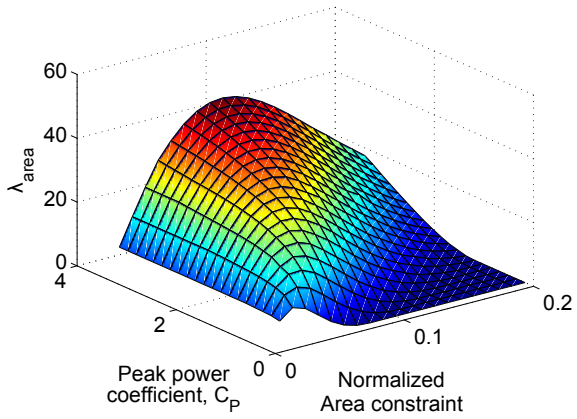

(b) Magnitude of the Lagrange multiplier corresponding to area for symmetric shapes

Figure 5.2: Lagrange multiplier values for symmetric designs.

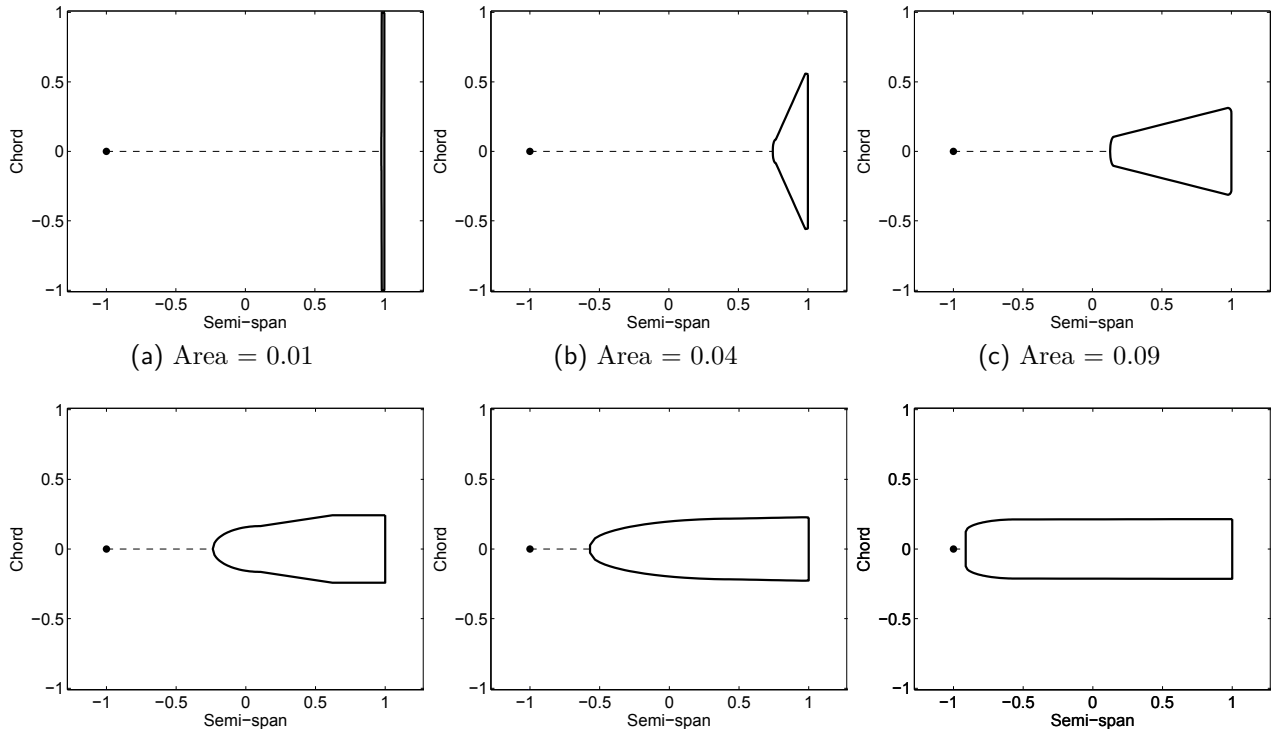

(a) Area = 0.01 (b) Area = 0.04 (c) Area = 0.09

(d) Area = 0.12 (e) Area = 0.15 (f) Area = 0.20

Figure 5.3: Optimal, symmetric flapping wing designs for different area constraints at a constant power constraint of $C_p = 1.3623$ and with no assumed inflow

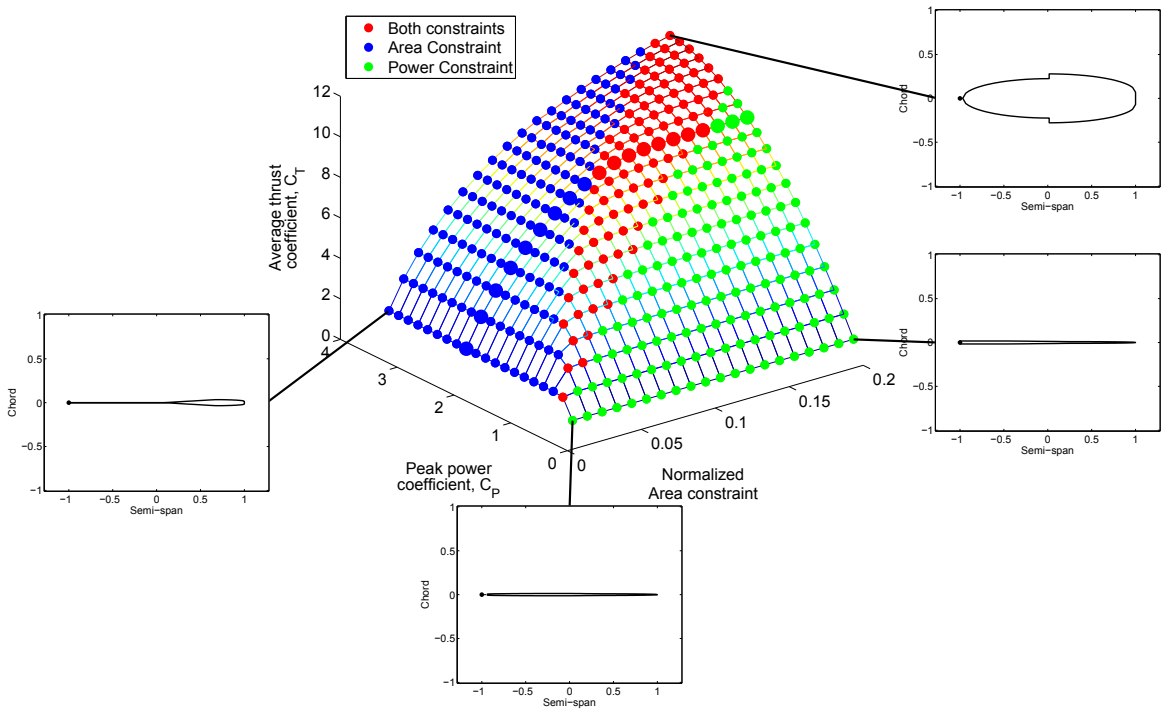

Figure 5.4: Pareto front of designs for flapping, symmetric wings, with 3D inflow effects

and by maximizing the chord, verifying the conclusions from the analytical sensitivities in the appendix A. As the area constraint is relaxed and the power constraint is also active, the optimizer allocates more wing area toward the hinge point and the planforms change from rectangular to triangular to half-ellipse. The optimal wing shape has increasingly smaller chord and longer span as the power constraint takes over as the driving force behind the designs.

5.1.2 Flapping Kinematics - Inflow

The aerodynamics were modified to account for the induced drag effects. The Pareto surface is shown in Fig. 5.4. The inflow reduces the maximum average thrust generated by nearly 70%. Also, the inflow changes the multiobjective optimization such that there is a narrower range of power-area combinations where both constraints are active.

A cut of the Pareto surface was made at $C_P = 2.0434$ to illustrate how the optimal planform changes as the area constraint is relaxed. For a small area constraint, the optimal

wing planform resembles a teardrop as in Fig. 5.5a. The teardrop planform differs from the planform in Fig. 5.3a due to the assumed inflow model. As the area constraint is relaxed and the peak power constraint becomes active, the optimizer shifts the wing area toward the hinge. The optimal planform resembles a triangle with a rounded tip when only the peak power constraint is active in Fig. 5.5f. The trend of either minimizing the the blade chord or the root-to-blade distance is especially prevalent in the cases where only the power constraint is active as in Fig. 5.5f. The blade chord values vary inversely with the distance from the root.

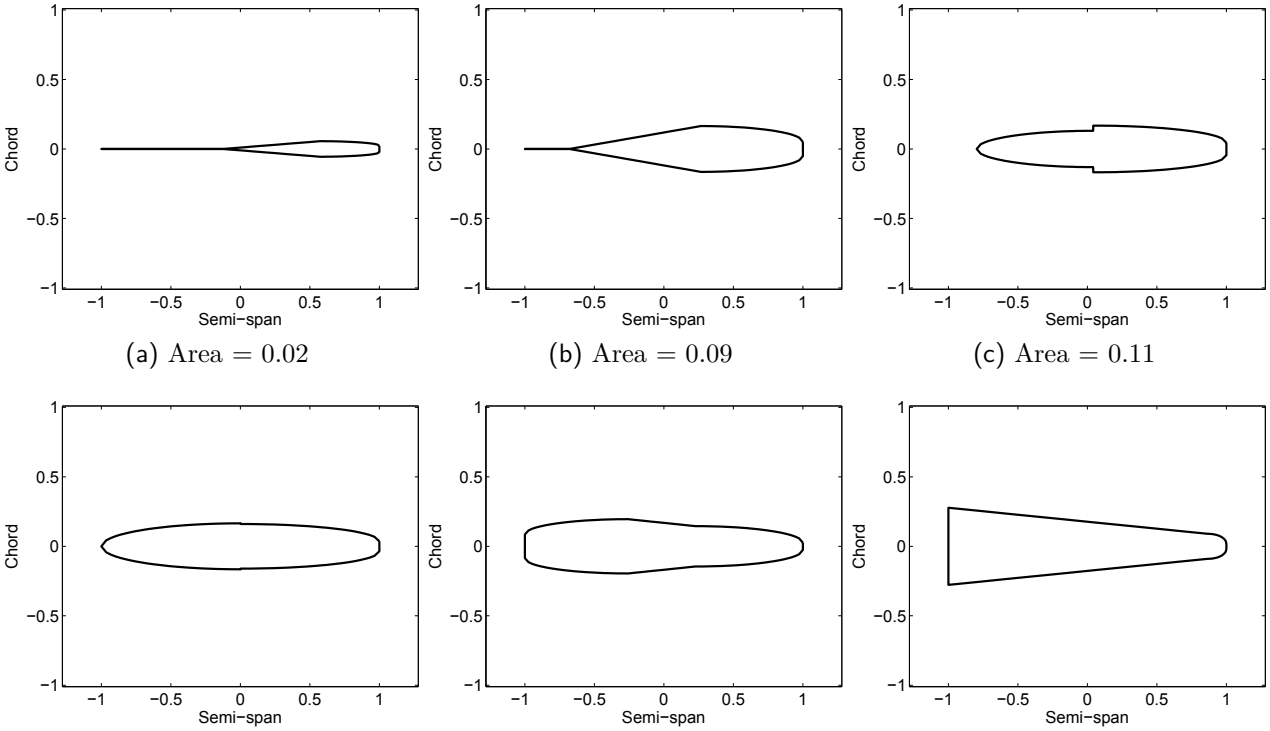

(a) Area = 0.02 (b) Area = 0.09 (c) Area = 0.11

(d) Area = 0.13 (e) Area = 0.15 (f) Area = 0.19

Figure 5.5: Optimal, symmetric flapping wing designs for different area constraints at a constant power constraint of $C_p = 2.0434$ and with 3D inflow

The span for each of the Pareto optimal planforms was maximized because of the assumed inflow model and the blade element discretization. The optimizer minimized the induced drag from the inflow model to increase the thrust. Due to the discrete lifting line model, there is a minor but finite decrease in drag with increase in the distance between each of the blade

elements. The fixed number of blades were distributed between the wing root and wing tip. So, maximizing the root-to-tip distance will increase the spacing of the blade elements and decrease the induced drag on the planform. For this reason, the teardrop shape in Fig. 5.5a has the infinitesimal tail from the hinge line to the wing root.

The optimizer attempted to minimize the induced drag through an elliptic lift distribution. The lift distribution is proportional to the chord and effective angle of attack of each blade element, which is itself proportional to r_{BL} for the element. The optimizer selects those parameters to get close to an elliptic lift distribution while staying within the geometric and nonlinear constraints.

The evolution of shapes between the cases where only one constraint is active is seen in Figs. 5.5c-5.5e. The three cases shown are examples of the trade-off that occurs between the area constraint and the power constraint during the optimization.

The blade element discretization is also an important factor in determining the final modified Zimmerman planform. The planform in Fig. 5.5c has a small discontinuity in the leading and trailing edges. During the optimization procedure, the value of the blade chords was determined by calculating the η position of the edges of each blade element and then averaging them together to find the η position of the center line leading and trailing edges for each blade element. So, by comparing the final planform and the distribution of the blade element chords used by the aerodynamics calculations as in Fig. 5.6, the notch in the planform in Fig. 5.6a is not evident in the blade chord plot in Fig. 5.6b.

5.1.3 Hover Kinematics - No Inflow

Kinematics matching those used by Stanford et al.[27] were used for the hovering configuration. For the reference frame and nomenclature used in this work the Euler angles vary through time as

$$\kappa = \frac{\pi}{3}\cos(\omega t) \tag{5.4}$$

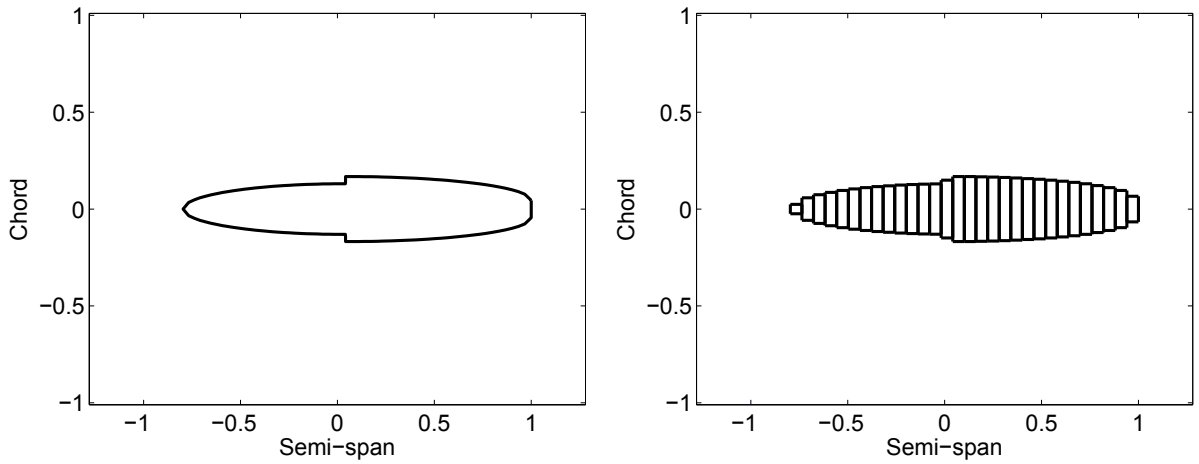

(a) Optimal modified Zimmerman planform

(b) Optimal planform created by discretizing modified Zimmerman planform

Figure 5.6: Comparison between the final planform as determined by the modified Zimmerman method and the blade element discretization.

$$\tau = -\frac{\pi}{4}\sin(\omega t) + \frac{\pi}{2} \tag{5.5}$$

$$\gamma = 0 \tag{5.6}$$

The optimization for the hover kinematics was slightly different from the flapping optimization in that the hover planform was optimized to produce the maximum average lift, rather than the maximum average thrust, which would always average to be zero for symmetric kinematics. Optimizations were performed on the hovering configuration similarly to the flapping configurations, where average lift was the objective function and peak power and area were constrained. The Pareto front, shown in Fig. 5.7 was again found by slowly relaxing the constraints on peak power and area. Shapes similar to those obtained in the flapping kinematics optimization were obtained. When the power constraint was inactive, the blade elements moved toward the wing tip, with the chord maximized.

The optimizer saves power by allocating wing area closer to the hinge rather than pushing all of the area as far away as possible. Fig. 5.8 shows the set of optimized symmetric shapes

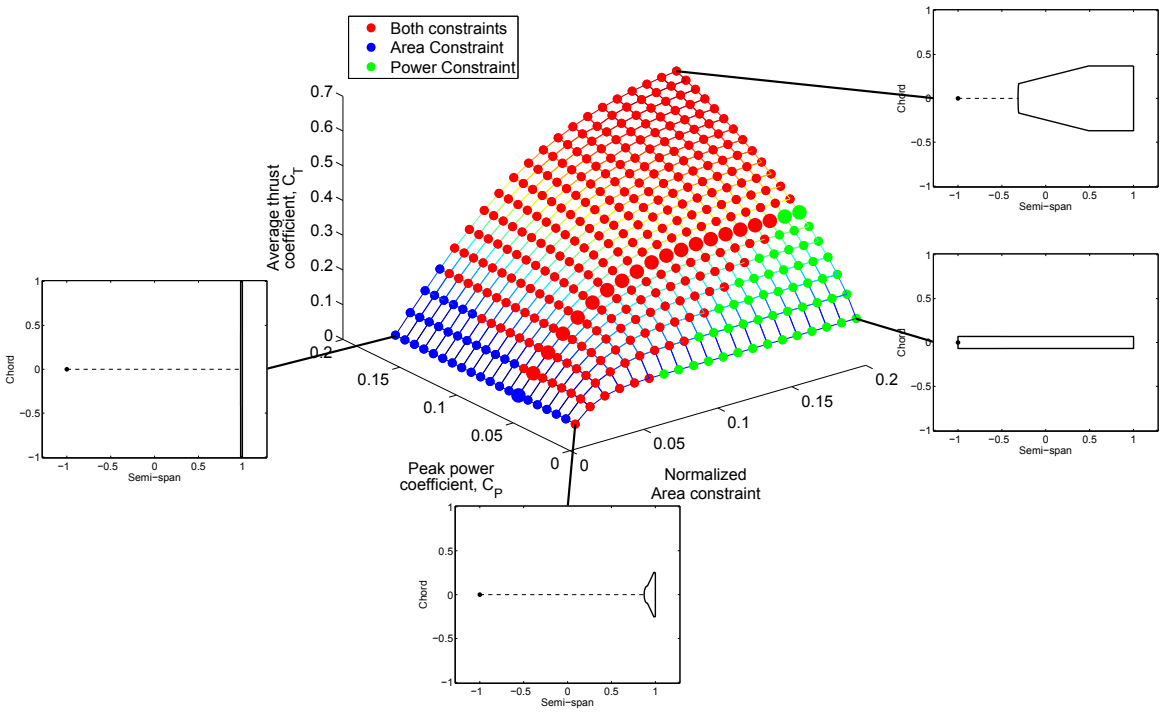

Figure 5.7: Pareto front for optimal symmetric designs

for hover as the power constraint was held constant at $C_p = 0.0584$ and the area constraint was relaxed.

5.1.4 Hover Kinematics - Inflow

The assumed inflow model based on lifting-line theory was implemented with the hovering kinematics. The Pareto surface is shown in Fig. 5.9. If a cut of the Pareto surface was made at $C_P = 0.0417$ to illustrate how the optimal planform changes as the area constraint is relaxed. As the area constraint is relaxed and the peak power constraint becomes active, the optimizer shifts the wing area toward the hinge. The optimal planform tends to mimic the planform trends for flapping kinematics. When only the area constraint is active, the optimal planform resembles a teardrop shape. When the power constraint becomes active, planform area is allocated to a location that is closer to the hinge. When the area constraint is larger, the optimal shape is triangular with both a rounded tip and a rounded root. When only the peak power constraint is active, the optimal shape is a triangle conjoined to a half-ellipse.

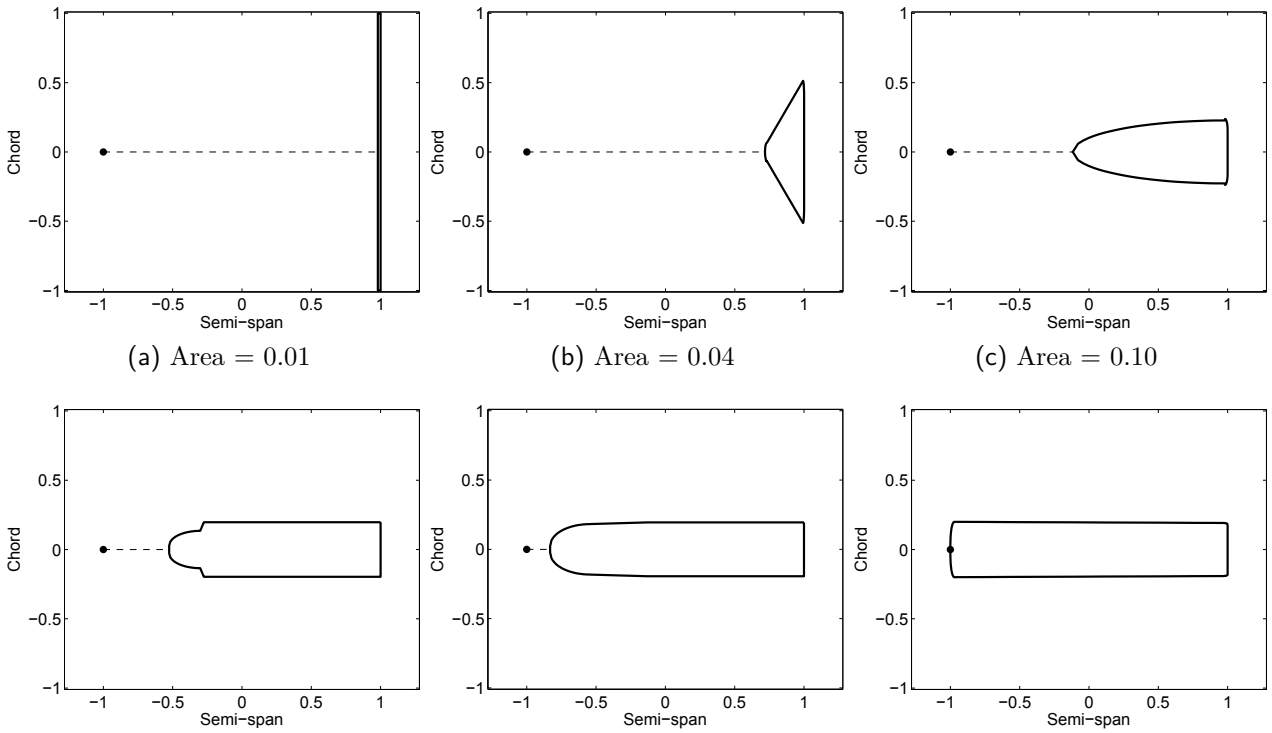

(a) Area = 0.01 (b) Area = 0.04 (c) Area = 0.10

(d) Area = 0.14 (e) Area = 0.17 (f) Area = 0.20

Figure 5.8: Optimal hover symmetric wing designs for different area constraints and with no assumed inflow

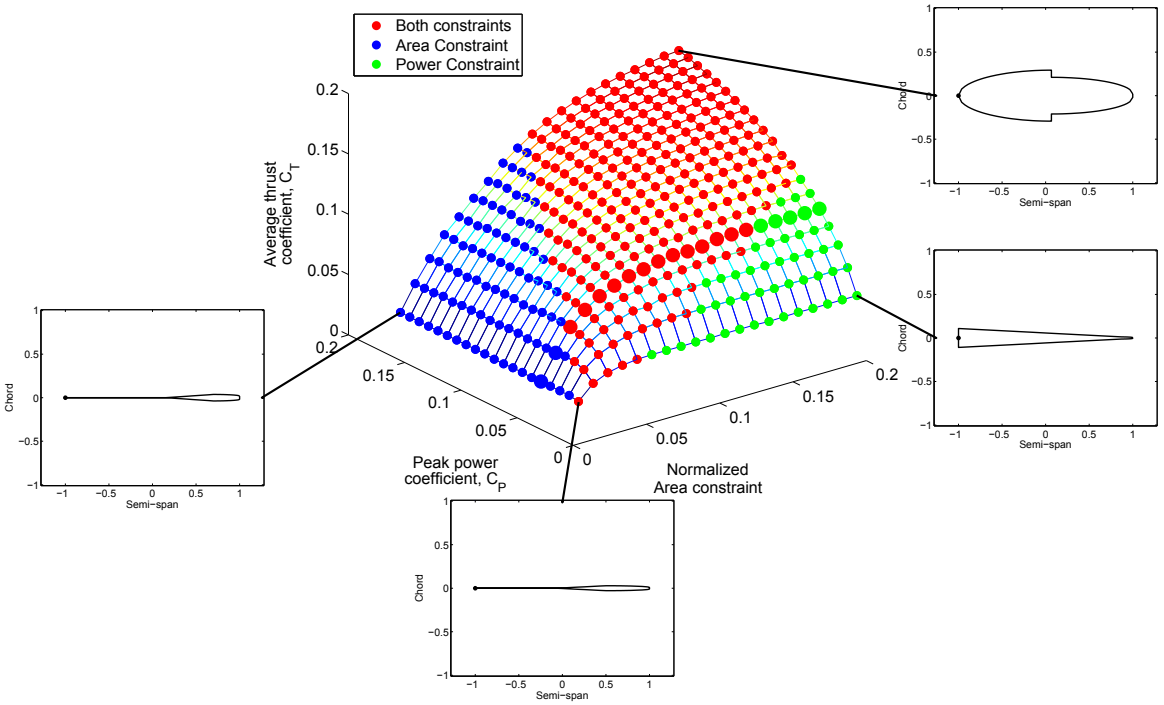

Figure 5.9: Pareto front of designs for hovering, symmetric wings, with 3D inflow effects

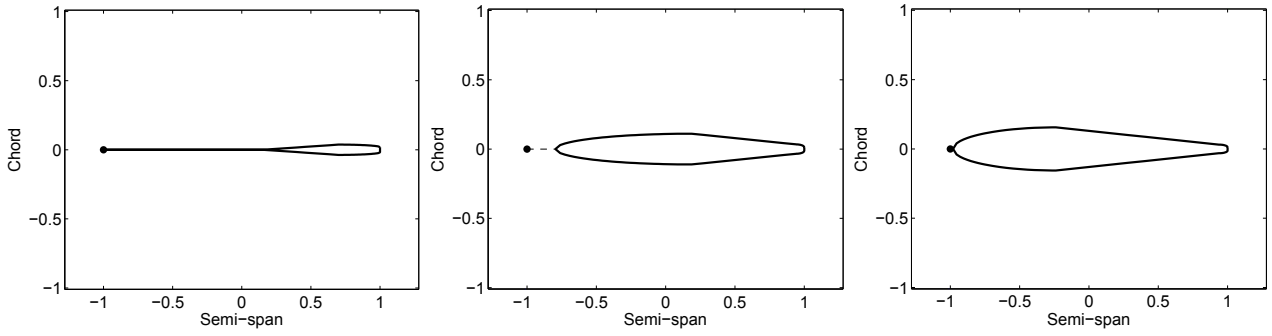

(a) Area = 0.01 (b) Area = 0.07 (c) Area = 0.10

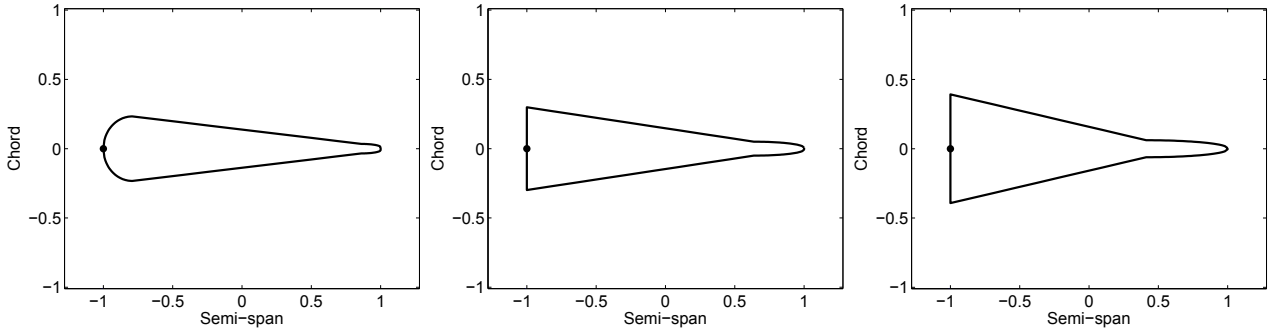

(d) Area = 0.13 (e) Area = 0.15 (f) Area = 0.20

Figure 5.10: Optimal, symmetric hovering wing designs for different area constraints at a constant power constraint of $C_p = 0.0417$ and with 3D inflow

The Pareto optimal planforms for hover are similar to the optimal planforms for the flapping kinematics. The teardrop shape still performs best when only the area constraint is active, and a triangular planform is best when only the power constraint is active. However, there is a difference between the flapping and hovering planforms when only the power constraint is active. In the case of the hover kinematics planform, shown in Fig. 5.10f, the optimizer allocates more area near the wing root than in the flapping case. This is because the objective function for this problem is lift, not thrust as in the previous case. The lift is proportional to both v_0 and v_1, as seen in Eqs. 3.15-3.17, whereas the thrust is proportional only to v_0 as seen in Eq. 3.18. The rotation of the wing will generate the same amount of lift whether the extra area is at the root or the tip of the wing. But if the area is located at the tip of the wing, then the stroke of the wing will cause the power to increase beyond the allowed power. By allocating the area more toward the root, more lift is created without violating the power constraint.

5.2 Power-Thrust Optimal Wings Explanation

In certain regions of the Pareto surface, only the power constraint is active and the optimizer tends to move most of the wing mass toward the root and have a small chord at the wing tip. However, if a different parameterization technique is used, then the power-thrust Pareto-optimal shapes can be better explained. Instead of using the parameters from the modified Zimmerman method, the chord lengths of the blade elements used in the aerodynamic calculations are used as the design variables along with the width of the blade elements. The optimization problem is reformulated without the area objective function so now only the power and thrust are used in the multi-objective formulation.

Using the blade element chords, the optimizer creates Pareto-optimal designs which are seen in Figure 5.11. The optimizer creates wings that drastically increase in chord close to the wing hinge with small chord close to the wing tip. The gaps at the wing root and the wing tip are due to the parameterization. The chord of each blade element is determined at

the center of the element, which leaves a gap at the root and hinge where the center of the blade element does not connect to another point.

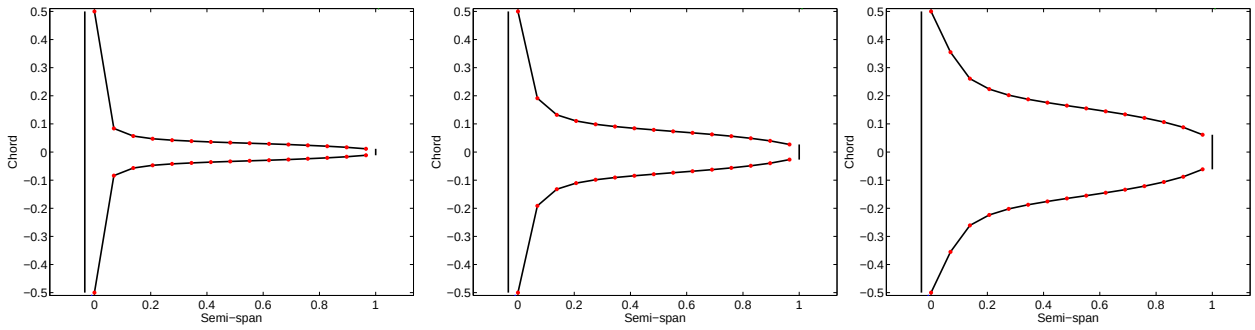

Figure 5.11: Thrust-optimal flapping wing planforms as power is relaxed for rigid wings

These optimal planforms are optimal since they minimize the induced downwash during the flapping cycle. From lifting-line theory, it is known that an elliptical lift distribution produces the minimum induced drag, and one way to give an elliptical lift distribution is to create an elliptical planform. However, in an analogous situation, flapping wings can best be modeled in the steady state flight as wing with a linearly varying angle of attack. The linearly varying angle of attack means that the optimal lift distribution (and, conversely the optimal planform) is no longer elliptical. The approximate optimal chord distribution to minimize the induced drag for a flapping wing is calculated from lifting-line theory by adding a linear angle of attack. The optimal chord distribution for a wing with a linear angle of attack is shown in Figure 5.12 and is compared against a sample planform from Figure 5.11 as well as an elliptical chord distribution. The linear angle of attack wing tends to create planforms which maximize the chord near the wing root while decreasing the chord at the tip to zero. The optimizer similarly creates wings which increase the chord near the wing root. The difference between the theory and the optimal results is due to the upper bound on the chord. The optimizer increases the chord at the root to the upper bound and then fills in the wing area to minimize the induced velocity.

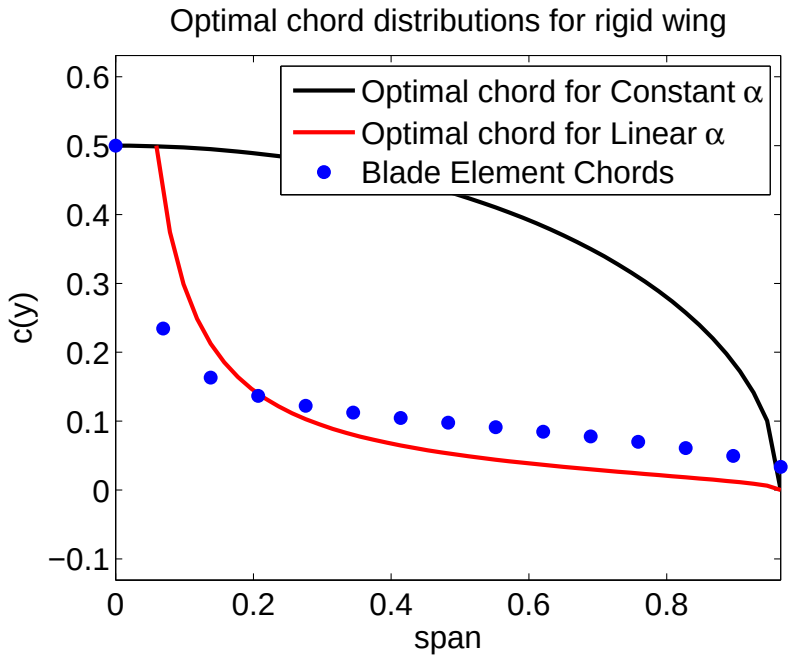

Figure 5.12: Pareto optimal planform (blue dots) compared against the optimal chord distribution to minimize induced drag (red line)

Chapter 6

Shape and Structural Wing Optimization

6.1 Problem Formulation

The analysis and optimization of flapping wings needs to include wing deformation over the flapping cycle to more closely model the physics of flapping wings. In this chapter, the flapping wings are modeled with Discrete Kirchhoff Triangular plate finite elements that will allow for wing deformation in the spanwise and chordwise directions.

The design variables in the optimization problem are the modified Zimmerman parameters for the shape as well as the wing thickness distribution which determines the effective stiffness and mass distributions. The modified Zimmerman parameterization is constrained to give planforms that are symmetric about the midchord. The planform constraints are in place so that the current optimization results can be compared against results in previous chapters. The thickness distribution is prescribed as a polynomial with the coefficients acting as design variables

$$t(\xi, \eta) = t_0 + t_1\xi + t_2\eta + t_3\xi^2 + t_4\eta^2 + t_5\xi\eta \tag{6.1}$$

where ξ and η are the non-dimensional coordinates in the span and chord.

The wing material used for this problem has an elastic modulus of $E = 2.3\,GPa$ and $\rho_w = 1040\,kg/m^3$ which are approximately the material properties of a plastic used in a 3D printer. The maximum span and chord allowable are both set to 10 cm so that the designs are within the DARPA definition of a MAV. The wing is flapped as

$$\gamma = \frac{\pi}{9}\cos\left(5\pi t\right) \tag{6.2}$$

in a constant freestream velocity of $1\,m/s$. If one-half of the maximum chord is considered to be the reference length, then the reduced frequency of $k = \frac{\omega c}{2V_\infty}$ is approximately 0.4.

The objective functions for the optimization are the average thrust coefficient over the flapping cycle and the peak power coefficient. Again utilizing the ϵ-constraint method, the power objective function is treated as a nonlinear constraint. A stress constraint is added to ensure that the wing does not undergo plastic deformation. The upper and lower bounds on the thickness are $1cm$ and $0.1mm$, respectively. The optimization problem is written as

$$\begin{gathered} min:\ -C_{T_{avg}} \\ st:\ C_P \leq \epsilon \\ \sigma < \sigma_{all} \\ t_{lb} \leq t\left(\bar{x}, \bar{y}\right) \leq t_{ub} \\ Geometric\,Constraints \end{gathered} \tag{6.3}$$

6.2 Optimization Results

The Pareto front is shown in Figure 6.1. The thrust increases nearly linearly with respect to the power constraint, a trend which is consistent with the results in Section 5.2. The optimizer tends to converge to high-aspect ratio wings in an effort to minimize the induced drag effect on the wing. The Pareto-optimal wing designs are shown in Figure 6.2. Each subfigure shows the top view of the optimal planform as well as a mesh plot that represents the thickness distribution of the wing. With the exception of the last two wings, the optimizer

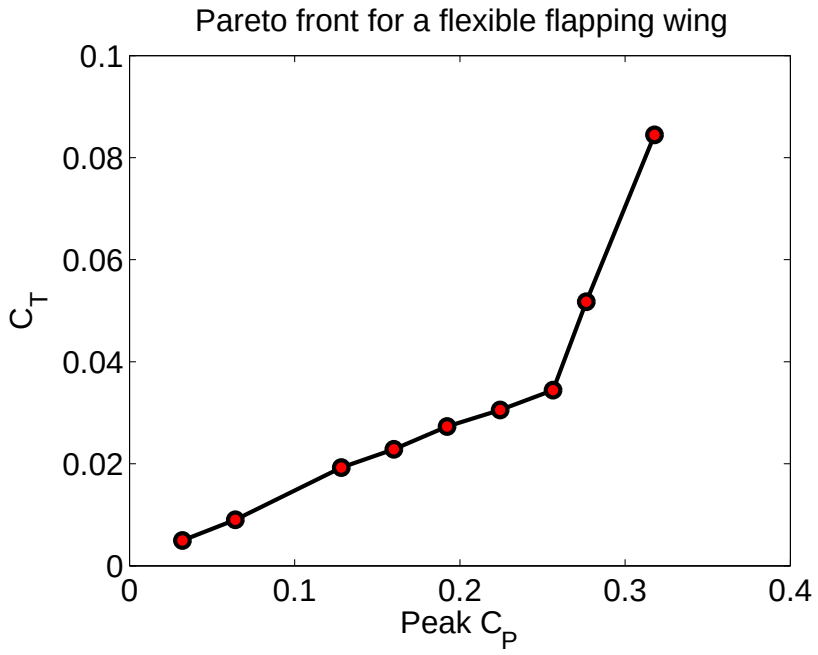

Figure 6.1: Pareto front of aeroelastic plate-like wings with quadratic thickness distribution

also tends to increase the wing thickness to prevent any deformation during the flapping cycle. This trend of increased thickness, and thus increased stiffness is seen in the first six planforms in Figure 6.2. This is because the optimizer is making the wings effectively rigid by increasing the thickness of each design, thus limiting the amount of input power that is needed to overcome the deformation during the flapping cycle.

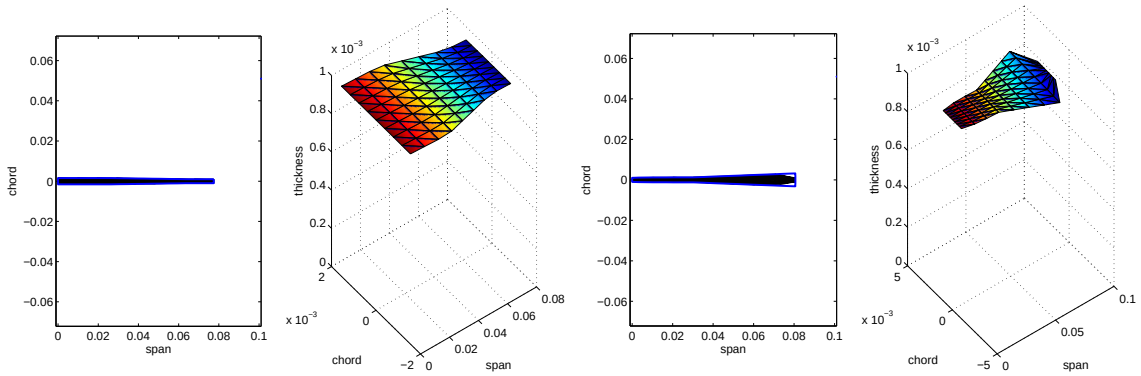

(a) $C_{Ppeak} = 0.032$

(b) $C_{Ppeak} = 0.064$

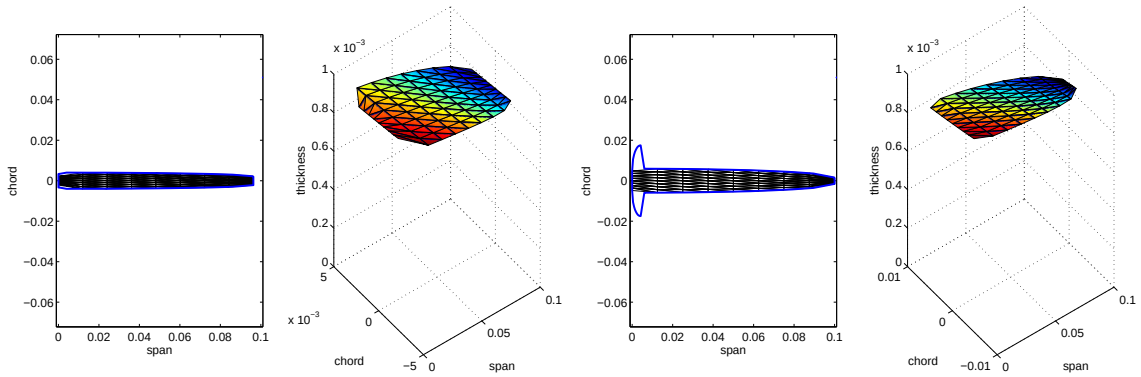

(c) $C_{Ppeak} = 0.16$

(d) $C_{Ppeak} = 0.19$

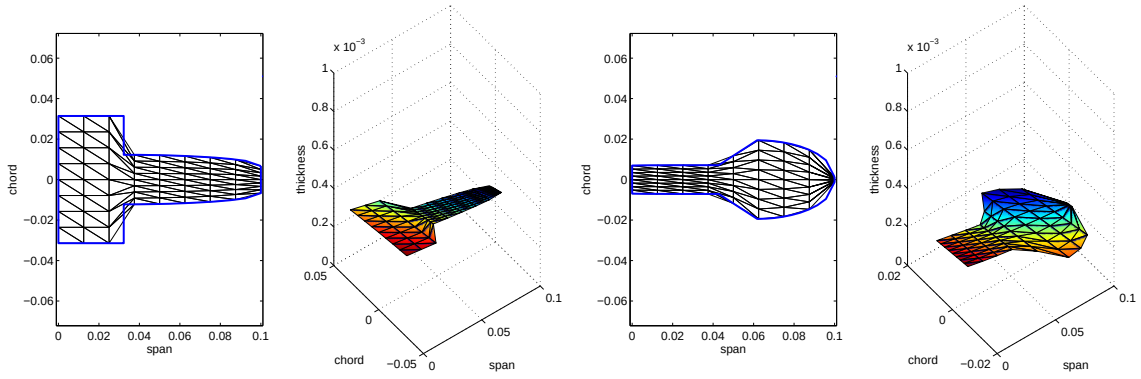

(e) $C_{Ppeak} = 0.28$

(f) $C_{Ppeak} = 0.32$

Figure 6.2: Thrust-optimal designs for flexible wings

For the wings with higher allowable power, such as the design in Figure 6.2f, the power required to overcome the wing bending is in phase with the power required for the rigid-

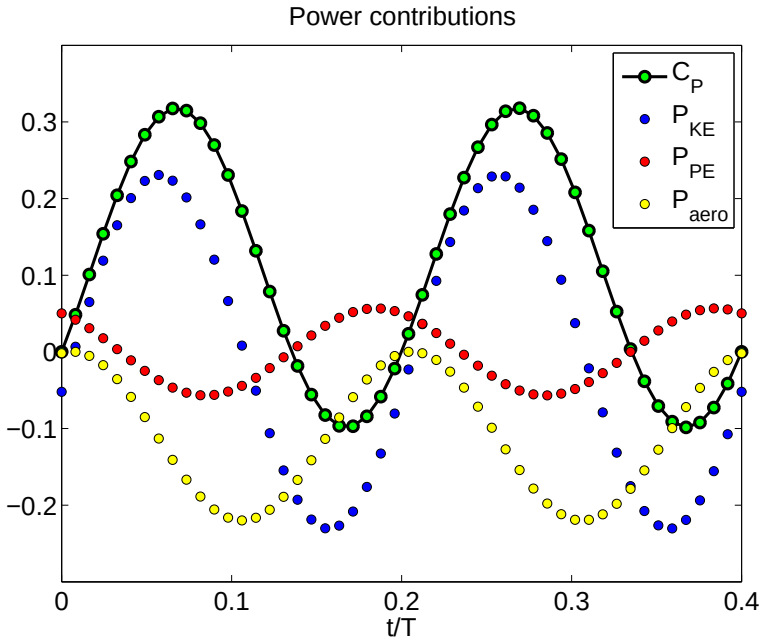

Figure 6.3: Breakdown of the contributions to power from the different components

body motion. For the other designs, little or no deformation occurs. So, a mechanism that potentially benefits thrust production is suppressed by the optimizer in an effort to save power. It is not until the power requirement is relaxed that the bending can be utilized for thrust production.

Figure 6.3 shows the components of the input power along with the total power over one flapping cycle. The components are broken down to show aerodynamic power (yellow), time-derivative of the kinetic energy (blue), and time-derivative of the potential energy (red). While slightly out-of-phase due to the aerodynamic damping, the time-derivative of the potential energy negates some of the power contribution from the kinetic energy.

More insight can be gained from the power by grouping its components in an alternate way. Instead of grouping the components of power as

$$P = \frac{dP_E}{dt} + \frac{dK_E}{dt} - P_{aero} = \left(\{\dot{q}\}^T [K_s] \{q\}\right) + \left(\left\{\ddot{h}\right\}^T [M_s] \left\{\dot{h}\right\} + \left\{\dot{h}\right\}^T [M_s] \{\ddot{q}\} + \left\{\ddot{h}\right\}^T [M_s] \{\dot{q}\} + \{\ddot{q}\}^T [M_s] \{\dot{q}\}\right) - P_{aero} \quad (6.4)$$

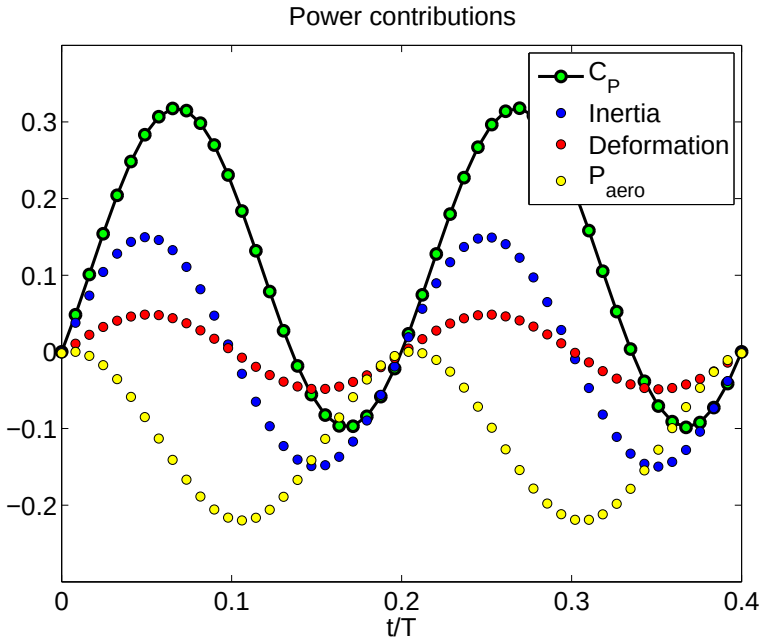

Figure 6.4: Breakdown of the contributions to power from the different components

they are grouped such that all terms containing the deformation or its time-derivative are together. The groups within the total power are the aerodynamic power, the power to overcome the rigid-body inertia, and the power required to overcome the deformation (from both kinetic and potential energy components).

$$P = \left(\{\dot{q}\}^T [K_s] \{q\} + \{\dot{h}\}^T [M_s] \{\ddot{q}\} + \{\ddot{h}\}^T [M_s] \{\dot{q}\} + \{\ddot{q}\}^T [M_s] \{\dot{q}\}\right) + \left(\{\ddot{h}\}^T [M_s] \{\dot{h}\}\right) - P_{aero} \quad (6.5)$$

The alternate power breakdown is shown in Figure 6.4. It is seen that the deformation that occurs over the flapping cycle actually adds to the peak input power requirement by being in phase with the inertial power. The optimizer sees little or no power savings by creating a wing with deformation. This is why many of the wings in the Pareto surface are very thick and stiff rather than deformable. Even though the thrust gets a boost proportional to the added wing velocity from the deformation component, the power sees a similar boost.

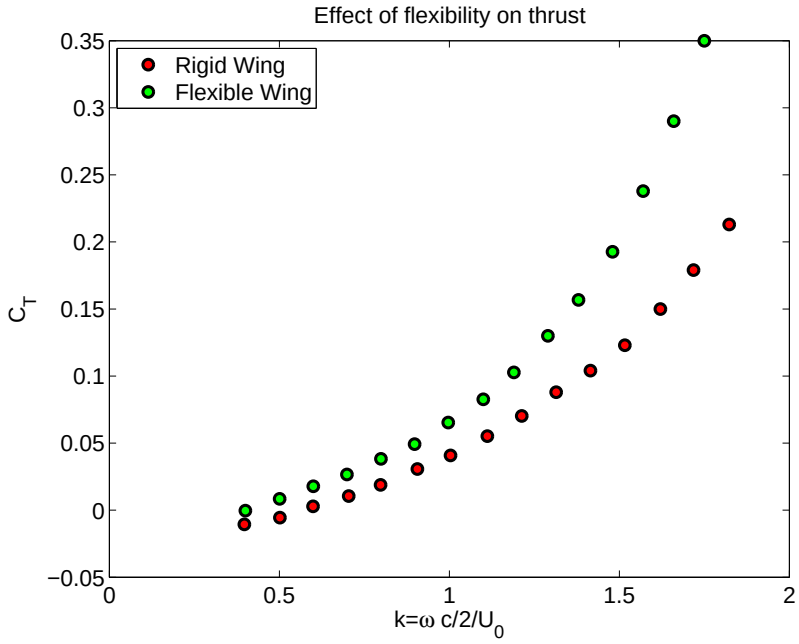

Figure 6.5: Data from Heathcote[1] for the coefficient of thrust for a rigid wing and for a flexible wing

This trend is also seen in the data presented by Heathcote, et al.[1] In that paper, they provide experimental work that shows that both power and thrust increases as the wind deformation increases. The coefficient of thrust increases 45-60% over the rigid case as shown in Figure 6.5 while the coefficient of power increases 30-50% over the rigid wing as seen in Figure 6.6.

6.3 Mass Effect

The effect of the wing density on the optimal wing design is explored. First the wing density is increased by an order of magnitude and the optimal Pareto front of designs is calculated. The wing density is then decreased by an order of magnitude and the Pareto-optimal designs are found. No other parameters are changed relative to the previous problem formulation.

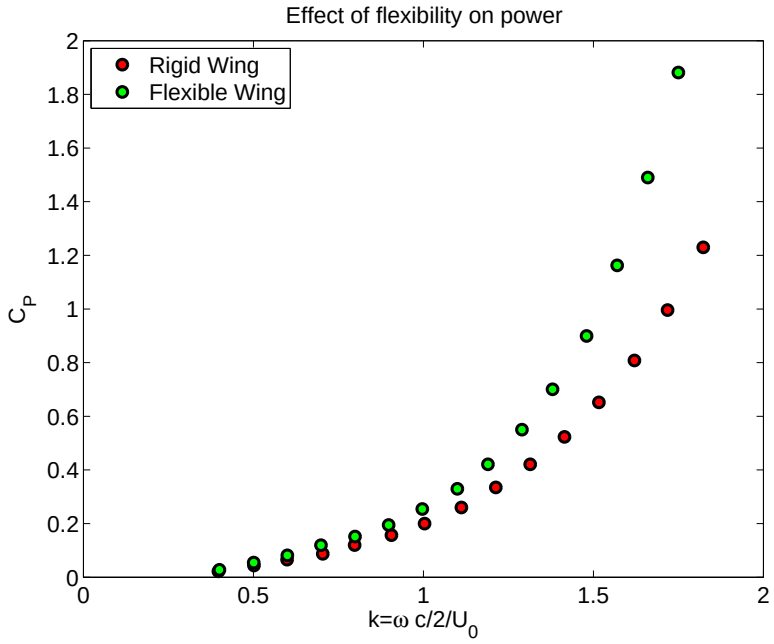

Figure 6.6: Data from Heathcote[1] for the coefficient of power for a rigid wing and for a flexible wing

6.3.1 Increased Wing Density

On this Pareto front, the optimizer tends to create wings with most of the wing area allocated toward the wing root and only a little of the wing mass at the tip. This is consistent with the theoretical prediction of the optimal, rigid, flapping wing. However, the optimal wings with increased density are not rigid, as will be shown below, and are not attempting to minimize the induced drag like the rigid wings.

The only noticeable difference between the wings on the Pareto front is the increase in wing area near the wing root. The optimizer increases the wing area to prevent yielding in the wing material. The wing continues to increase in size until $C_{P,peak} \approx 0.4$, which is where the optimizer reaches a minimum within the design space. This is seen in the Pareto front in Figure 6.7 where only ten points appear to be plotted, but the right-most point represents ten different design problems which collapse to the same design.

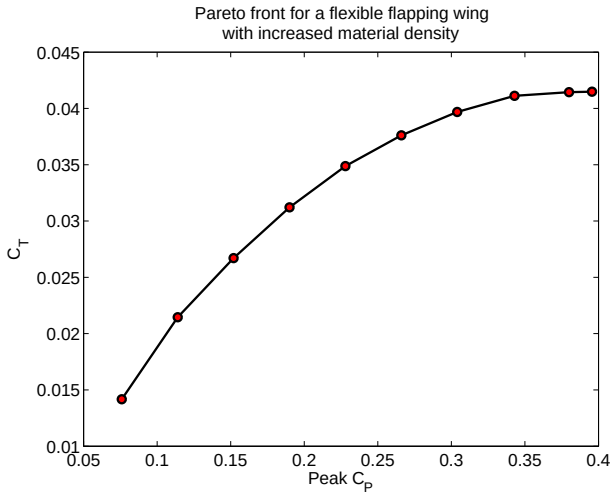

Figure 6.7: Pareto front for flexible wings with an increase in density

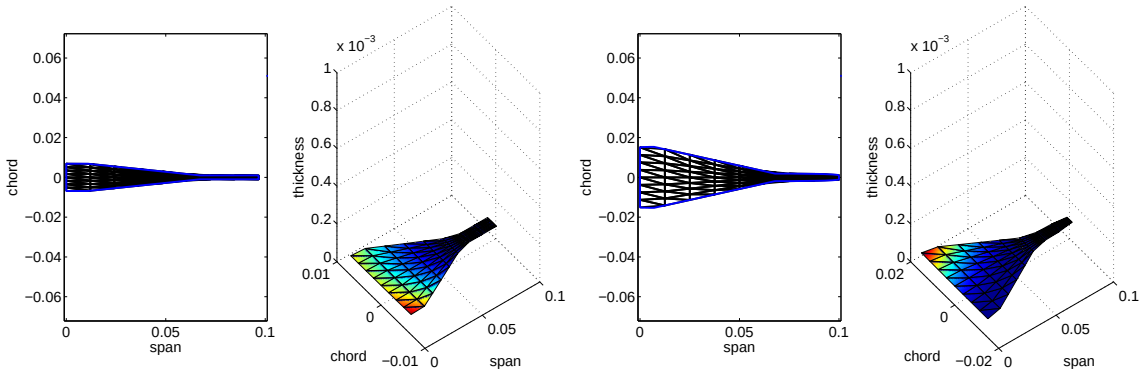

(a) $C_{Ppeak} = 0.076$ (b) $C_{Ppeak} = 0.152$

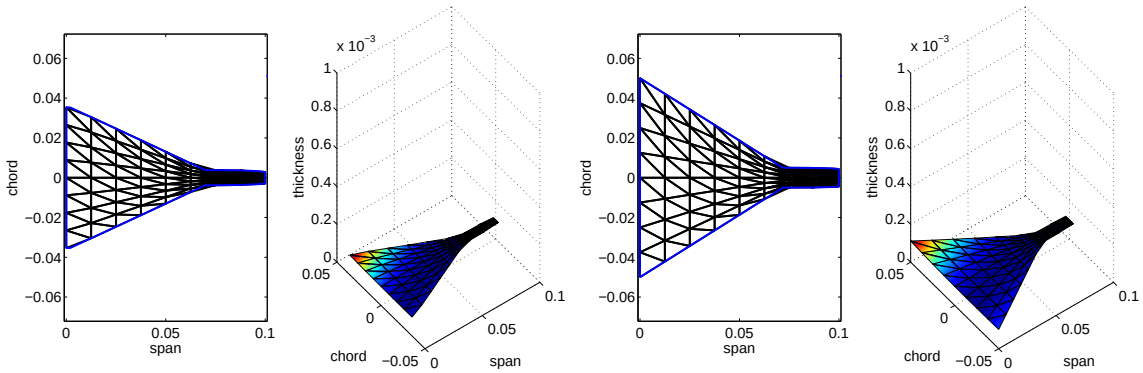

(c) $C_{Ppeak} = 0.305$ (d) $C_{Ppeak} = 0.396$

Figure 6.8: Thrust-optimal designs for flexible wings with increased material density

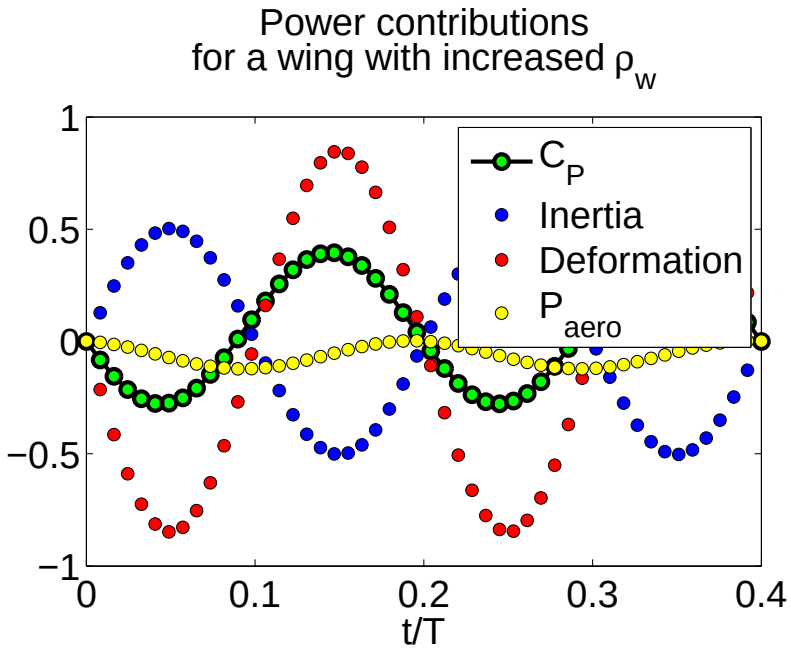

Figure 6.9: Power breakdown for a Pareto-optimal wing with increased material density

The wings with increased density are not rigid, even though they resemble the optimal rigid planforms in Section 5.2. As can be seen by the alternate power breakdown in Figure 6.9, there is a large amount of deformation in the wing with increased density. However, the deformation is now out-of-phase with the rigid-body motion, so the input power needed for the two components cancel out. Typically, the large phase lag of the deformation relative to the rigid-body motion hinders the production of the thrust, as is shown in Section 4.2.4. However, the deformation is very large in this particular problem so the thrust is improved. This occurs even though the velocities from the deformation and rigid-body motion are acting in opposite directions throughout the flapping cycle.

It is also seen in the power breakdown the relatively small effect the aerodynamic power has on the overall power calculation for the wing with increased density. In the alternate power breakdown show in Figure 6.4, the wing with nominal density has aerodynamic and inertial power values that are close in magnitude. The optimizer creates wings that take advantage of the small aerodynamic power and increases the deformation – and power due to the deformation – to increase the thrust.

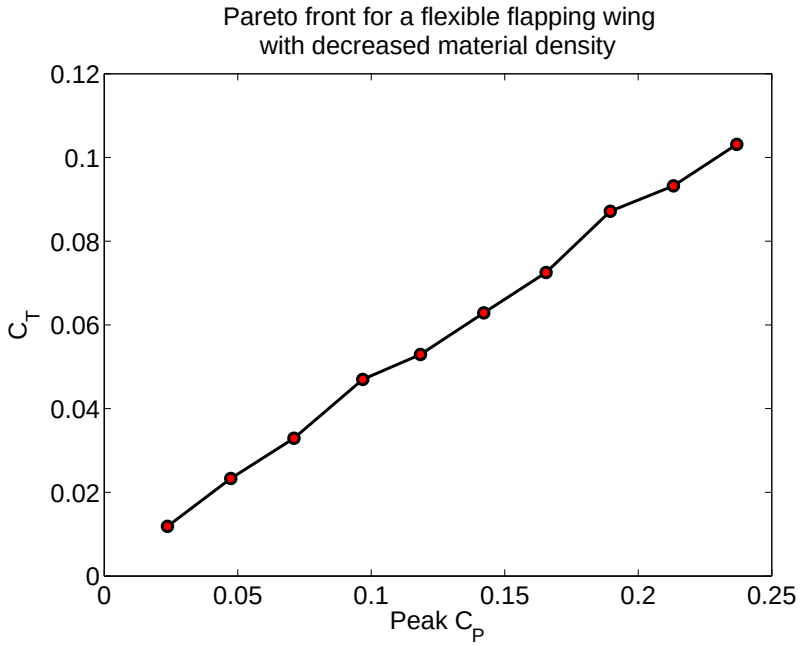

Figure 6.10: Pareto front for flexible wings with an decrease in material density

6.3.2 Decreased Wing Density

The density of the wing material is now decreased by an order of magnitude with respect to the designs presented in Section 6.2 and two orders of magnitude with respect to the designs in the previous section. The Pareto front of designs for the decreased density wings is shown in Figure 6.10. As is the case with the previous design formulations, the thrust and peak power are nearly linear.

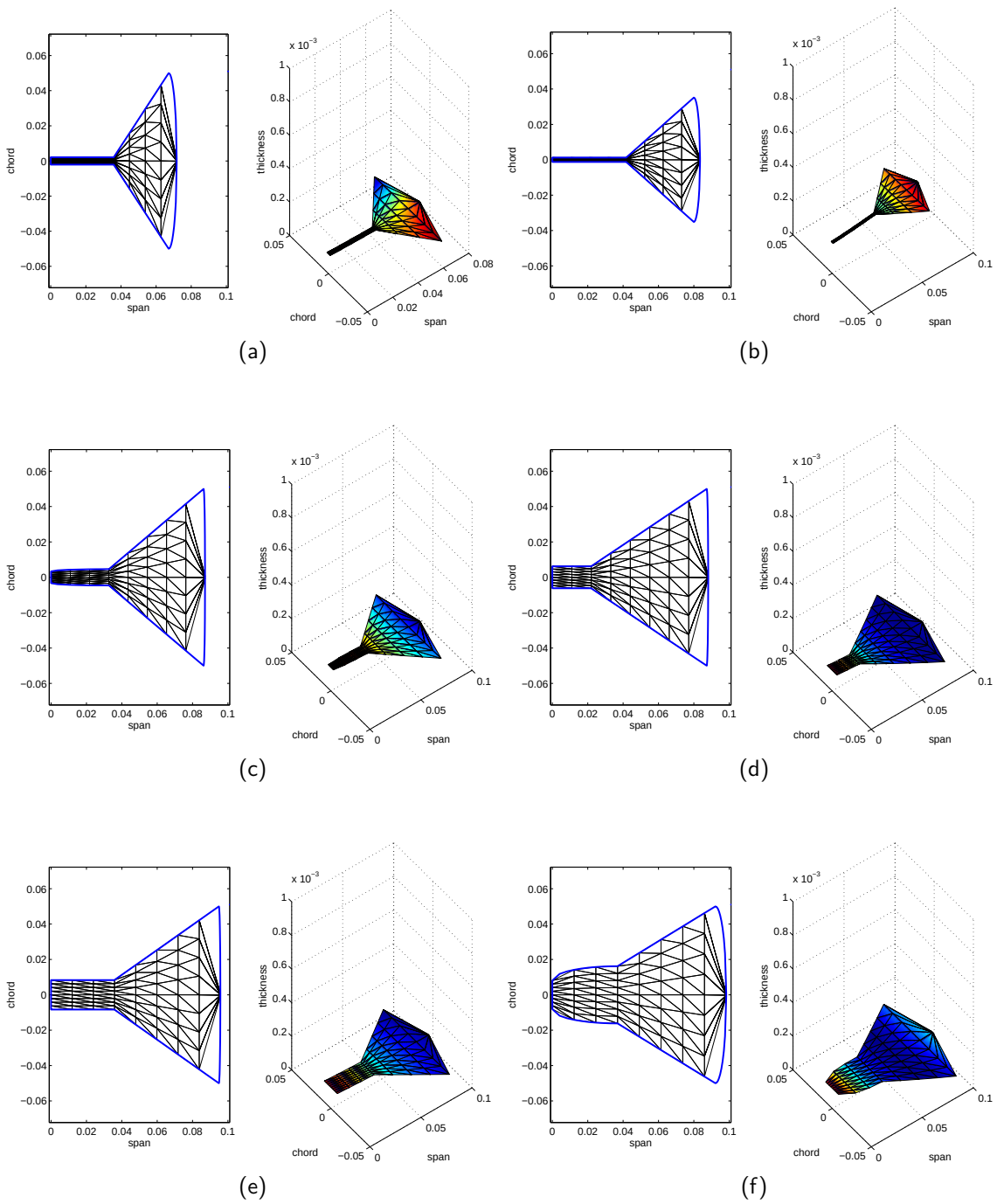

Figure 6.11: Thrust-optimal designs for flexible wings with decreased material density

It is seen that the the optimizer tends to create wings with much of the wing area toward the tip of the wing rather than at the root as was done with the wings with increased material

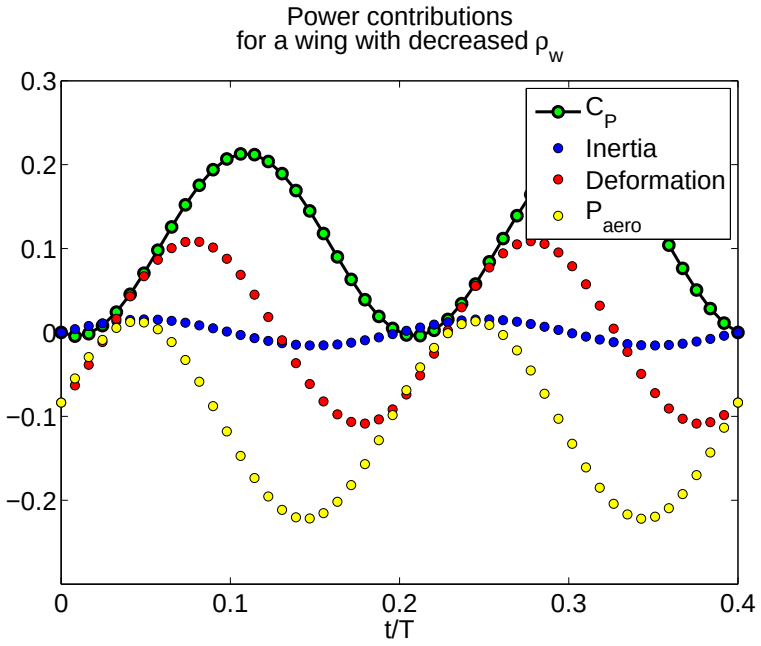

Figure 6.12: Power breakdown for a Pareto-optimal wing with decreased material density

density. This occurs because the lighter wings need very little power to prescribe the rigid body motion. So the only two components of power with any significance are the deformation power and the aerodynamic power. The optimizer improves the thrust by allocating mass toward the tip which, in turn, increases the wing deformation. The associated increase in inertial power is small and is essentially neglected by the optimizer. The small amount of power needed to create the rigid-body motion relative to the power needed to allow for the deformation is seen in Figure 6.12.

6.4 Thrust-Mass Optimization

A wing mass constraint is used in lieu of the power constraint in an effort to isolate the thrust improvement with deformation without the power constraint. In isolating the thrust from the power, the effects of deformation on the optimal thrust design are seen. The optimizer tends to create wings which maximize the span of the wing and then increases the chord until the area constraint is met. The thrust-weight Pareto front is shown in Figure 6.13 with

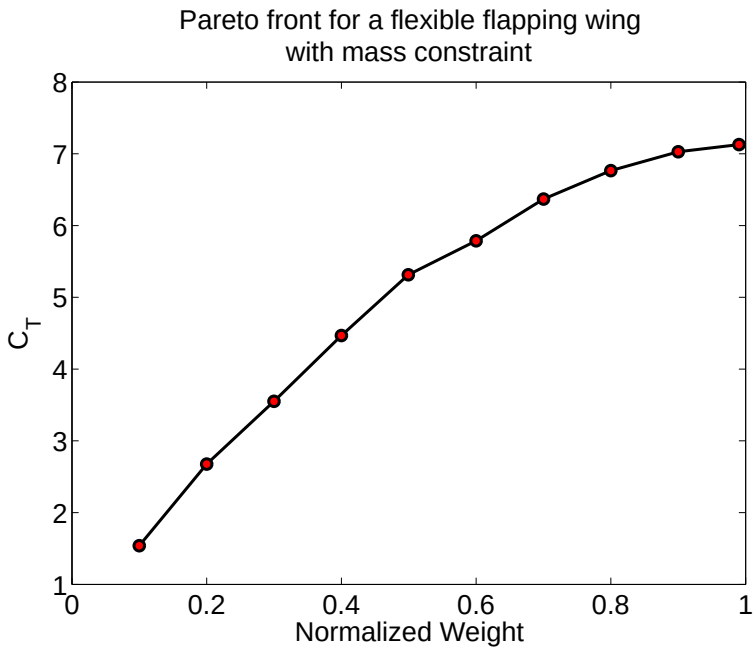

Figure 6.13: Pareto front for the thrust-mass multiobjective optimization

several examples of Pareto-optimal designs shown in Figure 6.14.

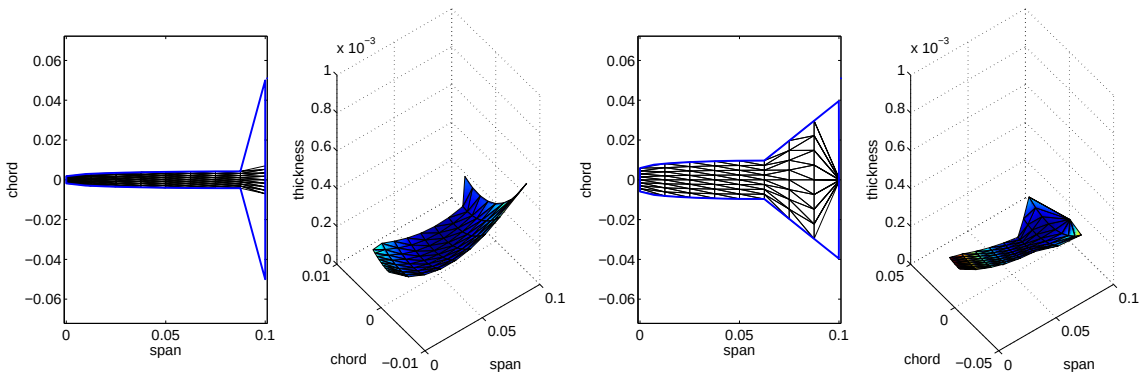

(a) $W = 0.1W_0$ (b) $W = 0.3W_0$

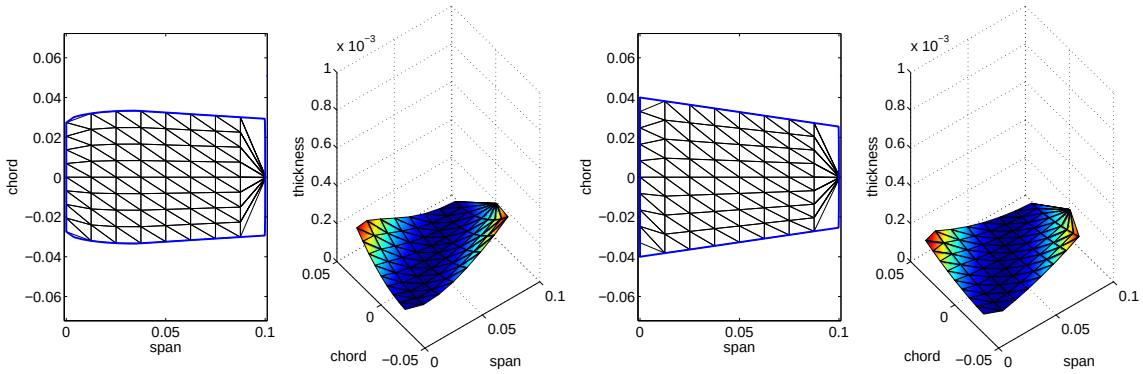

(c) $W = 0.5W_0$ (d) $W = 0.6W_0$

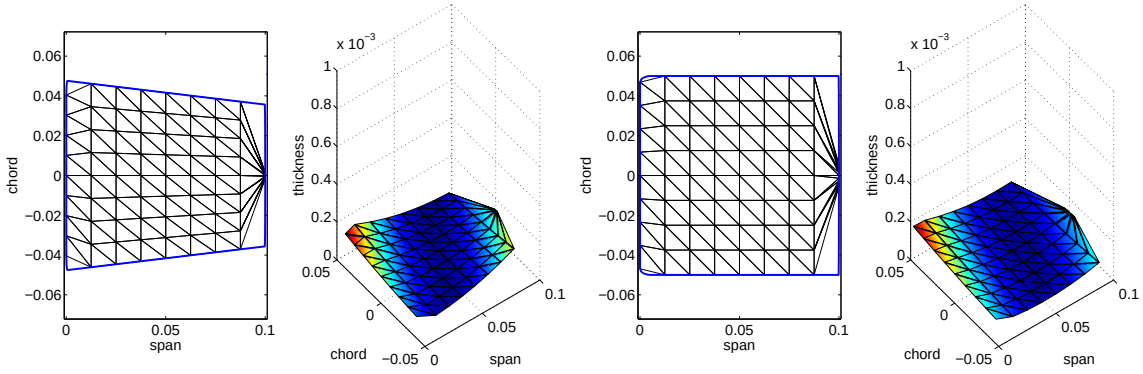

(e) $W = 0.8W_0$ (f) $W = 1W_0$

Figure 6.14: Thrust-mass Pareto optimal designs for flexible wings

The most obvious difference between the optimized wings with the power constraint and the optimized wings with the weight constraint is that the optimizer tends to allocate more

mass toward the wing tip, thereby increasing the deformation and thrust during the flapping cycle. A comparison of a power-optimal wing is compared to an area-optimal wing in Figure 6.15.

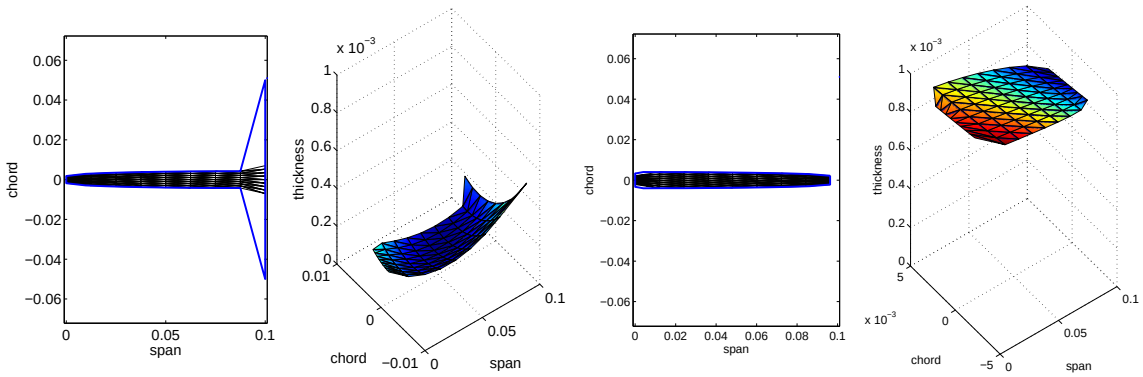

(a) Thrust-mass optimal wing with C_{Ppeak} = 0.163

(b) Thrust-power optimal wing with C_{Ppeak} = 0.16

Figure 6.15: Comparison of a thrust-power optimal wing with a thrust-mass optimal wing

The two optimal planforms have similar peak input power values and similar planforms but the thickness distributions are very different. The power-optimal wings tend to evenly distribute the wing thickness so as to not increase deformation by adding mass at the wing tip. Also, the even distribution of the thickness, with the large values of the thickness at the tip, create wings that are stiff and effectively inflexible, as is shown by the power breakdown plot in Figure 6.16b. The power breakdown is for the wing shown in Figure 6.15b. The power breakdown plot for the mass-optimal wing shown in Figure 6.16a. The mass-optimal wing clearly has more deformation over the flapping cycle than the power-optimal wing.

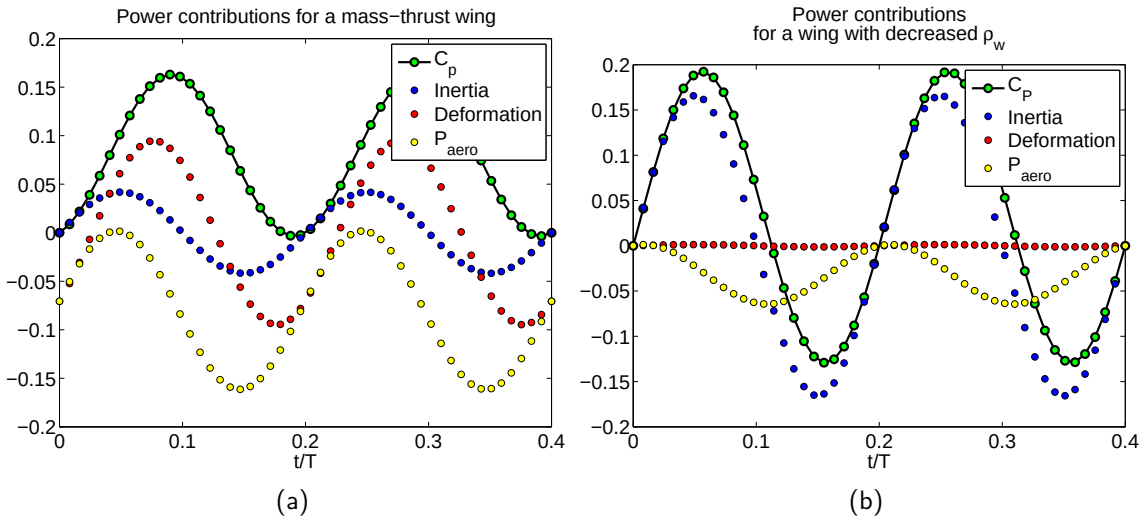

Figure 6.16: Comparison of a power breakdowns for the thrust-mass and thrust-power optimal wings

6.5 Thrust Improvement by Deformation

The optimal results for the wing of nominal material density are effectively rigid until the power constraint is large enough to allow for wing deformation to benefit the thrust production. As a check to see if the flexibility properly benefits the thrust production, the Pareto-optimal planforms from Section 6.2 are given a very high modulus of elasticity so that the wings have infinitesimal deformation over the flapping cycle. The optimal results and their rigid counterparts, seen in Figure 6.17, produce very similar coefficients of thrust and power until the allowable power reaches $C_p = 0.8$. The final two design points stand out among the rest as those are the two that have the most deformation. The final two design points are where the power constraint is large enough to allow for deformation. At these design points the benefits of flexibility are most obvious. The flexible wings out-perform their rigid counterparts in the thrust while needing more power.

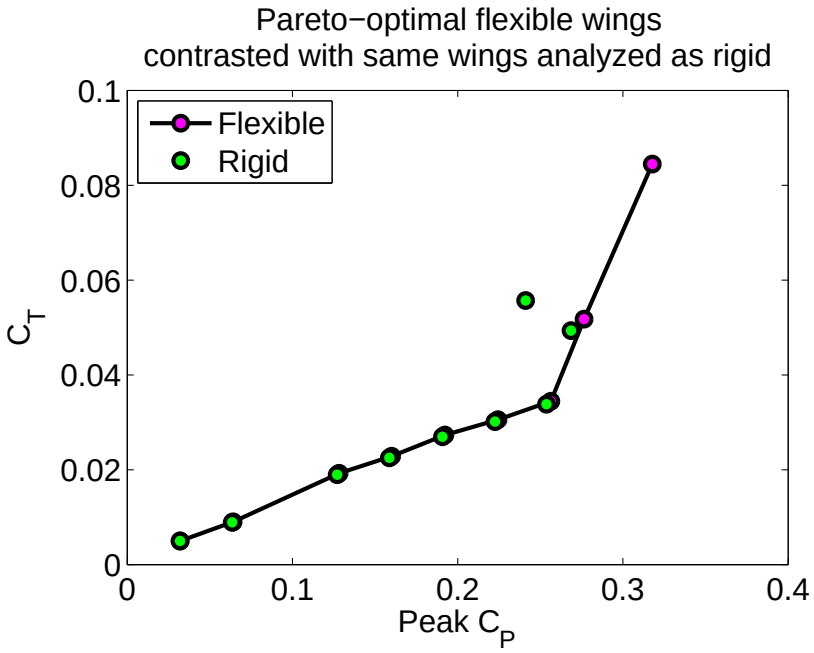

Figure 6.17: Comparison of aerodynamic performance if the planforms are considered rigid and flexible

Chapter 7

Membrane Wing Shape and Prestress Optimization

In this chapter, prestress optimization is performed on a flapping wing. First optimization is preformed on a rectangular flapping wing where the spanwise and chordwise prestress values are independently prescribed as polynomials. The planform and prestress are then optimized simultaneously with the prestress applied as described in Section 3.2.2.

7.1 Prestress Optimization

The thrust produced by a flapping membrane wing is optimized by utilizing the spacial distribution of the forces applied to the membrane as the design variables. A wing of aspect ratio two is flapped in a freestream with a reduced frequency of $k = 0.3$. The applied preforces F_x and F_y are independently prescribed as polynomials with the polynomial coefficients acting as the design variables in the optimization. The preforce leads to a prestress distribution as was described in section 3.2.2. A visual representation of a general prestress distribution is shown in Figure 7.1 along with the boundary conditions used

Two stress constraints are added: one to make sure the yield stress is not reached for the membrane material and a second one to ensure that the pretension throughout the membrane

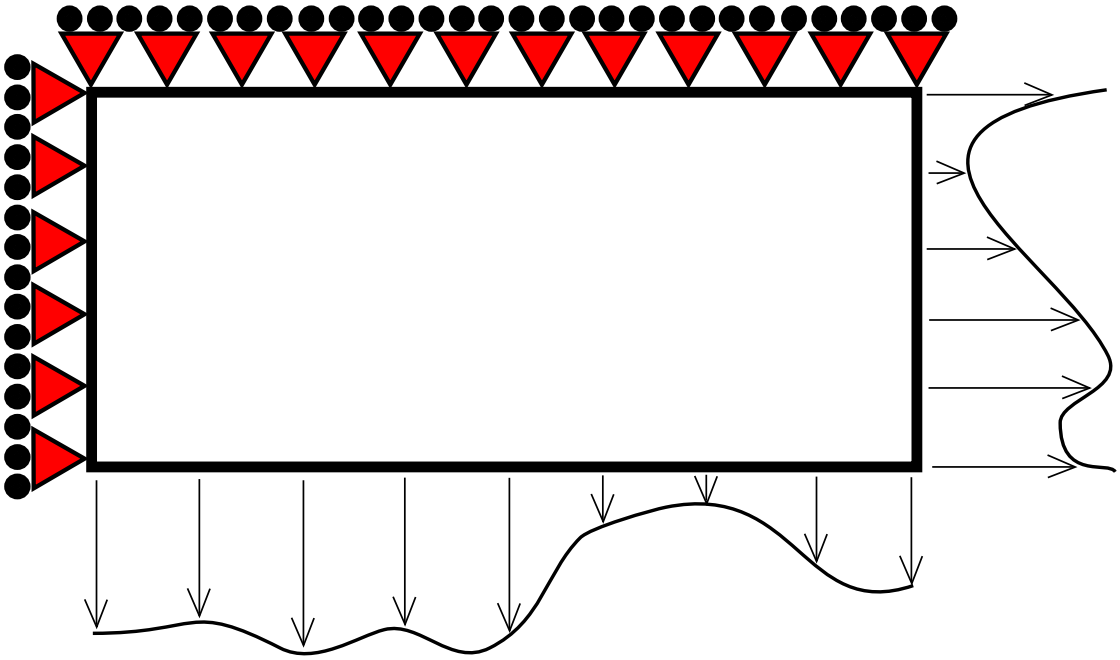

Figure 7.1: Prestress parameterization for the aeroelastic optimization

is non-negative. The negative membrane stress can cause membrane wrinkling, which is not modeled in a linear structural analysis. The positive principal stresses ensure that wrinkling will not occur[89]. The Von Mises criteria is used to make sure that yielding does not occur in the material. Formally, the problem statement is written as

$$\begin{gathered} min: \ -T_{avg} \\ st: \ \sigma_1 > 0 \\ \sigma_2 > 0 \\ \tfrac{1}{2}\left[(\sigma_x)^2 + (\sigma_y)^2 + (\sigma_x - \sigma_y)^2\right]^{1/2} \leq S_Y \end{gathered} \tag{7.1}$$

Several scenarios are considered in the design optimization. First, the planform of the membrane wing is fixed to be three specific shapes: rectangle, triangle, and half-ellipse. Then the modified Zimmerman design variables are added to the optimization so that the planform is allowed to be any shape that is symmetric about the midchord.

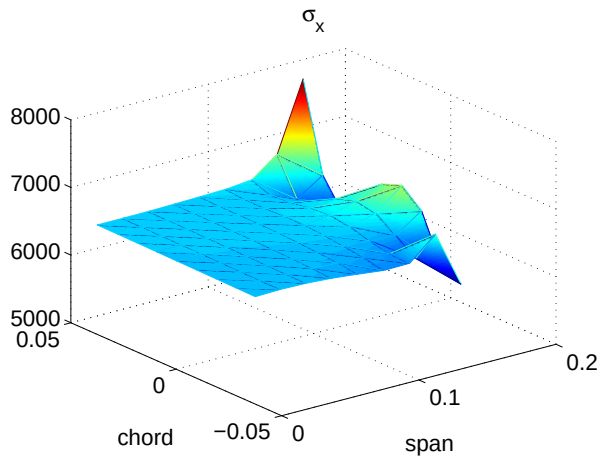

Figure 7.2: Optimal prestress distribution, σ_x, for a rectangular wing

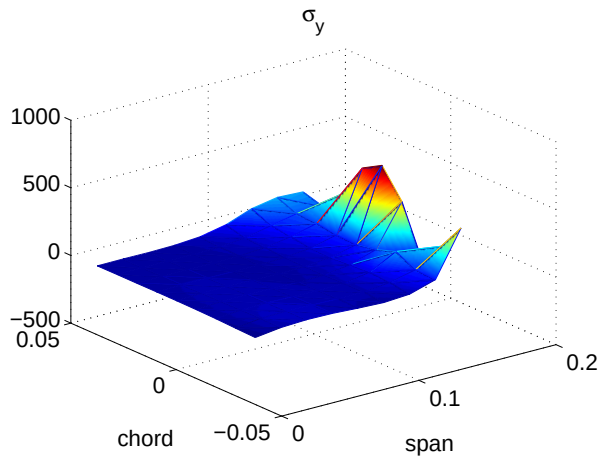

Figure 7.3: Optimal prestress distribution, σ_y, for a rectangular wing

7.1.1 Rectangular Membrane Wing

The first fixed planform is the rectangular membrane wing. The rectangular membrane wing has an aspect ratio of two and a span of 15cm. The optimal prestress distribution is shown in Figures 7.2-7.3. It is seen that both σ_x and σ_y are nearly uniform throughout the wing, except at the edges of the membrane, where the effects of the point-loads are seen. Also it is seen that σ_x is an order of magnitude greater than σ_y.

The deformation of the wing over the flapping cycle is illustrated in Figures 7.4a-7.5f. The wing downstroke is shown in Figure 7.4 with the upstroke shown in 7.5. Each subfigure

shows the position of the rigid-body motion of the flapping wing on the left side with the wing deformation shown on the right side. The deformation in each subfigure is magnified by an order of magnitude to make the deformation more readily apparent. During the downstroke and the upstroke, the wing deformation occurs mostly near the leading edge of the wing, where the largest aerodynamic pressure will act. At the end of each downstroke or upstroke, the inertia of the membrane dictates the deformation and the the wing deforms as though a uniform pressure is acting over the wing.

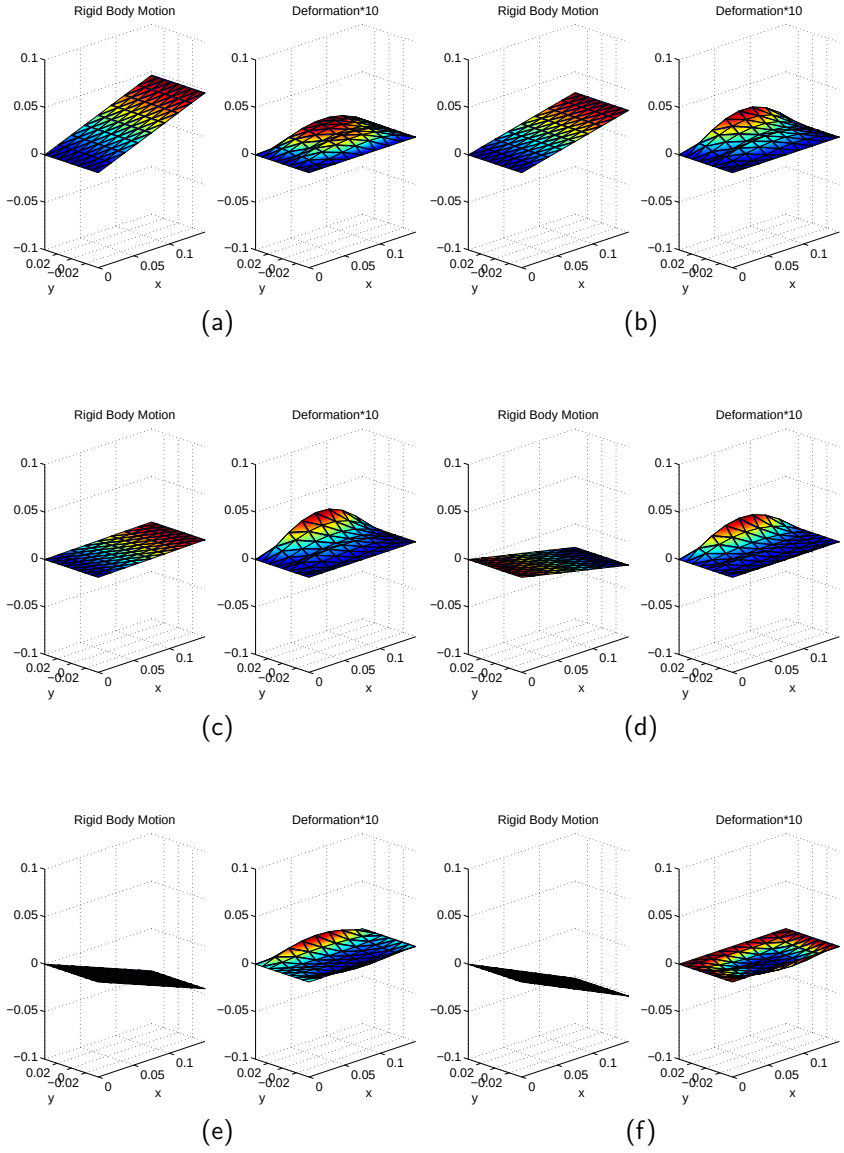

Figure 7.4: Rectangular membrane wing deformation during the downstroke

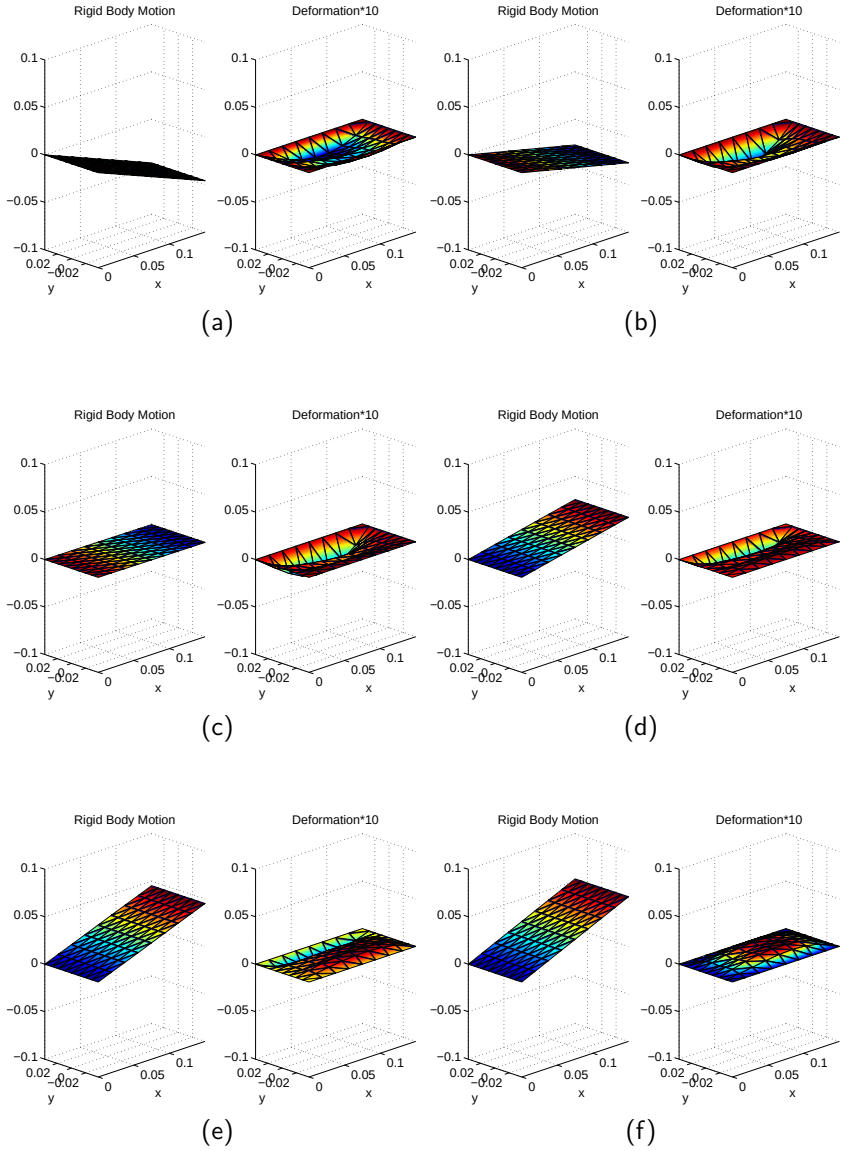

Figure 7.5: Rectangular membrane wing deformation during the upstroke

7.2 Shape and Prestress Optimization

The modified Zimmerman parameters are now added to the design problem. With the addition of shape variables, a constraint needs to be added to the problem so that the optimizer does not simply create a wing design which maximizes the span and chord to the

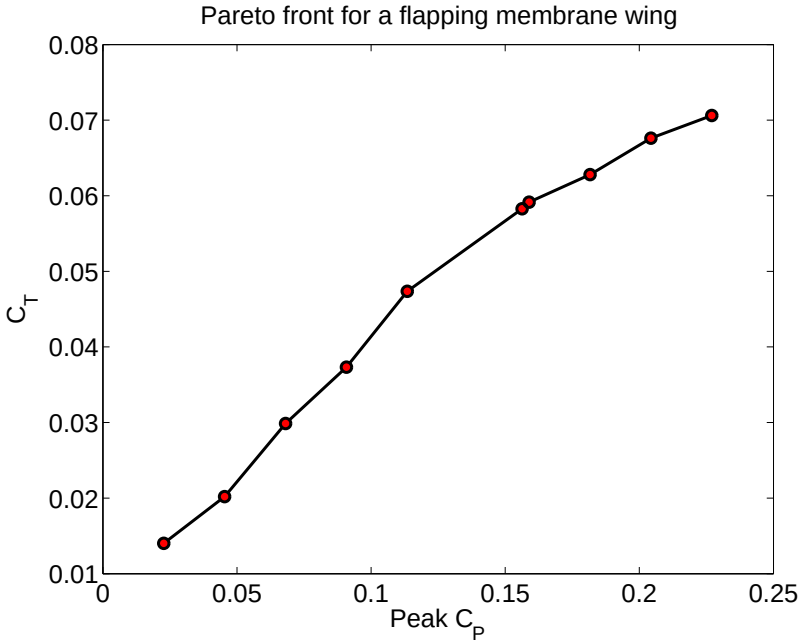

Figure 7.6: Pareto front for shape and structural optimization of membrane wings

upper bounds. So a peak power constraint is added to the problem as was done with the plate-like wings

$$\begin{aligned} min: \ & -T_{avg} \\ st: \ & P_{peak} < \epsilon \\ & \sigma_1 > 0 \\ & \sigma_2 > 0 \\ & \tfrac{1}{2}\left[(\sigma_x)^2 + (\sigma_y)^2 + (\sigma_x - \sigma_y)^2\right]^{1/2} \leq S_Y \end{aligned} \tag{7.2}$$

The Pareto front of designs for the membrane wing is shown in Figure 7.6.

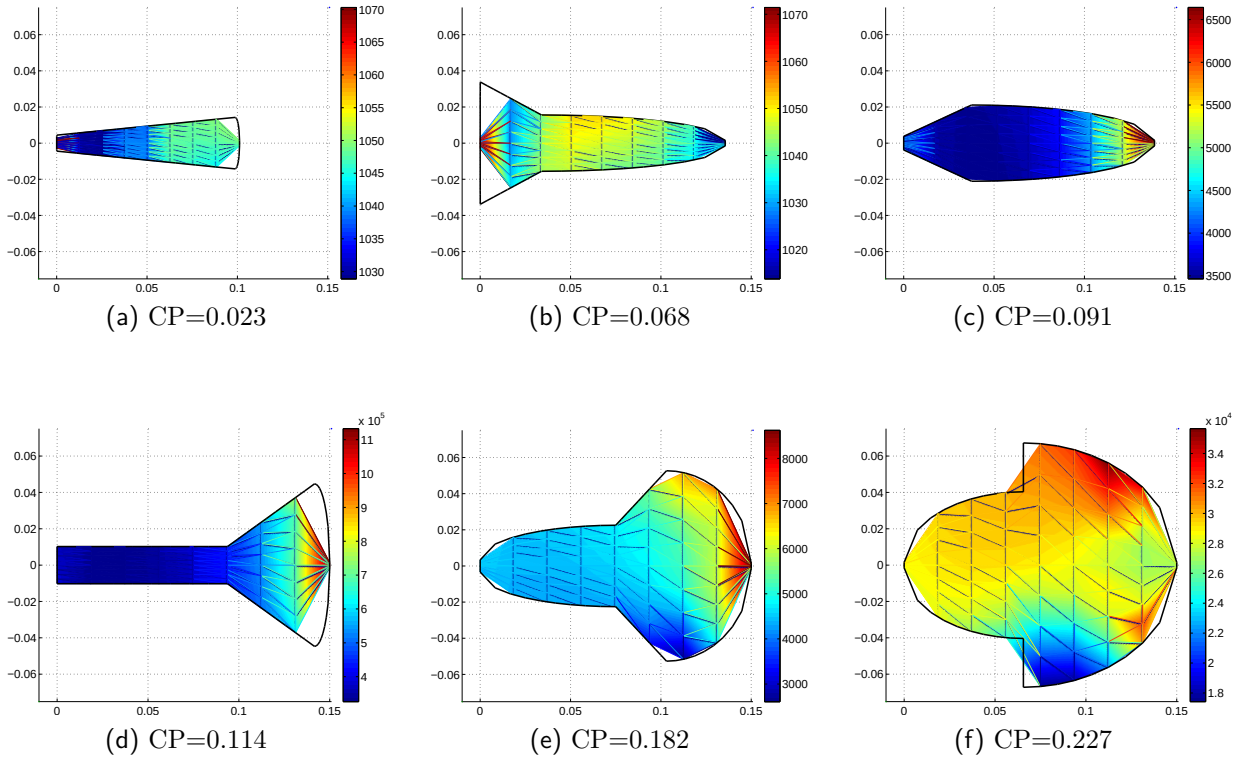

(a) CP=0.023 (b) CP=0.068 (c) CP=0.091

(d) CP=0.114 (e) CP=0.182 (f) CP=0.227

Figure 7.7: Pareto-optimal designs for membrane wings

As with the plate-like wings, the membrane wings tend toward designs which have little deformation over the flapping cycle because the deformation would increase the power constraint. Also, the contributions to the overall power can be shown for the membrane wing as with the plate-like wing. The optimal wing shown in Figure 7.7f gives the power-breakdown shown in Figure 7.8.

7.3 Unconstrained Optimization

In the membrane wing optimization, the power acts as the primary driver of the final design. However, the exploitation of the deformation for aerodynamic improvement is an important design consideration if the power constraint is ignored.

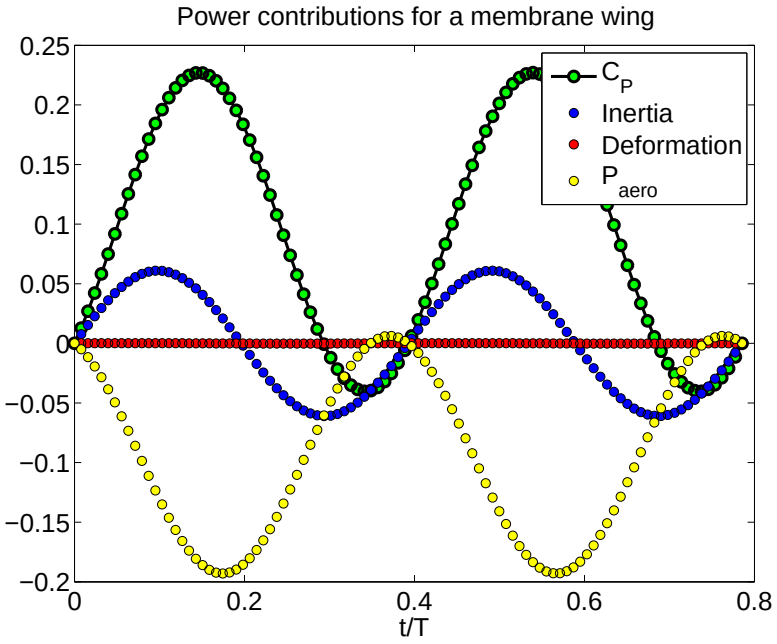

Figure 7.8: Example power breakdown for an optimal membrane wing

Some constraint is necessary in the aeroelastic optimization to prevent the final planform design from simply going to the upper bounds of the span and chord. For this case, the planform is fixed throughout the optimization procedure and just the prestress is optimized to maximize the thrust. The planforms that are used in the prestress optimization are those from the shape and prestress optimization in Section 7.2. The power-constrained Pareto front is shown in Figure 7.9 along with the results from the unconstrained optimization. There is thrust improvement for each of the membrane shapes along the Pareto surface. Both the thrust and the input power increase by 1-2% for each design. Both increases are due to the added power from the deformation over the flapping cycle. The breakdown of the power over the flapping cycle for design with the most relaxed constraint is shown in Figure 7.10. Along with the power breakdown for the constrained optimal planform, the power breakdown for the same planform which is optimized without the power constraint is shown. The figure shows the considerable increase in the power required to overcome the deformation. While the increase is small compared to the aerodynamic power and the inertial power (note the two scales on the vertical axes), it shows that the power constraint is an important factor in

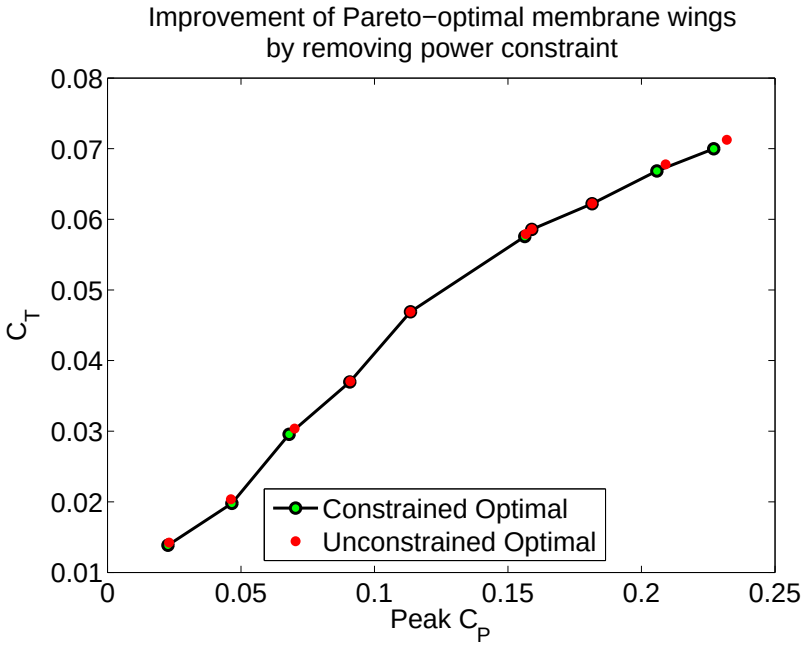

Figure 7.9: Membrane Pareto front with and without power constraint

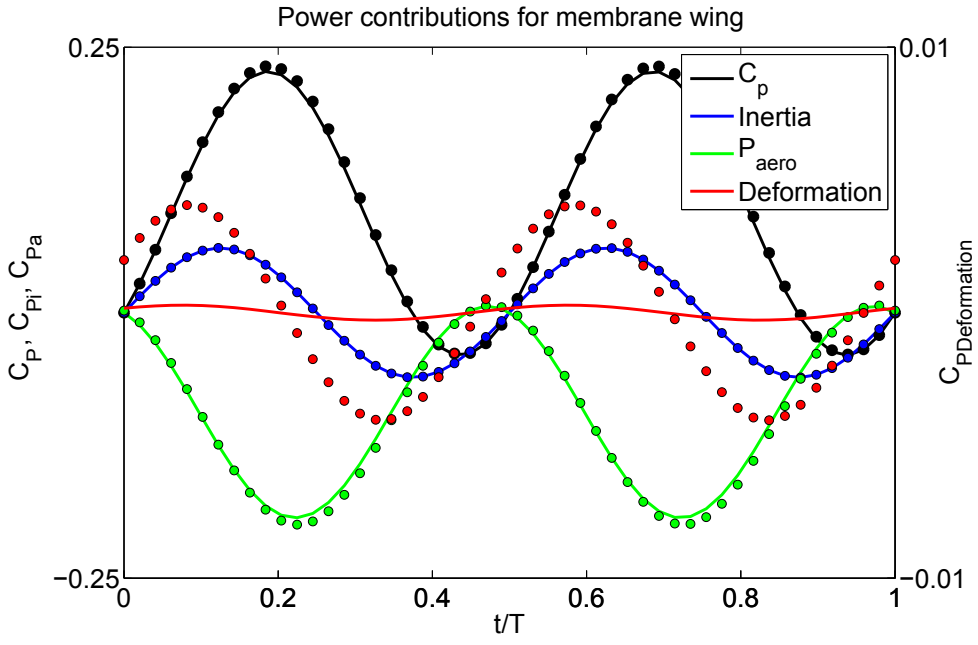

Figure 7.10: Power breakdown for the power-constrained membrane wing (solid lines) and for the optimized wing with no power constraint (dots)

the final, Pareto-optimal design.

7.4 Increasing the Design Space

Cubic polynomials are used to describe the membrane forces in the spanwise and chordwise directions. However, it may not be necessary to utilize the full design space to create wing designs which are optimal, or very nearly optimal. To test this, the prestress on a rectangular flapping wing with an aspect ratio of two is optimized using an increasing number of design variables. The force applied in the chordwise direction is

$$F_y = a_0 + a_1\xi + a_2\xi^2 + a_3\xi^3 \tag{7.3}$$

with the force applied in the spanwise direction as

$$F_x = b_0 + b_1\eta + b_2\eta^2 + b_3\eta^3 \tag{7.4}$$

During the optimizations, the full chordwise polynomial is used each time while the number of terms in the spanwise force polynomial is varied. The average coefficient of thrust is maximized subject to lower and upper stress constraints as stated in Eq. 7.1. The optimized coefficient of thrust is plotted as a function of the number of terms used in the spanwise force in Figure 7.11. It is seen that the optimized thrust is not improved by adding terms to the spanwise force polynomial. This is because the optimizer makes the membrane wings very stiff to maximize the thrust over the flapping cycle. The added polynomial terms are not beneficial because the optimizer has already increased the prestress of the wing and decreased the deformation to the point where the membrane wing is effectively rigid.

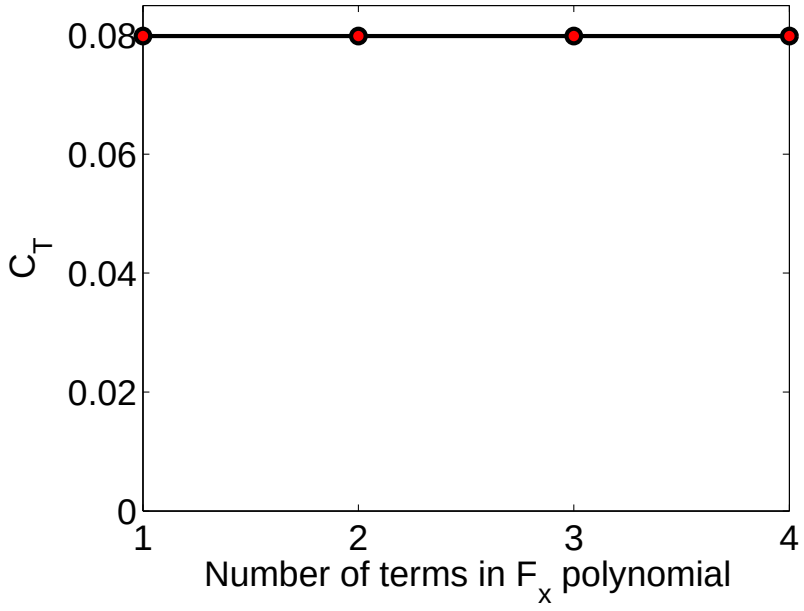

Figure 7.11: Coefficient of thrust compared to the number of polynomial terms used in the spanwise force

Chapter 8

Conclusions and Future Work

8.1 Conclusions

This work presents shape and structural optimization of flapping wings. Three wing types are modeled: rigid, plate-like deformable, and membrane-like deformable.

First the wing is modeled as a rigid wing and Peters' quasi-steady aerodynamic model is used to predict the required input power and thrust produced over one flapping cycle. During the optimization the wing area and required input power are minimized while the thrust produced over one flapping cycle is maximized. The design variables are the parameters from the modified Zimmerman parameterization method, a novel shape parameterization technique. The ϵ-constraint method is used to calculate the Pareto surface for this multiobjective optimization problem. The input power and the wing area, a surrogate for wing mass, are treated as nonlinear constraints. Some Pareto-optimal designs are driven by the non-linear power constraint, some designs are driven by the area constraint, while other designs are determined from both constraints. When only the area constraint is active, the optimizer tends to push the wing mass as far toward the tip as possible while still generating thrust. This leads to tear-drop wing shapes which are located near the wing tip. When only the power constraint is active, the optimizer tends to create wings which have most of the wing mass at the root in an effort to minimize the induced drag.

The flapping wing is then allowed to deform by using a plate finite element model. The finite element model is tightly coupled to an unsteady vortex lattice aerodynamic model to create a low cost aeroelastic model. A six-term polynomial is used to describe the thickness distribution, which determines both the mass and stiffness distribution. The coefficients of the thickness polynomial and the parameters of modified Zimmerman are the design variables. The objective of the problem is to maximize the cycle-averaged thrust while minimizing the peak power over the flapping cycle.

During the optimization of the plate-like deformable wings, there are two mechanisms that the optimizer exploits to maximize the thrust. The first aerodynamic mechanism that the optimizer uses is the minimization of the induced drag on the wing, leading to rigid high-aspect ratio wings. The rigidity of the wings saves power by limiting the deformation which occurs over the flapping cycle. The high-aspect ratio wing designs are optimal when the allowable peak input power is small. When the constraint on the power is relaxed, the optimizer takes advantage of the deformation of the wing to improve the thrust rather than minimizing the induced drag. The wing deformation increases the thrust produced over the flapping cycle while simultaneously increasing the input power required to flap the wing. This is because the input power required to overcome the wing deformation is in phase with the input power needed to produce the rigid-body motion of the wing, thus increasing the peak input power over the flapping cycle. The Pareto-optimal designs exploit one of the two mechanisms to benefit thrust, either wing deformation or minimization of the induced drag.

The density of the wing material plays a roll in the optimal wing design. A material with a small density needs less power allocated to the rigid-body motion and, therefore, can have more power devoted to the wing deformation. Also, much of the wing area can be allocated near the wing tip, which increases the inertial loads on the wing and promotes deformation over the flapping cycle. A wing material with a high density leads to wings that have large deformations over the flapping cycle. The large deformation is out of phase with the rigid-body motion and cancels out the inertial power, thus decreasing the input power needed by the design.

The analysis of membrane-like wings was performed using finite elements. The aeroelastic model used for the plate-like wing is modified and used with the membrane elements. The in-plane prestress on the membrane wing controls the stiffness of the membrane. The coefficients on the in-plane prestress polynomials are the design variables of the problem along with the modified Zimmerman parameters. The optimal membrane wings tend to create wings with little deformation, like their plate-wing cousins. Also, the optimal wing move more of the wing mass toward the tip as the power constraint increases. The design space of the membrane prestress is described as two cubic polynomials that define the force applied in the spanwise and chordwise directions. However, it is found that utilization of the full design space is not needed to get optimal performance from a membrane wing. This is because a membrane wing with a large stiffness can be created with a large uniform spanwise force.

8.2 Future Work

Subsequent studies should first focus on the calculation of the analytical sensitivities of the objective function to the parameters in the modified Zimmerman method. The sensitivities used in the optimization are calculated using central finite difference. The finite differentiation is prone to inaccuracies and is highly dependent on the finite difference step size; it is also very costly as it requires two extra evaluations of the objective for each design variable for each iteration. Calculation of the analytical sensitivities can both improve accuracy as well as decrease computational cost.

This work can easily be extended by simply removing the modified Zimmerman constraints that require symmetric wings. The symmetric constraints on the wings prevent the possibility that the optimizer might go toward a more biomimetic shape. Also, the boundary conditions at the wing root are clamped, which prevents twisting that can be caused by asymmetric designs. Manipulation of the boundary conditions can lead to investigations into the wing hinge design and location.

Finally, the design space should be explored using different models to calculate the ob-

jective. This study is based on a simplified UVLM aerodynamic model and linear structural models. It would be interesting if a high-fidelity model were used in conjunction with response surface techniques to optimize the flapping wing design. Alternatively, the objective can be calculated through experiments to compute the optimal design.

Bibliography

[1] Heathcote, S., Wang, Z.-J., , and Gursul, I., "Effect of Spanwise Flexibility on Flapping Wing Propulsion," *Journal of Fluids and Structures*, Vol. 24, 2008, pp. 183–199.

[2] Brooks, A., MacCready, P., Lissaman, P., and Morgan, W., "Development of a Wing-Flapping Flying Replica of the Largest Pterosaur," *Proceedings of the 21st AIAA Joint Propulsion Conference*, Monterey, CA, July 8-10 1985.

[3] DeLaurier, J. D. and Harris, J. M., "A Study of Mechanical Flapping-Wing Flight," *The Aeronautical Journal*, Vol. 97, No. 970, October 1993, pp. 277–286.

[4] McMichael, J. M. and Francis, M. S., "Micro Air Vehicles - Toward a New Dimension of Flight," Tech. rep., DARPA, 1997.

[5] Colorado, J., Barrientos, A., Rossi, C., and Breuer, K. S., "Biomechanics of smart wings in a bat robot: morphing wings using SMA actuators," *Bioinspiration and Biomimetics*, Vol. 7, 2012, pp. 1–16.

[6] Day, A. H., *Optimization of a Micro Aerial Vehicle Planform Using Genetic Algorithms*, M.s. thesis, Mechanical Engineering Dept., Worcester Polytechnic Institute, Worcester, MA, 2007.

[7] Wood, R. J., "The First Takeoff of a Biologically Inspired At-Scale Robotic Insect," *IEEE Transactions on Robotics*, Vol. 24, No. 2, April 2008, pp. 341–347.

[8] Ma, K. Y., Chirattananon, P., Fuller, S. B., and Wood, R. J., "Controlled Flight of a Biologically Inspired, Insect-Scale Robot," *Journal of Science*, Vol. 340, No. 603, 2013, pp. 603–607.

[9] Peters, D. A., Hsieh, M. A., and Torrero, A., "A State-Space Airloads Theory for Flexible Airfoils," *American Helicopter Society 62nd Annual Forum*, Phoenix, AZ, May 9-11 2006.

[10] Anderson, J. D., *Fundamentals of Aerodynamics*, McGraw-Hill, New York, NY, 2nd ed., 1991.

[11] Pesavento, U. and Wang, Z. J., "Flapping Wing Flight Can Save Aerodynamic Power Compared to Steady Flight," *Physical Review Letters*, Vol. 103, No. 11, 2009, pp. 118102.

[12] Hsu, C.-K., Evans, J., Vytla, S., and Huang, P., "Development of Flapping Wing Micro Air Vehicles -Design, CFD, Experiment and Actual Flight," *48th AIAA Aerospace Sciences Meeting*, Orlando, FL, January 4-7 2010.

[13] Keennon, M., Klingebiel, K., and Won, H., "Development of the Nano Hummingbird: A Tailless Flapping Wing Micro Air Vehicle," *Proceedings of the 50th AIAA Aerospace Sciences Meeting*, Nashville, TN, January 9-12 2012.

[14] Pesavento, U. and Wang, Z. J., "Falling Paper: Navier-Stokes Solutions, Model of Fluid Forces, and Center of Mass Elevation," *Physical Review Letters*, Vol. 93, No. 14, 2004, pp. 144501.

[15] Andersen, A., Pesavento, U., and Wang, Z. J., "Unsteady Aerodynamics of Fluttering and Tumbling Plates," *Journal of Fluid Mechanics*, Vol. 541, 2005, pp. 65–90.

[16] Berman, G. J. and Wang, Z. J., "Energy-Minimizing Kinematics in Hovering Insect Flight," *Journal of Fluid Mechanics*, Vol. 582, 2007, pp. 153–168.

[17] Sane, S. P. and Dickinson, M. H., "The Control of Flight Force by a Flapping Wing: Lift and Drag Production," *Journal of Experimental Biology*, Vol. 204, 2001, pp. 2607–2626.

[18] Ansari, S. A., Zbikowski, R., and Knowles, K., "Non-linear Unsteady Aerodynamic Model for Insect-like Flapping Wings in the Hover. Part 1: methodology and analysis," *Proceedings of the Institution of Mechanical Engineering, Part G: Journal of Aerospace Engineering*, Vol. 220, No. 2, 2006, pp. 61–83.

[19] Ansari, S. A., Zbikowski, R., and Knowles, K., "Non-linear Unsteady Aerodynamic Model for Insect-like Flapping Wings in the Hover. Part 2: Implementation and Validation," *Proceedings of the Institution of Mechanical Engineering, Part G: Journal of Aerospace Engineering*, Vol. 220, No. 3, 2006, pp. 169–186.

[20] Dickinson, M. H. and ans Sanjay P. Sane, F.-O. L., "Wing Rotation and the Aerodynamic Basis of Insect Flight," *Journal of Science*, Vol. 284, No. 5422, June 1999, pp. 1954–1960.

[21] Walker, W. P. and Patil, M. J., "Unsteady Aerodynamics of Deformable Thin Airfoils," *48th AIAA Aerospace Sciences Meeting*, Orlando, FL, 4-7 January 2010.

[22] Taha, H. E., Hajj, M. R., and Nayfeh, A. H., "Optimization of Wing Kinematics for Hovering MAVs Using Calculus of Variation," *Proceedings of the 14th AIAA/ISSM Multidisciplinary Analysis and Optimization Conference*, Indianapolis, IN, Septemer 17-19 2012.

[23] Peters, D. A., Karunamoorthy, S., and Cao, W.-M., "Finite State Induced Flow Models Part I: Two-Dimensional Thin Airfoils," *Journal of Aircraft*, Vol. 32, No. 2, March-April 1995, pp. 313–322.

[24] Bierling, T., *Nonlinear Dynamics and Stability of Flapping-Wing Flight*, M.s. thesis, Technische Universitat Munchen, Munich, Germany, 2009.

[25] Richter, M. N. and Patil, M. J., "Infuence of Wing Flexibility on the Stability of Flapping Flight," *AIAA Atmospheric Flight Mechanics Conference*, Toronto, Ontario Canada, August 2-5 2010.

[26] Leonard, B. Y., *Flapping Wing Flight Dynamic Modeling*, Master's thesis, Virginia Tech, Blacksburg, VA, 2011.

[27] Stanford, B., Kurdi, M., Beran, P., and McClung, A., "Shape, Structure, and Kinematic Parameterization of a Power-Optimal Hovering Wing," *AIAA Structures, Structural Dynamics, and Materials Conference*, Orlando, FL, April 12-15 2010.

[28] Stanford, B., Beran, P., and Kobayashi, M., "Aeroelastic Optimization of Flapping Wing Venation: A Cellular Division Approach," *AIAA Structures, Structural Dynamics, and Materials Conference*, Denver, CO, April 4-7 2011.

[29] Stewart, E. C., Patil, M. J., Canfield, R. A., and Snyder, R. D., "Parametric Representation and Shape Optimization of Flapping Micro Air Vehicle Wings," *International Journal of Micro Air Vehicles*, Vol. 4, 2012, pp. 179–202.

[30] Katz, J. and Plotkin, A., *Low-Speed Aerodynamics*, Cambridge University Press, New York, NY, 2nd ed., 2001.

[31] Smith, M. J., "The Effects of Flexibility on the Aerodynamics of Moth Wings: Towards the Development of Flapping-Wing Technology," *AIAA Aerospace Sciences Meeting*, Reno, NV, January 9-12 1995.

[32] Smith, M. J. C., "Simulating Moth Wing Aerodynamics: Towards the Development of Flapping-Wing Technology," *AIAA Journal*, Vol. 34, No. 7, July 1996, pp. 1348–1355.

[33] Stanford, B. K. and Beran, P. S., "Analytical Sensitivity Analysis of an Unsteady Vortex-Lattice Method for Flapping-Wing Optimization," *Journal of Aircraft*, Vol. 47, No. 2, March-April 2010, pp. 647–662.

[34] Ghommem, M., *Modeling and Analysis for Optimization of Unsteady Aeroelastic Systems*, Ph.D. thesis, Virginia Tech, Blacksburg, VA, 2011.

[35] Stewart, E. C., Patil, M. J., Canfield, R. A., and Snyder, R. D., "Aeroelastic Shape Optimization of a Plunging Plate," *Proceedings of the 52nd AIAA Structures, Structural Dynamics, and Materials Conference*, Honolulu, HI, April 23-26 2012.

[36] Stewart, E. C., Patil, M. J., Canfield, R. A., and Snyder, R. D., "Aeroelastic Optimization of Membrane Prestress on a Flapping Wing," *Proceedings of the 14th AIAA/ISSM Multidisciplinary Analysis and Optimization Conference*, Indianapolis, IN, September 17-19 2012.

[37] Ahmadi, A. R. and Widnall, S. E., "Unsteady Lifting-Line Theory with Applications," *AIAA Aerospace Sciences Meeting*, Orlando, FL, January 11-14 1982.

[38] Archer, R. D., Sapuppo, J., and Betteridge, D. S., "Propulsion Characteristics of Flapping Wings," *Aeronautical Journal*, Vol. 83, 1979, pp. 355–371.

[39] Betteridge, D. S. and Archer, R. D., "A Study of the Mechanics of Flapping Wings," *The Aeronautical Quarterly*, Vol. 25, 1974, pp. 129–142.

[40] Phlips, P. J., East, R. A., and Pratt, N. H., "An Unsteady Lifting Line Theory of Flapping Wings with Applications to the Forward Flight of Birds," *Journal of Fluid Mechanics*, Vol. 112, 1981, pp. 97–125.

[41] Theodorsen, T., "General Theory of Aerodynamic Instability and the Mechanism of Flutter," Tech. rep., NACA TR No. 496, May 1934.

[42] Garrick, I. E., "Propulsion of a Flapping and Oscillating Airfoil," Tech. rep., NACA TR No. 567, 1936.

[43] Masoud, H. and Alexeev, A., "Resonance of Flexible Flapping Wings at Low Reynolds Number," *Physical Review E*, Vol. 81, No. 5, May 2010, pp. 056304.

[44] Persson, P.-O. and Willis, D. J., "High Fidelity Simulations of Flapping Wings Designed for Energetically Optimal Flight," *49th AIAA Aerospace Sciences Meeting*, Orlando, FL, January 4-7 2011.

[45] Fitzgerald, T., Valdez, M., Vanella, M., Balaras, E., and Balachandran, B., "Flexible Flapping Systems: Computational Investigations into Fluid-Structure Interactions," *The Aeronautical Journal*, Vol. 115, No. 1172, 2011, pp. 593–604.

[46] Trizila, P., Kang, C.-K., Aono, H., Shyy, W., and Visbal, M., "Low-Reynolds-Number Aerodynamics of a Flapping Rigid Flat Plate," *AIAA Journal*, Vol. 49, No. 4, April 2011, pp. 806–823.

[47] Ansari, S. A., Knowles, K., and Zbikowski, R., "Insectlike Flapping Wings in the Hover Part 2: Effect of Wing Geometry," *Journal of Aircraft*, Vol. 45, No. 6, 2008, pp. 1976–1990.

[48] Ansari, S. A., Knowles, K., and Zbikowski, R., "Insectlike Flapping Wings in the Hover Part 1: Effect of Wing Kinematics," *Journal of Aircraft*, Vol. 45, No. 6, November-December 2008, pp. 1945–1954.

[49] Isogai, K. and Harino, Y., "Optimum Aeroelastic Design of a Flapping Wing," *Journal of Aircraft*, Vol. 44, No. 6, November-December 2007, pp. 2040–2048.

[50] Stanford, B. K. and Beran, P., "Formulation of Analytical Design Derivatives for Nonlinear Unsteady Aeroelasticity," *AIAA Structures, Structural Dynamics, and Materials Conference*, Orlando, FL, April 12-15 2010.

[51] Banerjee, S. P. and Patil, M. J., "Aeroelastic Analysis of Membrane Wings," *AIAA Structures, Structural Dynamics, and Materials Conference*, Schaumburg, IL, 7-10 2008.

[52] Walker, W. P., Patil, M. J., and Canfield, R. A., "Aeroelastic Tailoring of Flapping Membrane Wings for Maximum Thrust and Propulsive Efficiency," *Proceedings of the 14th AIAA Multidisciplinary Analysis and Optimization Conference*, Indianapolis, IN, 2012, (submitted for publication).

[53] Moschetta, J.-M. and Thipyopas, C., "Optimization of a Biplane Micro Air Vehicle," *AIAA Applied Aerodynamics Conference*, Toronto, Ontario, Canada, June 6-8 2005.

[54] Jagdale, V., Ifju, P., Patil, A., , and Stanford, B., "Deterministic Design Optimization of a Bendable Load Stiffened UAV Wing," *AIAA Aerospace Sciences Meeting*, Orlando, FL, January 4-7 2010.

[55] Choi, K. K. and Kim, N.-H., *Structural Sensitivity Analysis and Optimization 2: Nonlinear Systems and Applications*, Springer, 2005.

[56] Haftka, R. T. and Grandhi, R. V., "Structural Shape Optimization - A Survey," *Computer Methods in Applied Mechanics and Engineering*, Vol. 57, No. 1, 1986, pp. 91–106.

[57] Stanford, B. and Ifju, P. G., "Multi-Objective Topology Optimization of Wing Skeletons for Aeroelastic Membrane Structures," *International Journal of Micro Air Vehicles*, Vol. 1, No. 1, March 2009, pp. 51–69.

[58] Torres, G. E. and Mueller, T. J., "Low-Aspect-Ratio Wing Aerodynamics at Low Reynolds Numbers," *AIAA Journal*, Vol. 42, No. 5, May 2004, pp. 865–873.

[59] Kurdi, M., Stanford, B., and Beran, P., "Kinematic Optimization of Insect Flight for Minimum Mechanical Power," *48th AIAA Aerospace Sciences Meeting*, Orlando, FL, January 4-7 2010.

[60] Ghommem, M., Hajj, M. R., Watson, L. T., Mook, D. T., Snyder, R. D., and Beran, P., "Deterministic Global Optimization of Flapping Wing Motion for Micro Air Vehicles," *13th AIAA Mutidisciplinary Analysis Optimization Conference*, Fort Worth, TX, September 13-15 2010.

[61] Thompson, S. L., Mattson, C. A., Colton, M. B., Harston, S. P., Carlson, D. C., and Cutler, M., "Experiment-Based Optimization of Flapping Wing Kinematics," *Proceedings of the 47th AIAA Aerospace Sciences Meeting*, Orlando, FL, January 5-8 2009.

[62] Stanford, B. K., Beran, P., and Kobayashi, M., "Simultaneous Topology Optimization of Membrane Wings and Their Compliant Flapping Mechanisms," *Proceedings of the*

53rd AIAA Structures, Structural Dynamics, and Materials Conference, Honolulu, HI, April 23-26 2012.

[63] Ghommem, M., Hajj, M. R., Stanford, B. K., Watson, L. T., and Beran, P. S., "Global and Local Optimization of Flapping Kinematics," *Proceedings of the 53rd AIAA Structures, Structural Dynamics, and Materials Conference*, Honolulu, HI, April 23-26 2012.

[64] Stearman, R. O., *The Stability of a Membrane in Subsonic Flow*, Ph.D. thesis, California Institute of Technology, Pasadena, CA, 1961.

[65] Irvine, H. M., "A Note on Luffing in Sails," *Proceedings of the Royal Society of London*, Vol. 365, 1979, pp. 345–347.

[66] Newman, B. G. and Pa*ddot*(i)doussis, M. P., "The Stability of Two-Dimensional Membranes in Streaming Flow," *Journal of Fluids and Structures*, Vol. 5, 1991, pp. 443–454.

[67] Sygulski, R., "Stability of Membrane in Low Subsonic Flow," *International Journal of Non-Linear Mechanics*, Vol. 42, 2007, pp. 196–202.

[68] Gibbs, S. C., Wang, I., Bloomhardt, E., and Dowell, E. H., "Aeroelastic Behavior of Noise-Reducing Membranes for Aircraft Lifting Surfaces Part I: Theory," *AIAA Structures, Structural Dynamics, and Materials Conference*, Honolulu, HI, April 23-26 2012.

[69] Richter, M. N., *Influence of Flexibility on the Stability of Flapping Flight*, Master's thesis, Technische Universitat Munchen, 2010.

[70] Mueller, T. J., editor, *Fixed and Flapping Wing Micro Air Vehicle Applications*, AIAA, Reston, VA, 2001.

[71] Zimmerman, C. H., "Aerodynamic Characteristics of Several Airfoils of Low Aspect Ratio," Technical Note 539, NACA, Washington, D. C., August 1935.

[72] Turan, M., Canfield, R. A., and Harmon, F., "Tools for the Conceptual Design and Engineering Analysis of Micro Air Vehicles," *47th AIAA Aerospace Sciences Meeting*, No. AIAA-2009-38, Orlando, Florida, Jan. 5-8 2009.

[73] Hutchinson, J. R. and Smith, D., "Chiropteran Flight," http://www.ucmp.berkeley.edu/vertebrates/flight/bats.html, September 2005, [Cited 1 March 2010].

[74] Sane, S. P. and Dickinson, M. H., "The Aerodynamic Effects of Wing Rotatoin and a Revised Quasi-Steady Model of Flapping Flight," *Journal of Experimental Biology*, Vol. 205, 2002, pp. 1087–1096.

[75] Heathcote, S., Wang, Z.-J., , and Gursul, I., "Effect of Spanwise Flexibility on Flapping Wing Propulsion," *36th AIAA Fluid Dynamics Conference and Exhibit*, San Francisco, CA, June 5-8 2006.

[76] Batoz, J.-L., Bathe, K.-J., and Ho, L.-W., "A Study of Three-node Triangular Plate Bending Element," *International Journal for Numerical Methods in Engineering*, Vol. 15, No. 12, 1980, pp. 1771–1812.

[77] Batoz, J.-L., "An Explicit Formulation for an Efficient Triangular Plate-Bending Element," *International Journal for Numerical Methods in Engineering*, Vol. 18, No. 7, 1982, pp. 1077–1089.

[78] Cooke, R. D., Malkus, D. S., Plesha, M. E., and Witt, R. J., *Concepts and Applications of Finite Element Analysis*, John Wiley & Sons, New York, 4th ed., 2002.

[79] Kansara, K., *Development of Membrane, Plate and Flat Shell Elements in Java*, Master's thesis, Civil Engineering Dept., Virginia Polytechnic Institute and State University, Blacksburg, VA, 2004.

[80] Reddy, J. N., *Theory and Analysis of Elastic Plates and Shells*, CRC Press, 2007.

[81] Kim, N. H. and Sankar, B., *Finite Element Analysis and Design*, John Wiley & Sons, 2009.

[82] Chimakurthi, S. K., Tang, J., Palacios, R., Cesnik, C. E. S., and Shyy, W., "Computational Aeroelasticity Framework for Analyzing Flapping Wing Micro Air Vehicles," *AIAA Journal*, Vol. 47, No. 8, August 2009, pp. 1865–1878.

[83] Tang, D., Dowell, E. H., and Hall, K. C., "Limit Cycle Oscillations of a Cantilevered Wing in Low Subsonic Flow," *AIAA Journal*, Vol. 37, No. 3, 1999, pp. 364–371.

[84] Haftka, R. T. and Kamat, M. P., *Elements of Structural Optimization*, Martinus Nijhoff Publishers, The Hague, 1985.

[85] Haftka, R. T. and Gurdal, Z., *Elements of Structural Optimization*, Kluwer Academic Publishers, Dordrecht, 1992.

[86] Marler, R. T. and Arora, J. S., "Survey of Multi-Objective Optimization Methods for Engineering," *Structural and Multidisciplinary Optimization*, Vol. 26, No. 6, 2004, pp. 369–395.

[87] Duckstein, L., "Multiobjective Optimization in Structural Design: The Model Choice Problem," *New Directions in Optimum Structural Design*, edited by E. Atrek, R. H. Gallagher, K. M. Ragsdell, and O. C. Zienkiewicz, John Wiley & Sons, 1984, pp. 459–481.

[88] Carmichael, D. G., "Computation of Pareto Optima in Structural Design," *International Journal for Numerical Methods in Engineering*, Vol. 15, 1980, pp. 925–929.

[89] Stein, M. and Hedgepeth, J. M., "Analysis of Partly Wrinkled Membranes," Technical Note NASA TN D-813, National Aeronautics and Space Administration, 1961.

Appendix A

Sensitivities for Quasi-Steady Aerodynamics

The sensitivities for average thrust over a cycle were calculated for a wing in flapping flight without inflow. The sensitivities were used to verify the shape optimizations that were performed for flapping flight. Peters' aerodynamics were used to find the average thrust and peak power on a single blade element. Only deviation is present in flapping kinematics as

$$\gamma = \gamma_{max} \sin(\omega t) \tag{A.1}$$

The freestream velocity parallel to the wing frame was prescribed as

$$u_0 = U_0 \tag{A.2}$$

The lift and drag on the blade element are

$$L = -2\pi\rho b\, u_0 v_0 - \pi\rho b^2 \dot{v}_0 \tag{A.3}$$

$$D = -2\pi\rho b\, v_0^2 \tag{A.4}$$

A.1 Thrust Sensitivities

The thrust in flapping flight is the negative of the drag. The average thrust T_{avg} over one period of flapping θ is calculated as

$$T_{avg} = \frac{1}{\theta}\int_0^{\theta} -D\,dt = \frac{1}{2}c\,l\,\pi r_{BL}^2\gamma_{max}^2\rho\omega^2 \tag{A.5}$$

The sensitivities of the thrust with respect to the chord, blade width, and hinge-to-blade distance were then analytically determined to be

$$\frac{\partial T_{avg}}{\partial c} = \frac{1}{2}l\pi r_{BL}^2\gamma_{max}^2\rho\omega^2 \tag{A.6}$$

$$\frac{\partial T_{avg}}{\partial l} = \frac{1}{2}c\pi r_{BL}^2\gamma_{max}^2\rho\omega^2 \tag{A.7}$$

$$\frac{\partial T_{avg}}{\partial r_{BL}} = cl\pi r_{BL}\gamma_{max}^2\rho\omega^2 \tag{A.8}$$

The sensitivities of thrust show that to maximize the average thrust of a single blade element, the chord and blade width are maximized and the blade element should be located at the wing tip.

A.2 Power Sensitivities

The peak power was found by first calculating the power required during one flapping period. For pure flapping without inflow the calculations for the power reduce to

$$P_{aero} = L_0\,v_0 \tag{A.9}$$

$$P = M_x\dot{\gamma} - P_{aero} \tag{A.10}$$

The effect of drag on the power required was ignored because the velocity of the flow parallel to the wing is dependent only on the freestream. Power over a given cycle is

$$P = K_1 \sin(\omega t)\left(K_2 \cos(\omega t) + K_3 \sin(\omega t)\right) \tag{A.11}$$

where K_1, K_2, and K_3 are constants with respect to time

$$K_1 = \frac{1}{12} c l \gamma_{max}^2 \omega^2 \tag{A.12}$$

$$K_2 = \omega\left(3\pi\rho c\, r_{BL}^2 + \left(l^2 + 12\, r_{BL}^2\right) h\rho_w\right) \tag{A.13}$$

$$K_3 = 12\pi\rho r_{BL}^2 U_0 \tag{A.14}$$

In equation A.13 h is the thickness of the wing and ρ_w is the wing material density. The magnitude of the maximum power is found by combining the average and oscillatory parts of the power equation

$$P_{max} = \frac{K_1 K_3}{2} + \frac{K_1}{2}\sqrt{K_3^2 + K_2^2} \tag{A.15}$$

The sensitivities of the maximum power with respect to c, l, r_{BL} were then calculated by substituting the values for K_1, K_2, and K_3 back into expression for maximum power and differentiating with respect to the blade parameters.

$$\begin{aligned}\frac{\partial P_{max}}{\partial c} = \frac{1}{24} l \gamma_{max}^2 \omega^2 \Bigg(& 12\pi r_{BL}^2 U_0 \rho + \\ & \frac{3c\pi r_{BL}^2 \rho \left(l^2 h\rho_w + 3r_{BL}^2 (c\pi\rho + 4h\rho_w)\right)\omega^2}{\sqrt{144\pi^2 r_{BL}^4 U_0^2 \rho^2 + \left(l^2 h\rho_w + 3r_{BL}^2 (c\pi\rho + 4h\rho_w)\right)^2 \omega^2}} + \\ & \sqrt{144\pi^2 r_{BL}^4 U_0^2 \rho^2 + \left(l^2 h\rho_w + 3r_{BL}^2 (c\pi\rho + 4h\rho_w)\right)^2 \omega^2}\Bigg)\end{aligned} \tag{A.16}$$

$$\frac{\partial P_{max}}{\partial l} = \frac{1}{24} c\gamma_{max}^2 \omega^2 \Bigg(12\pi r_{BL}^2 U_0 \rho + \frac{2l^2 h\rho_w \left(l^2 h\rho_w + 3r_{BL}^2 (c\pi\rho + 4h\rho_w)\right)\omega^2}{\sqrt{144\pi^2 r_{BL}^4 U_0^2 \rho^2 + \left(l^2 h\rho_w + 3r_{BL}^2 (c\pi\rho + 4h\rho_w)\right)^2 \omega^2}} + \sqrt{144\pi^2 r_{BL}^4 U_0^2 \rho^2 + \left(l^2 h\rho_w + 3r_{BL}^2 (c\pi\rho + 4h\rho_w)\right)^2 \omega^2} \Bigg) \tag{A.17}$$

$$\frac{\partial P_{max}}{\partial r_{BL}} = \frac{1}{48} cl\gamma_{max}^2 \omega^2 \Bigg(48\pi r_{BL} U_0 \rho + \frac{576\pi^2 r_{BL}^3 U_0^2 \rho^2 + 12 r_{BL} (c\pi\rho + 4h\rho_w)\left(l^2 h\rho_w + 3r_{BL}^2 (c\pi\rho + 4h\rho_w)\right)\omega^2}{\sqrt{144\pi^2 r_{BL}^4 U_0^2 \rho^2 + \left(l^2 h\rho_w + 3r_{BL}^2 (c\pi\rho + 4h\rho_w)\right)^2 \omega^2}} \Bigg) \tag{A.18}$$

A.3 Nondimensional Variables

The average thrust and and peak power equations can be represented through nondimensional parameters. Both equations are normalized by a combination of air density ρ, freestream velocity U_0, and maximum span s. The nondimensional thrust and peak power equations take the form

$$\frac{T_{avg}}{\frac{1}{2}\rho U_0^2 s^2} = \frac{\frac{1}{2} c\omega l \omega \pi r_{BL}^2 \gamma_{max}^2 \rho}{\frac{1}{2} U_0^2 s^2 \rho} \tag{A.19}$$

$$\frac{P_{max}}{\frac{1}{2}\rho U_0^3 s^2} = \frac{\frac{1}{2} cl\pi r_{BL}^2 U_0 \gamma_{max}^2 \rho\omega^2}{\frac{1}{2}\rho U_0^3 s^2} + \frac{\frac{1}{24} cl\mu_{max}^2 \omega^2 \sqrt{144\pi^2 r_{BL}^4 U_0^2 \rho^2 + \left(3c\pi r_{BL}^2 \rho + \left(l^2 + 12r_{BL}^2\right) h\rho_w\right)^2 \omega^2}}{\frac{1}{2}\rho U_0^3 s^2} \tag{A.20}$$

and simplify to the nondimensional equations

$$\bar{T}_{avg} = 4\pi\gamma_{max}^2 k^2 \bar{r}^2 AR \tag{A.21}$$

$$\bar{P}_{max} = 4\pi\gamma_{max}^2 k^2 \bar{r}^2 \, AR + \sqrt{16\pi^2\gamma_{max}^4 k^4 \bar{r}^4 AR^2 + \left(2\gamma_{max}^2 k^3 \bar{r}^2 AR\mu_m\right)^2 \left(\frac{\pi}{\mu_m} + \frac{AR^2}{3\lambda} + 4\,\lambda\right)^2} \tag{A.22}$$

Several nondimensional parameters are introduced in equations A.21 and A.22. Let the aspect ratio be $AR = \frac{c}{l}$, nondimensional hinge-to-blade distance $\bar{r} = \frac{r_{BL}}{s}$, mass ratio term called $\mu_m = \frac{m_{wing}}{m_{air}} = \frac{\rho_w c\, l\, h}{\rho c\, l\, r_{BL}}$ and a taper ratio term called $\lambda = \frac{r_{BL}}{c}$, and reduced frequency be $k = \frac{\omega c}{2U_0}$.

A.4 Sensitivity Ratios

Equations (A.6-A.8) and (A.16-A.18) are combined to calculated the sensitivity ratios. Nondimensional parameters are used describe the sensitivity ratios as

$$\frac{\frac{\partial \bar{P}}{\partial r_{BL}}}{\frac{\partial T_{avg}}{\partial r_{BL}}} = 1 + \frac{\frac{72}{k} + 6k\left(1 + 4\mu_m\lambda^2 AR\right)\left(\frac{\mu_m}{AR} + \left(3 + 12\mu_m\lambda^2 AR\right)\right)}{12\sqrt{\frac{36}{k^2} + \left(\frac{\mu_m}{AR} + \left(3 + 12\mu_m\lambda^2 AR\right)\right)^2}} \tag{A.23}$$

$$\frac{\frac{\partial \bar{P}}{\partial c}}{\frac{\partial T_{avg}}{\partial c}} = 1 + \frac{k\left(\frac{\mu_m}{AR} + \left(3 + 12\mu_m\lambda^2 AR\right)\right)}{2\sqrt{\frac{36}{k^2} + \left(\frac{\mu_m}{AR} + \left(3 + 12\mu_m\lambda^2 AR\right)\right)^2}} + \frac{k}{6}\sqrt{\frac{36}{k^2} + \left(\frac{\mu_m}{AR} + \left(3 + 12\mu_m\lambda^2 AR\right)\right)^2} \tag{A.24}$$

$$\frac{\frac{\partial \bar{P}}{\partial l}}{\frac{\partial T_{avg}}{\partial l}} = 1 + \frac{k\,\mu_m\left(\frac{\mu_m}{AR} + \left(3 + 12\mu_m\lambda^2 AR\right)\right)}{3AR\sqrt{\frac{36}{k^2} + \left(\frac{\mu_m}{AR} + \left(3 + 12\mu_m\lambda^2 AR\right)\right)^2}} + \frac{k}{6}\sqrt{\frac{36}{k^2} + \left(\frac{\mu_m}{AR} + \left(3 + 12\mu_m\lambda^2 AR\right)\right)^2} \tag{A.25}$$

By taking the limit of the ratios as reduced frequency goes to zero and infinity, it is seen that the power sensitivities are greater than the thrust sensitivities for any value of reduced frequency. Similarly, the sensitivity ratios are always greater than one for any value of mass ratio. This means that the power constraint will limit the extent to which the planform design is determined by the thrust sensitivities. Thrust maximizes c, l, and r_{BL} for each of the blade elements, until the power contribution is maximized by the blade element, at

which point power sensitivities limit the maximization of those parameters.